Small-Angle X-ray Scattering Study of Crazing in Bulk Thermoplastic Polymers

by

Gregory John Salomons

A thesis submitted to the Department of Physics in conformity with the requirements for the degree of Doctor of Philosophy

Queen's University
Kingston, Ontario, Canada
January 1998

Abstract

Crazing is a form of tension-induced deformation consisting of microscopic cracks spanned by load-bearing fibrils. This is generally considered to be the primary source of plastic strain response of rubber-modified thermoplastics subjected to applied tensile stress. An understanding of the mechanisms involved in crazing is, therefore, valuable as a means of identifying structure-property relationships. Extensive studies on single crazes in thin films have been done,[1-6] however, experiments on crazing in bulk materials have been fraught with problems, such as difficulties with the production of uniform crazes and accurate temperature control.[7] A new apparatus has been designed to overcome many of these problems; a symmetric tensile stretching mechanism and a radiant heating technique combined with real-time small-angle x-ray scattering (RTSAXS) is used to examine craze fibril structure.

The analysis of small-angle x-ray scattering (SAXS) data is highly model-dependent requiring precise structural models to ensure accurate interpretation. Recently, improved measurement techniques have called into question some aspects of the long accepted models applied to SAXS interpretation of craze structures.[8,9] A detailed examination of the models applicable to craze fibril structure is presented here, including a newly proposed model involving power-law density distributions within the fibrils. It is shown that the best description of craze fibrils comes from a Gaussian density distribution. This is in contrast to the traditional models which describe the fibrils as having uniform density with sharp boundaries.[1,2]

RTSAXS studies of High Impact Polystyrene (HIPS) and Polystyrene (PS) blended with 2 wt.% Polybutadiene (PB) were performed using a constant strain rate of 5×10^{-4} s^{-1}

and temperatures from 30 to 70° C. Crazing deformation modes were identified and the macroscopic deformation characteristics for the two materials were compared revealing a significantly lower mobility of the polymer in the PS-PB blend than in HIPS. The craze fibril structure observed in the two materials was found to be nearly identical with slightly smaller and more uniform fibrils in the PS-PB blend material. This suggests that both materials follow similar craze formation mechanisms with a reduced polymer mobility in the blend material. The identification of this mechanism through temperature-dependent studies is found to be compromised since current theories describing crazing deformation rely heavily on determination of the craze fibril surface energy, a parameter which is poorly defined in the case of diffuse boundaries.

Acknowledgments

I owe many thanks to my supervisor, Marsha Singh for her hard work, timely advice, and regular encouragement. I would also like to thank those who have worked with me on this project over the years: Mike Glavicic, Peter Ma, Greg Hiltz, Bill Newson, LiHong Pan, James Gupta, Adam Foran, and Tim Bardouille. I also owe a great deal of thanks to Steve Gillen and Jim Thompson for their help in designing and building the equipment, Jiahu Wang, for providing the DSC measurements, Lichen Zou, for her assistance with the deposition of laser diffraction grid patterns on to samples, and to Malcolm Capel manager of the X12B Beamline at NSLS, where the experiments were performed. Dr. L.A. Utracki of IMI and Dr. Mark Cranch of DOW Canada deserve special thanks for providing samples.

In addition, I owe a big thanks to my wife Jina who gave plenty of advice on statistical matters, taught me SAS programing, and provided an excellent sounding board as I discussed problems with my data interpretation. Finally, I want to thank my son Timothy, who put up with me patiently while I was writing this thesis, crumpled papers with glee and provided plenty of enjoyable distraction. Both Jina and Timothy deserve thanks for giving me plenty of love and encouragement.

The fear of the Lord is the beginning of knowledge

Proverbs 1:7

These few words contained herein are dedicated
to the one Word which has existed from the beginning,
is with God, and is God:
The Lord Jesus Christ
through whom all things were made
and have their being,
and without whom this work
would be meaningless.

Statement of Originality

Unless stated otherwise, all contents of this thesis is the original work of the author.

The idea of a new apparatus for SAXS measurements of crazing came from discussions with Dr M.A. Singh and M. Glavicic. The design of this new apparatus including stress measurements, radiant heating, and feedback motor control was the work of the author in consultation with J. Thompson and S. Gillen, technicians at the Queen's University Dept. of Physics. The proposal for a laser diffraction system for measuring strain came from Dr. M.A. Singh.

All of the deformation experiments were performed by the author. The analysis of the data was achieved using programs written by the author and by W.A. Foran. The interpretation of the data and all model fitting was accomplished by the author. The Fourier transform analysis employed the GNOM program, provided by Dr. D.I. Svergun.[10–12] The use of this program and the use of the *Sigmoidal-Gradient* model were suggested by Dr. M.A. Singh. The deformation mode parameter, $\widehat{\rho z}$, was developed by the author.

The derivations described in appendices A and B, along with the *Power-Law* model of particles with diffuse boundaries given in appendix C, are the original work of the author. The fitting algorithms described in appendix D were developed by the author with the assistance of J. Zhang-Salomons and Dr. J.T. Smith, the latter of the Queen's University STATLAB.

The tests of the *Constant Background* and Guinier models were established by the author. The observation of subtle detector saturation, mentioned in the conclusions was proposed by Dr. M.A. Singh.

Contents

List of Figures

List of Tables

Acronyms

Measurement Techniques

DSC differential scanning calorimetry

LAED low-angle electron diffraction

RTSAXS real-time small-angle x-ray scattering

SAXS small-angle x-ray scattering

TEM transmission electron microscopy

USAXS ultra-small-angle x-ray scattering

Materials

ABS Acrylonitrile Butadiene Styrene

HIPS High Impact Polystyrene

LDPE Low-Density Polyethylene

PS Polystyrene

PB Polybutadiene

PC Polycarbonate

SBS Styrene-Butadiene-Styrene triblock copolymer

Institutions

BNL Brookhaven National Laboratories

IMI Industrial Materials Institute

LNLS Laboratòrio Nacional de Luz Sìncrotron

NSLS National Synchrotron Light Source

List of Symbols

A Cross-sectional area of craze fibrils ..... equation 3.29

a Length of a polymer segment ..... equation 2.4

a_m Molecular bond length ..... equation 2.17

b Background term for *Constant Background* model ..... equation 4.2

$\bar{D}_f$ Mean fibril diameter ..... equation 3.32

$\bar{D}_p$ Mean fibril diameter from the *Power-Law* model ..... equation 7.5

$\bar{D}_s$ Mean fibril diameter from the *Sigmoidal-Gradient* model ..... equation 7.4

D_o Average inter-fibril distance ..... equation 2.13

D_s Surface fractal dimension ..... equation 3.25

D_{mass} Mass fractal dimension ..... equation 3.25

D_{max} Maximum particle diameter ..... page 112

D_{rep} Reptation diffusion coefficient ..... equation 2.6

f_b Force to break a single polymer bond ..... equation 2.17

f_r Reptation force ..... equation 2.18

$\tilde{I}$ Scattering intensity prefactor ..... equation 3.10

$I(q)$ X-ray scattering intensity ..... equation 3.10

I_e X-ray intensity scattered from a single electron ..... equation 3.1

$I_f(q)$ Scattering intensity from the fibril cross-section ..... equation 3.29

I_{in} Incident x-ray intensity ..... equation 3.1

J_0 Zeroth order Bessel function

K Porod constant ..... equation 3.22

K^* *Power-Law* model Porod constant ..... equation 7.2

L Length of craze fibrils ..... equation 3.29

M_N Number-average molecular weight ..... equation 2.1

M_w Weight-averaged molecular weight ..... equation 2.2

N_s Number of segments in a polymer chain ..... equation 2.4

$P(r)$ Patterson function for a rod cross-section ..... equation 7.10

Q X-ray scattering invariant ..... equation 3.16

Q_{tail} Invariant correction for high-q limit ..... page 104

q Momentum transfer in Å^{-1} ..... equation 3.7

q_{max} Largest q value for which data is obtained ..... equation 7.6

q_{min} Smallest q value for which data is obtained ..... equation 3.19

$\bar{R}_f$ Mean fibril radius ..... equation 7.3

R_o End-to-end distance of a polymer ..... equation 2.4

R_g Radius of gyration ..... equation 2.5

$\overline{R^2}$ Measure of the goodness-of-fit ..... equation D.2

$\vec{r}$ Vector joining the two scattering centers ..... equation 3.5

S Surface area of a particle ..... equation 3.21

T Temperature

T_g Glass transition temperature ..... page 9

$\mathcal{U}$ Energy required to break a polymer bond ..... equation 2.17

$U(l)$ Average potential energy trapping individual polymer segments ..... equation 2.19

$\mathcal{V}$ Volume of a particle ..... equation 3.21

V The entire volume irradiated by the x-ray beam ..... equation 3.9

v_1,v_2 Volume fractions of a two phase system ..... equation 3.23

v_f Volume fraction of craze fibrils ..... equation 4.1

Y Young's Modulus ..... equation 2.10

z Sample thickness ..... equation 3.3

α Power-law exponent of scattering intensity ..... equation 3.24

β *Power-Law* model boundary parameter ..... equation 7.2

$\Gamma(x)$ Gamma function

Γ_f Energy required to create new fibril surface area ..... equation 2.15

γ_o Structural correlation function ..... equation 3.11

$\gamma_f(r)$ Correlation function for the craze fibril cross-section ..... equation 3.29

ϵ_{ii} Axial strain in the ith direction ..... equation 2.9

$\dot{\epsilon}_f$ Rate of craze fibril lengthening ..... equation 2.12

ζ_i X-ray polarization factor in the ith direction ..... equation 3.1

η Power-law exponent for non-Newtonian fluid flow ..... equation 2.11

θ Half the angle of a scattered x-ray relative to the incident direction ..... equation 3.1

λ X-ray wavelength

μ_1 Mobility constant of a polymer in the melt state ..... equation 2.6

μ_T Polymer chain mobility ..... equation 2.18

μ_x Linear mass absorption coefficient ..... equation 3.3

$\frac{\mu_x}{\rho}$ X-ray mass absorption coefficient ..... equation 3.4

ν Poisson's ratio ..... equation 2.10

ξ Constant relating external applied stress to stress at the craze surface .... equation 2.14

$\overline{(\Delta\rho)^2}$ Mean square electron density contrast ..... equation 3.11

ρ Material density

$\widehat{\rho z}$ Reduced thickness-weighted density ..... equation 6.3

$\nabla\sigma_f$ Stress gradient at the surface of the craze ..... equation 2.13

σ_a External applied stress ..... equation 2.14

σ_c Stress directly above the craze fibrils ..... equation 2.14

σ_m Stress at the void surface between fibrils ..... equation 2.15

σ_p Dilatational component to the stress ..... equation 2.8

σ_s Boundary thickness parameter for the *Sigmoidal-Gradient* model ..... equation 3.26

σ_{ij} Full stress tensor for a material ..... equation 2.7

φ Phase difference between two scattered x-rays ..... equation 3.5

Chapter 1

Introduction

Over the past few decades, there has been a tremendous growth in the polymer industry.[13,14] Thermoplastic polymers are becoming an increasingly popular choice as a manufacturing material. Their uses in new applications will require the ability to engineer thermoplastic alloys with specific properties. In the case of glassy thermoplastics, an enhanced tensile strength combined with optimized density and long-term durability are obvious goals. To achieve this, one needs a fundamental understanding of the structure-property relationships involved in polymer deformation. These relationships are quite complex due to the entanglements that result from the interactions of the long chain molecules in a polymer system.

Three distinct macroscopic modes of deformation are known to occur in thermoplastic polymers: shear deformation[14,15] describes the case wherein a polymer deforms through the bulk flow of polymer chains; crazing[13,16] involves the formation and growth of small cracks bridged by load-bearing fibrils; and rubber-particle cavitation[17,18] describes the creation of microscopic voids in rubber-particle additives to relieve local shear stress. Each mode exhibits distinct sensitivities to temperature, applied stress, strain rate, and sample morphology.[3,14,18,19]

Crazing is known to occur as the primary deformation mode in many thermoplastic polymer materials, accounting for up to 90% of the strain energy.[20] Its presence has been linked

with enhanced toughening in polymer blends such as High Impact Polystyrene (HIPS).[21] The formation and growth of crazes depend upon both the large scale structure of the polymer material and interactions between individual polymer molecules in the craze fibrils. A study of craze formation and growth thus provides information regarding structure-property relationships and clues to the fundamental mechanisms of polymer-polymer interactions.

Although it is relatively easy to confirm that crazing has taken place by examining the resultant damage in a deformed or fractured material, little information may be obtained regarding the crazing process through post-deformation analysis. Upon fracture or removal of tension, the craze structure undergoes significant changes with relaxation and slow reabsorption of the craze fibrils back into the bulk material. In addition, processes such as microtoming, required for transmission electron microscopy (TEM) studies, cause irreparable alterations to the craze form, obliterating much of the information on its structure. A non-invasive tool is needed to accurately probe the craze structure.

Craze fibrils are highly oriented and on the order of 100 Å in diameter, thus small-angle x-ray scattering (SAXS) measurements, combined with a 2-dimensional detector, provide a non-invasive tool for examining their properties. This method of studying craze structure has been popular for some time.[1,2,22] More recently, the techniques of real-time small-angle x-ray scattering (RTSAXS) have been applied to the study of craze fibrils in bulk thermoplastic polymers.[5,23–25] Real-time measurements face several difficulties, however, since the production of crazes must be performed within the restrictive confines of the x-ray beampath in a manner which allows for unobstructed passage of the x-ray beam.

Several different techniques have been employed for this purpose. The most common involved flexing the sample rather than applying pure tension.[5,24] This method results in large variations in the local strain conditions leading to nonuniformities among the crazes produced.[14] The group of Bubeck et al.[23] dealt with this problem by fixing one end of the sample to a table with translational capabilities, employing a hydraulic ram mounted on the table to pull on one side of the sample, and then using the translational stage of the table to approximately align the sample center with the x-ray beam. The drawback to this

method is that one cannot maintain observation of the same region in the sample over the duration of the experiment. Ijichi et al.[25] employed a method of symmetric stretching by applying equal tension to opposite ends of the sample. Their design, however, was limited to only one strain rate. In addition, none of the techniques mentioned above were capable of providing temperature-dependent studies which are valuable for investigating the driving forces behind craze formation and growth.[3,6]

A method of generating consistent craze deformation while allowing the in-situ use of SAXS is required. This involves the application of tensile deformation over a wide range of strain rates while holding the sample center motionless relative to the x-ray beam. Temperature control, accurate measurements of applied stress, and strain response are also desired.

The interpretation of SAXS data is a complex issue since it is highly model-dependent. A description of the scattering from crazes, produced by Paredes et al.[1] and refined by Brown et al.,[2] has been the accepted standard for over a decade. Recently, due to the novel use of second generation synchrotron sources which provide access to lower scattering angles and better signal-to-noise ratios, some aspects of these models have been called into question.[8,9] A careful reexamination of the accepted models for craze fibril structure is therefore warranted.

A new apparatus is presented, capable of nondestructive, in-situ measurements of the craze deformation mode in bulk polymer materials. The technique is based on time-dependent transmission x-ray measurements made in conjunction with precise measurements of applied stress.[17,25] This system is unique in that it is capable of in-situ x-ray measurements of bulk polymer deformation mechanisms with varying temperature and strain rate. It can be used to examine four deformation histories: constant strain rate, constant strain, constant stress, and free relaxation.

Data obtained with this apparatus include measurements of the stress applied to the deforming sample, x-ray absorption by the sample, and SAXS diffraction patterns from the sample using a 2-dimensional wire-based detector. The data are used to identify stages at

which the deformation proceeds via the craze deformation mode and to examine the craze fibril structure for two representative thermoplastic materials over a temperature range from 30 to 70° C with a common strain rate. Details of the fibril structure are examined in light of different possible mechanisms of craze formation. Changes in the applied stress and fibril diameter with temperature are compared with predictions from the theory of craze growth by forced reptation.

Chapter 2

Polymer Material Basics

2.1 Polymer Materials

The term 'polymers' is used to describe a broad class of large molecules with carbon based structures. Unlike conventional molecules which are composed of relatively few atoms, a single polymer molecule may contain 10 000 atoms or more. Polymers are composed of many repeat units, called monomers. The repeat units involved can be as simple as ethylene, or as complex as the amino acids which make up a protein or DNA molecule. Due to their large size, polymer molecules tend to become entangled with each other. For this reason physical interactions between molecules dominate over chemical interactions in determining the properties of high polymers. As a result, many polymers behave in a similar manner despite great diversity in their chemical makeup. This has led to their establishment as a distinct class of materials with distinct properties.

2.1.1 Molecular Weight

It is impossible for synthetic polymers to contain chains all of exactly the same length, thus they cannot be described by their total chemical composition, such as $C_{1297}H_{1596}$. Instead, an average molecular weight may be used. The number-average molecular weight, M_N, is

defined as the average molecular weight of each chain.

$$M_N = \frac{\sum N_i M_i}{\sum N_i} \tag{2.1}$$

where N_i is the number of molecules of mass M_i.

Experience has shown that this molecular weight does not adequately describe the properties of a material. For example, in a sample composed of 1000 polymer molecules of weight 100 combined with one molecule of weight 100 000 the number average molecular weight would be $\approx$ 200. The single heavy molecule, however, will have a much more significant influence on the material's properties than will the many small molecules. Situations such as this have given rise to the development of the weight-averaged molecular weight, M_w, defined by:

$$M_w = \frac{\sum N_i M_i^2}{\sum N_i M_i} \tag{2.2}$$

as a practical standard because of its use as a predictor of material properties. To continue with the previous example, the single large molecule will dominate the weight-averaged molecular weight giving $M_w \approx 50\ 000$.

It is also of value to have a measure of the variation in the chain lengths. The polydispersity defined as:

$$M_w/M_N = \frac{\langle M^2 \rangle}{\langle M \rangle^2} \tag{2.3}$$

will be 1 for a material with all chain lengths identical and will increase with increasing size distribution. A typical value for the polydispersity of a synthetic plastic such as Low-Density Polyethylene (LDPE) is 2. For natural polymers, such as proteins, the polydispersity will be 1.0, but for synthetic polymers the lowest values obtained are around 1.02.[15]

2.1.2 Polymer Conformation

Polymer molecules are not necessarily linear; a polymer can have one main chain with many side branches such as LDPE; it can be composed of two or three linear chains bound together at a common point; it can even take the form of a large mesh of linear polymers

joined together at random intervals, as in the case of epoxies. The process by which polymer chains are bonded together, known as cross-linking, can sometimes be so complete that the end product, such as vulcanized rubber, is in fact one gigantic molecule.

Today's commercial materials rarely consist of only one type of polymer molecule. Some, known as copolymers, consist of two or more chemically distinct polymers covalently bonded together. Composites can be formed from polymer-metal or polymer-glass combinations, such as fiberglass, as well as from different polymers blended together without bonding. Just as metals can be combined to form alloys with unique properties, polymers can also be mixed and matched to form new materials with specific properties. An example of this is HIPS in which Polystyrene (PS) is blended with a small amount of Polybutadiene (PB) to form a much tougher material. This particular material will be discussed further in section 2.2.2.

Polymer molecules will rarely exhibit an extended-rod conformation; instead, their form is composed of buckles and twists coiling in upon themselves resulting in a rather globular outline. This coiling can be modeled as a random walk problem where each successive segment can have any orientation relative to its neighbouring segments. This results in an average square end-to-end distance, $< R_o^2 >$[26]

$$< R_o^2 >= cN_s a^2 \tag{2.4}$$

where a is the length of a segment determined from the number of monomers which need to be grouped together to mask all information regarding bond angles, N is the number of segments in a chain, and c is a constant. This coiling of the molecules causes them to be entangled together much like spaghetti. Molecular entanglement considerably complicates the dynamics of polymer motion and gives them many of their unique physical properties.

A more general quantity than R_o is the radius of gyration, R_g, which is well-defined not only for a linear chain (random walk), but for any shape of object or any collection of

objects. The radius of gyration is defined by

$$R_g^2 = \frac{\sum r_i^2}{N_s}. \tag{2.5}$$

Here r_i is the distance from the center-of-gravity to the ith link and N_s is the number of links. Clearly R_g is proportional to the mean end-to-end distance described in equation 2.4.

2.1.3 Polymer Dynamics

The mechanical behavior exhibited by polymers was first described by viscoelastic fluid flow, discussed further in section 2.2.1. Empirical models have been proposed which combine spring and dashpot characteristics to describe the observed behavior of the material under some form of external stress.[15]

The first molecular theory of polymer motion was that of the Rouse bead and chain model[26] which describes a polymer chain as a sequence of beads connected by springs moving through a viscous fluid. There are three fundamental assumptions in this model which hinder its predictive capabilities. Firstly, localized responses are assumed. This means that the force on a given bead is influenced only by its nearest neighbours. Secondly, the polymer chains are considered to have ideal elasticity whereas, in reality, there are ways in which elastic energy can be absorbed by the chain. Finally, the most critical problem for large polymers is the assumption of phantom chains which allows two parts of a polymer chain to pass through each other. This eliminated any role played by entanglement.

The reptation model[26] did away with the phantom chain shortfall of the Rouse model by describing a polymer chain as confined to a narrow tube defined by its neighboring polymer chains. The chain moves by Brownian motion inside of the tube creating and destroying tube lengths on opposite ends as it moves. The time required for the chain to move a given distance can be described in terms of a diffusion coefficient, D_{rep},

$$D_{rep} = \frac{\mu_1 T}{N^2} \cong \frac{R_o^2}{\tau_t}. \tag{2.6}$$

Here μ_1 is the mobility constant, T is the temperature, N is the number of segments in the chain, R_o is the mean end-to-end distance defined in equation 2.4, and τ_t is the length of time necessary for all memory of the original conformation to be lost. As will be shown in section 2.3.3, the reptation model continues to be the basis for most of the current understanding of polymer motion in situations such as the formation of craze fibrils.

2.1.4 Glass Transition Temperature

Amorphous polymers do not exhibit the distinct phases of solid, liquid, and gas. The apparently solid state has liquid-like properties when examined on sufficiently large timescales. However there is a temperature at which a distinct change in the physical properties of the material occurs. This is known as the *glass transition* temperature[14,15] (T_g). Above this temperature there is a decrease in the strength of the material and an increase in the mobility of the polymer molecules; the polymer is said to be in a melt state. It should be noted, however, that a polymer in this state is not well-described by conventional fluid dynamics and that models which describe the polymer dynamics above the glass transition temperature can often be applied below the glass transition with a suitable change in the timescale.

Although general theories of molecular motion are well-established, translating these theories into practical models of macroscopic motion has proven difficult in the case of polymers. The behavior of a polymer material in response to external stress is described in terms of macroscopic models, but modifications to existing materials through changes in processing and structure occur at microscopic levels. In order to bridge the gap between general molecular theories and specific macroscopic models, a detailed understanding of the deformation processes which occur in polymers is necessary. Without this, the ability to design new materials and tailor their properties will be severely limited.

2.2 Polymer Deformation

2.2.1 Macroscopic Deformation

Materials in the real world are subjected to numerous forces. The response of a material to these forces is a primary criterion determining its suitability for a particular application. To understand the material response to external applied stress we must first establish a definition of these forces and the material's response.

The forces acting upon a material are described by the stress tensor σ_{ij};

$$\sigma_{ij} = \begin{pmatrix} \sigma_{11} & \sigma_{21} & \sigma_{31} \\ \sigma_{21} & \sigma_{22} & \sigma_{23} \\ \sigma_{31} & \sigma_{23} & \sigma_{33} \end{pmatrix}. \tag{2.7}$$

We assume here that the center of mass is fixed and that no net rotation of the material occurs so that the tensor is symmetric.[14,27]

The stress can be divided into two parts: dilatational and shear. The dilatational component accounts for volume change and is given by:

$$\sigma_p = \frac{1}{3}(\sigma_{11} + \sigma_{22} + \sigma_{33}) \tag{2.8}$$

The shear stress tensor is obtained by subtracting the dilatational stress from the total stress tensor. If no shear stress is present, the stress tensor will be diagonal.

The response of the material to both external and internal stress is described by the resulting strain. The total strain is also a second rank tensor with identical form to that of the stress tensor (equation 2.7) Dilatational and shear portions of the strain tensor can also be identified in which the normal components of the dilatation (ϵ_{11},ϵ_{22},ϵ_{33}) are defined by:

$$\epsilon_{ii} = \frac{\delta l_i}{l_i}, \tag{2.9}$$

where δl_i is the change in length of a material of length l_i in a given direction.

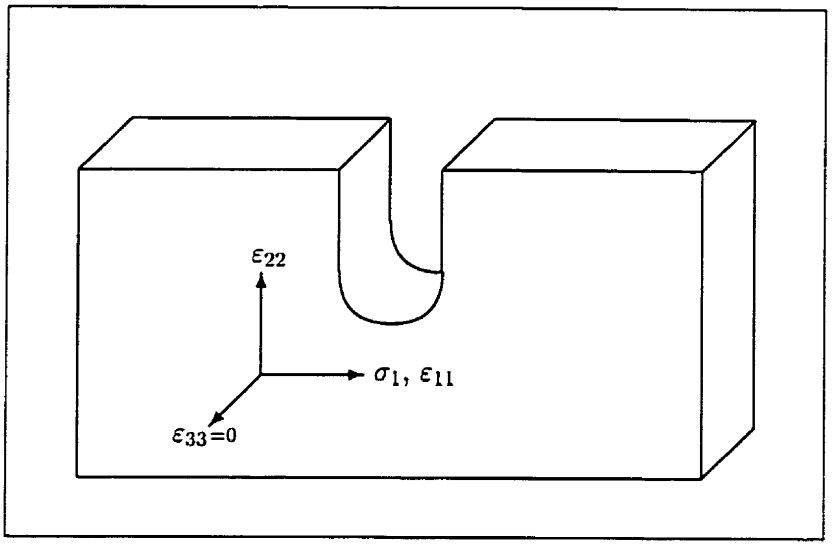

Figure 2.1: An example of plane strain. At the notch point the strain normal to the sample surface may be approximated as zero

In general, the stress and strain components in differing directions are interrelated. Stress applied in one direction may result in a strain response in all directions. Likewise, strain in one direction may cause local non-zero values for all of the stress tensor components. However, there are some cases in which the stress-strain relations can be simplified. In stress applied to a thin sheet, one can approximate the stress normal to the sheet surface, σ_{33}, as zero. This is known as plane stress. Plane strain ($\epsilon_{33} = 0$) may be approximated at concentrated stress points in relatively thick sheets,[14] as shown in figure 2.1.

The simplest form of material response to stress is elastic deformation in which the relation between stress and strain follows Hooke's law;

$$\epsilon_{11} = \frac{\sigma_{11}}{Y} - \frac{\nu}{Y}(\sigma_{22} + \sigma_{33}). \tag{2.10}$$

Here Y is the elastic constant of the material, known as Young's modulus, and ν is Poisson's ratio which describes the material's attempt to maintain constant volume. For small strain values elastic deformation is an excellent approximation of the behavior of most solids.

In amorphous polymers below the glass transition temperature, molecules are not able

to move past each other and elastic deformation is primarily due to bond rotation. This rotation is limited in nature due to the restrictions of the bond angles and interactions between molecules. The result is a short or nonexistent elastic region for most polymer materials.

Polymer deformation is better described by viscoelastic models, such as the spring and dashpot model described in section 2.1.3, where energy loss due to chains sliding past each other is taken into account. Unlike elastic deformation in which the elastic constant is only a function of the material and temperature, the viscoelastic stress-strain curve is also a function of the testing rate, duration, and sample history. In viscoelastic deformation there exists a time lag in the response of the strain to an applied stress; repeated loading and unloading of the material will also change the strain response function. Therefore, the results one obtains are dependent on the type of loading measurements one makes.

There are six primary types of loading tests which can be used to examine deformation: constant strain, constant stress, constant strain rate, constant stress rate, and periodic stress or strain. A material in constant strain is held at a fixed extension. In constant stress, a fixed force is applied and the material is unconstrained in its response. For constant stress and strain rate, the stress or strain is increased at a fixed rate. For periodic stress and strain, the material is cycled through stages of loading and unloading where one of stress or strain is forced to follow an oscillating pattern while the other is measured.

In some cases it is necessary to abandon the assumption of linear stress-strain response implied in viscoelastic motion. In this case one must resort to non-Newtonian fluid mechanics[28] in which:

$$\sigma = (\pm)\sigma_o \left(\frac{\dot{\epsilon}}{\dot{\epsilon}_o}\right)^{1/\eta}, \tag{2.11}$$

where σ is the applied stress, $\dot{\epsilon}$ is the shear strain rate, $(\pm)$ indicates the positive or negative sign of the strain response and η, σ_o, and $\dot{\epsilon}_o$ are material-related constants which are phenomenologically determined.

2.2.2 Microscopic Deformation

Elastic, viscoelastic, and non-Newtonian models are used to describe the three distinct modes of deformation known to occur in thermoplastic polymers: shear, cavitation, and crazing. These deformation modes are the link between molecular models of motion and macroscopic processes.

Shear yielding[14] involves a constant volume deformation; the material responds to the applied stress by changing shape. In shear deformation a polymer deforms through the bulk flow of polymer molecules. During bulk flow, the material behaves as a continuum responding to shear stresses, and the contributions of individual molecules to the total motion cannot be resolved.

Cavitation[17,18] describes the creation of microscopic voids to relieve local shear stress. The dilatation component of the stress is relieved by causing a change in volume. Cavitation is often a precursor to crazing and may also combine with shear yielding when crazing is suppressed. It is also more common in crack tip deformation than in uniaxial stress.

Crazing[13,16] involves the formation and growth of small cracks bridged by load-bearing fibrils and will be dealt with in more detail in section 2.3. Individual molecules play a significant role in the properties of craze fibrils. The formation and growth of these fibrils is, consequently, an excellent mechanism for examining the links between theories of molecular dynamics and macroscopic properties of polymer materials.

Since crazes are capable of absorbing significant amounts of strain energy, it is often in the interest of a manufacturer to modify a material in order to encourage craze growth.[14,21,29] It has long been known that this can be done by incorporating 10 to 20 weight percent of an impurity such as PB with an amorphous polymer like PS.[14] The PB-PS boundaries act as craze nucleation sites[30] by reducing the energy required to nucleate crazes, and thus encouraging craze formation instead of brittle failure. It has been suggested that the PB in HIPS may also perform another function; the PB domains may cavitate and the resulting voids merge to form crazes.[17,21] Recently it has also been suggested that cavitation and crazing in HIPS act independently of each other and that cavitation may

also support shear yielding.[9,31]

Another mechanism of toughening thermoplastics involves the addition of small (up to 4%) amounts of low molecular weight PB to PS.[29] When sufficient (greater than 0.05%) PB is added, domains of rubber are formed in the PS matrix. These pools of liquid rubber are too small to initiate crazes, instead, the liquid is absorbed into the active region surrounding a craze and plasticizes it. This greatly increases the craze velocity and thus increases the strain energy which can be absorbed by a craze.[5,32] This mechanism is quite distinct from that expected to occur in HIPS and the craze structure observed in these two materials is expected to reflect this difference. In addition, thin film deformation tests on this material have reported toughness comparable to that of HIPS with an order of magnitude less additive.[5,32] No such results have been reported for bulk samples of this material.

2.3 Crazing

Crazing is a very common form of polymer deformation, occurring in almost all polymers under suitable conditions —although *suitable* conditions may vary greatly from one material to another. Crazing is also a highly efficient method for polymer deformation, absorbing up to 90% of the strain energy.[20] At the same time, crazes often develop into pure cracks making them a precursor to failure. This has led to a great interest in understanding the crazing mechanism.

Crazing, despite its complexities, is easier to study than other deformation mechanisms since it results in significant volume and density changes in the material. Its distinctive form remains even after the material has fractured. Because of the electron density contrast between voids and the polymer material in a craze, it is ideally suited for scattering studies. The deformation process in crazes is also controlled by the response of individual molecules, thereby providing an excellent opportunity to link theories on polymer molecule motion with macroscopic deformation.

2.3.1 Craze Structure

As mentioned earlier, craze is a crack spanned by load-bearing fibrils. It is usually in the shape of an oblate spheroid 50–1000 μm in length and 0.1–2 μm wide (figure 2.2). Although crazes contain a significant number of irregularities due to impurities and imperfections in the material, they can, with reasonable accuracy, be modeled as having a regular structure,[21,33,34] consisting of several hundred thousand parallel fibrils 200–300 Å apart and 50–300 Å in diameter.[3] Individual fibrils are themselves composed of oriented polymer chains where each chain will be within 4–5 nearest neighbours of the fibril surface.[35] The fibrils maintain a constant diameter throughout the crazing process and are connected at random intervals by cross tie fibrils as shown in figure 2.3. These cross ties, which can compose up to 15% of the fibrillar matter, are of little consequence in the formation and growth of crazes,[13] except for the fact that they tend to pull the craze fibrils out of alignment with each other by up to 5°. Surrounding the craze is a strain-softened area, typically 200–900 Å wide, known as the active region. It is from this region that the craze draws new material as it grows. Outside of this region the material is assumed to be completely unaffected by the presence of the craze.

2.3.2 Craze Growth

The energy required to initiate a craze is significantly larger than the energy required for craze growth; once the critical stress for craze formation is reached and crazes have formed, strain relief will be due to craze growth rather than the formation of new crazes. Craze growth involves dilatation only in the direction of the applied stress. Strain relief, therefore, is limited to this specific direction only; no lateral contraction occurs due to craze growth.[21]

A craze will grow both by lengthening (horizontal growth in figure 2.2) and by widening (vertical growth in figure 2.2). It lengthens by a process known as *Meniscus Instability* growth.[21,28] New fibrils are formed at the craze tip in a process much like that which occurs in peeling tape from a glassy surface. The strain-softened polymer in the active zone around the craze tip is modeled as a non-Newtonian fluid. As the craze tip surface moves

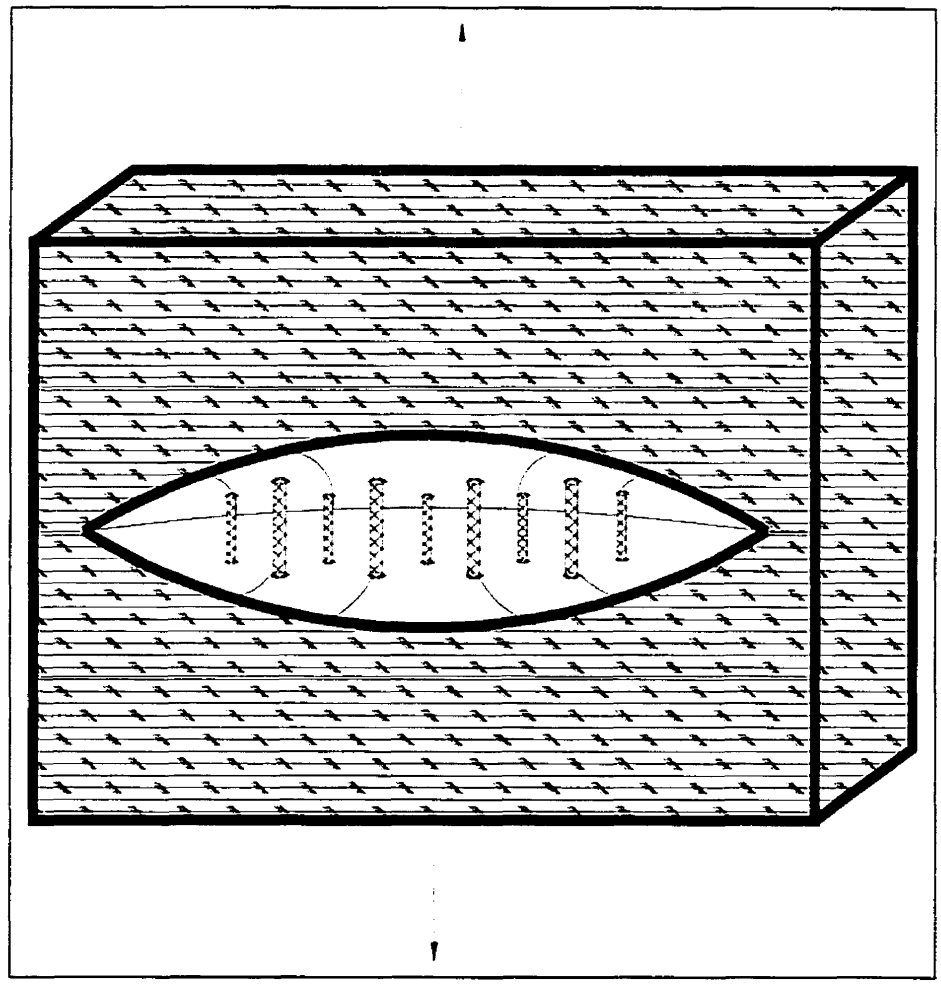

Figure 2.2: A cutaway view of a craze structure with arrows indicating the direction of the tensile force and only a few fibrils shown, for the sake of clarity.

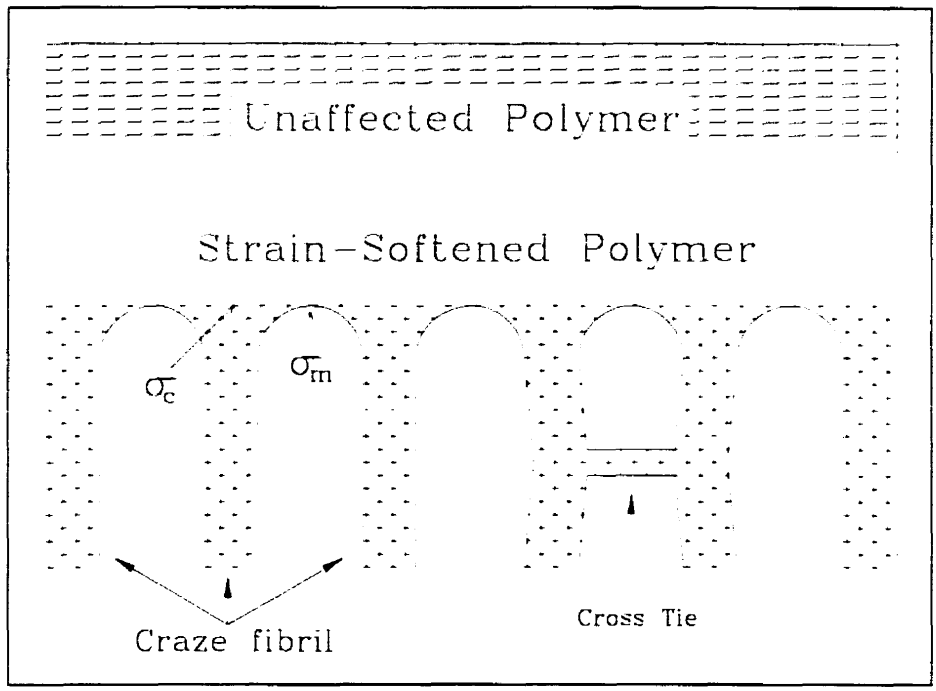

Figure 2.3: The surface of a craze showing the strain-softened region from which the fibrils grow and the bending of fibrils due to cross ties.

undulatory disturbances form (figure 2.4) and develop into fibrils.

As a craze widens, it has been observed that a constant fibril volume fraction, v_f, is maintained.[3,21] This indicates a widening process which is not due to the thinning of preexisting fibrils, but rather is a result of new material being drawn out of the active zone. The size of the inter-fibril spacing is a constant determined by the growth process,[28] implying that the diameters of the fibrils should remain constant.

Craze widening can also be modeled as non-Newtonian fluid flow in which polymer at the edge of the active zone is responding to a lateral stress gradient ($\bigtriangledown\sigma_f$) between the stress immediately above the center of fibrils (σ_c)and the stress at the midpoints between fibrils (σ_m). The rate of widening $\dot{\epsilon}_f$ is then proportional to

$$\dot{\epsilon}_f \propto \mid \bigtriangledown\sigma_f \mid^{\eta} \tag{2.12}$$

where

$$\mid \bigtriangledown\sigma_f \mid \simeq 2\frac{\sigma_c - \sigma_m}{D_o}. \tag{2.13}$$

with D_o being the average inter-fibril distance and η being the power-law exponent from the non-Newtonian flow.

The stress directly above the craze fibrils, σ_c, is considered to be proportional to the applied stress,

$$\sigma_c = \xi\sigma_a \tag{2.14}$$

where σ_a is the applied stress and ξ is a dimensionless constant less than or equal to one. The stress at the void surface between fibrils, σ_m, can be considered to be due to the work required to increase the fibril length by an incremental amount. If the energy required to lengthen the fibril comes exclusively from the energy (Γ_f) required to create new fibril surface area, then from geometrical arguments:

$$\sigma_m = 4\frac{\Gamma_f}{D_o}. \tag{2.15}$$

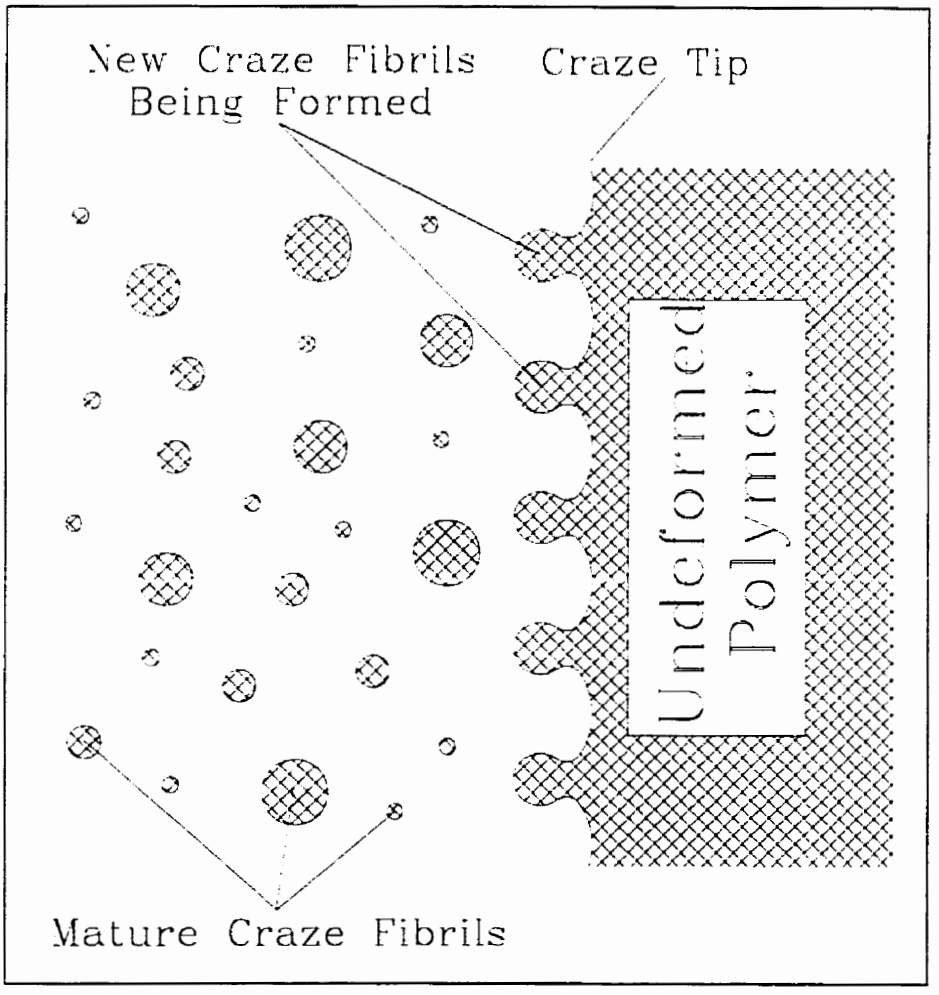

Figure 2.4: An illustration of fibril formation from the bulk polymer by the meniscus instability model. The fibril length extends normal to the plane of view, the applied stress is directed out of the paper, and the craze is expanding to the right.

This equation assumes that the polymer material can be treated as a viscous fluid and that the surface stresses are negligible. In this way, the meniscus-producing surface tension can be equated with the thermodynamic definition of the Gibbs surface energy. It is reasonable to assume that the craze with the largest velocity at any given time will determine the strain rate and stress. When $\nabla\sigma_f$ is chosen to produce the maximum velocity, the applied stress becomes

$$\sigma_a = 8\frac{\Gamma_f}{\xi D_o}. \tag{2.16}$$

2.3.3 Surface Energy And Forced Reptation

The value of the surface energy, Γ_f, is determined by the forces governing intermolecular interactions. There are three major forces which can be at work when new polymer surfaces are formed: Van der Waals, scission, and reptation.[6,19,36,37] The Van der Waals force is due to covalent bond energy between molecules and will be a constant for a fixed configuration. The scission force is due to the energy required to break a polymer chain and depends on the molecular weight and density. The reptation force is due to the energy required for polymer chains to move past each other and depends on molecular weight, strain rate and temperature. The rate of craze growth and hence the toughness of the material will be determined by the dominant force.

As mentioned above, the scission force, f_b is determined by the force to break a single bond. That is,

$$f_b \sim \frac{\mathcal{U}}{2a_m}, \tag{2.17}$$

where $\mathcal{U}$ is the energy required to break a bond and a_m is the bond length.[13,36] The reptation force, f_r is determined by the chain mobility, μ_T:

$$f_r \sim v\mu_T^{-1}\frac{M_N}{M_o} \tag{2.18}$$

where v is the rate of chain pullout, M_N is the mean molecular weight of the chains, and

M_o is the molecular weight of a monomer.[6,19] The chain mobility is given by:

$$\mu_T^{-1} \approx \mu_1^{-1} \int a \exp\{U(l)/kT\}\, dl \tag{2.19}$$

with μ_1^{-1} being the high temperature mobility, a the monomeric length parameter, $U(l)$ the potential energy trapping the individual polymer segments, labelled l along the chain contour, k the Boltzmann constant, and the integral being over the length of a chain.[37]

Below the glass transition temperature in polymers with a large molecular weight, the Van der Waals force is small compared to the scission and reptation forces and can be neglected.[13,36] The scission and reptation forces are generally of the same magnitude and the determination of which force is dominant will depend on the temperature, strain rate and molecular weight. One can define a critical temperature, strain rate, and molecular weight at which the force for chain pullout becomes less than the force for chain scission.[6,19]

At low temperatures, the surface energy of the craze fibrils should be independent of temperature since the scission force is temperature-independent. Above some critical temperature, a decrease in the surface energy is predicted as a result of the transition from scission-dominated forces to disentanglement-dominated forces.[6] This decrease in surface energy is expected to continue up to the glass transition temperature.

To identify the transition from craze growth by scission to that of craze growth by reptation, and thus verify that reptation processes are involved in the crazing mechanism, the surface energy governing the craze growth process may be measured as a function of temperature. Equation 2.16 states that the surface energy may be calculated from measurements of the applied stress and craze fibril diameter and, as will be shown Chapter 3, the craze fibril diameter may be determined using the techniques of SAXS. This process of identification of the crazing mechanisms is essential to any further attempts to test fundamental models of polymer molecule dynamics through bulk deformation measurements.

Chapter 3

Small-Angle X-ray Scattering Basics

Ever since von Laue first used x-rays to examine crystalline copper sulfate, they have proved to be a useful tool for probing the structure of materials. Because of their higher energies, x-rays can penetrate much farther into materials that are opaque at the visible wavelengths. At the same time, x-rays are low enough in energy that they will interact with electrons. X-rays used for scattering measurements typically have wavelengths between 0.5 and 2.5 Å, similar in size to that of interatomic spacings, making them ideally suited for resolving regular crystalline structures and molecular details.

3.1 X-ray Production

X-rays are produced in two ways: through the acceleration of electrons, and through electron energy band transitions between core shells in metals.[38] In an anode source, both of these processes occur. Electrons are accelerated by a high voltage and strike a metal anode. The energetic electrons will either be stopped by multiple interactions with valence electrons, producing bremsstrahlung x-rays, or they may collide with a core electron knocking it free and producing transition line x-rays as valence electrons drop down to replace the missing core shell electrons.

Anode source energies are dictated by the characteristic spectrum of the metals used for the anode. The primary factor limiting the x-ray intensity from these sources is the dissipation of heat generated by electron collisions. A significant increase in intensity is possible with the use of a rotating anode source; the target position on the anode is continually changing, allowing for better heat dissipation and thus higher specific loading.

Several orders of magnitude higher intensity may be obtained by abandoning the luxury of an in-house apparatus for the centralized facility setting of a synchrotron source. Synchrotron x-rays are produced by changing the direction of motion of fast moving electrons or positrons.[39] This is accomplished by the action of a magnetic field produced either by bending magnets, required to keep the electrons moving in a circular orbit, or by insertion devices, placed in straight sections of the synchrotron.

The x-rays produced from bending magnets have a continuous energy spectral distribution over several orders of magnitude with an upper energy limit at some critical value which is a function of electron energy and magnetic field. Insertion devices can be customized to produce a spectral distribution similar to that of a bending magnet, but with a much higher critical energy. They can also be designed to concentrate energy at certain wavelengths giving a large increase in spectral brightness — which is proportional to the photon flux over a 0.1% bandwidth[39] — and thus much greater useable flux. Because the electrons are moving near light speed, the x-rays are concentrated in a small cone parallel to the direction of motion.[39,40] This adds to the brilliance of a synchrotron's x-rays by reducing the source size and angular divergence.

Unlike anode sources, the x-rays produced from synchrotron sources are linearly polarized in the plane of the electron orbit. The polarization becomes elliptical away from the orbital plane. This results in a complex, non-randomly polarized beam, valued for some spectroscopic experiments.[39]

3.2 X-rays and Materials

The electric field from an x-ray can interact with an electron in a material and cause it to accelerate. The resultant electron motion may then be converted back into an x-ray with the same wavelength and a π radian phase shift. This process is called elastic scattering. Scattered x-rays are coherent with an intensity (I_e) is given by:

$$I_e = I_{in}\frac{e^4}{r_e^2 m_e^2 c^4}\left[\zeta_y + \zeta_z \cos^2(2\theta)\right] \tag{3.1}$$

where I_{in} is the incident x-ray intensity, e is the charge of an electron, r_e is the distance from the electron to the point of detection, m_e is the mass of an electron, c is the speed of light, ζ_y and ζ_z are the relative proportions of the electric field polarization in the x and y directions for an x-ray traveling in the x direction ($\zeta_y + \zeta_z = 1$), and 2θ is the angle of the scattered x-ray relative to the incident direction. The factor $[\zeta_y + \zeta_z \cos^2(2\theta)]$ is called the polarization factor. In the case of randomly polarized incident x-rays, such as from anode sources, this becomes $[1 + \cos^2(2\theta)]/2$. For synchrotron sources, where the polarization is non-random, the polarization factor must be determined from measurements of the system.

X-rays can also undergo Compton scattering. In this case a photon collides inelastically with a valence electron, knocking it free from the atom and transferring to the electron some of the x-ray's energy. This results in a change in the wavelength of the x-ray;

$$\Delta\lambda \propto 1 - \cos(2\theta) \tag{3.2}$$

Compton scattering is incoherent; that is, the phase of the outgoing x-rays bears no relation to that of the incoming x-rays. The lack of phase information means that these x-rays will not contribute to the diffraction process and will add a smooth background to the x-ray scattering pattern. At the small angles associated with SAXS the probability of observing Compton scattered photons is quite low and the contribution of incoherent scattering to the diffraction pattern can be ignored.

X-rays can also be absorbed by materials, resulting in heating or chemical reactions.

The absorption of x-rays is related to the material density and thickness by

$$I_z = I_{in} e^{-(\mu_x/\rho)\rho z} \tag{3.3}$$

where ρ is the density and z is the thickness. The ratio $\frac{\mu_x}{\rho}$ is a mass absorption coefficient and depends upon the material and the wavelength of the x-rays with an approximate form far from an absorption edge of[38]

$$\frac{\mu}{\rho} \approx k_x \lambda^3 Z^3. \tag{3.4}$$

Here k is a constant, λ is the x-ray wavelength, and Z is the atomic number of the material.

In summary, four things can happen to an x-ray photon as it passes through a material: It can exit the material without any interaction; it can be absorbed by the material; it can undergo Compton scattering, changing its energy; or it can undergo elastic scattering. The relative probabilities of these events occurring depends on the material and the x-ray wavelength. Of these four, the one which is of primary interest here is the elastic scattering because the x-ray intensity as a function of scattering angle will be dependent upon the macroscopic structure of the material.

3.3 X-ray Diffraction

X-rays scattering from neighboring electrons will combine to form a diffraction pattern. Constructive and destructive nodes in the pattern will depend on the relative phase of the x-rays coming from the different scattering centers. For any two scattering centers, the phase difference depends on the displacement of the electron sites and is determined by:

$$\varphi = \frac{2\pi}{\lambda}\left(\hat{k} - \hat{k}_o\right) \cdot \vec{r} \tag{3.5}$$

where $\hat{k}$ is the outgoing unit wave vector, $\hat{k}_o$ is the incoming unit wave vector, and $\vec{r}$ is the vector joining the two scattering centers.[41] This assumes that each x-ray undergoes at most one scattering event while inside the material. Setting $\varphi = 2\pi$ and noting that

$|\hat{k} - \hat{k}_o| = 2\sin\theta$, one obtains the familiar Bragg's Law

$$\lambda = 2d\sin\theta \tag{3.6}$$

where d is the distance between the two scattering centers and θ is half the angle between the incoming and outgoing wave vectors.

The lengthscales one can examine are determined by the wavelength used and the angular diffraction range available. It would seem logical to increase the wavelength in order to examine structures on larger lengthscales. This is not practical in many cases because the higher wavelength x-rays are more readily absorbed by a material, as shown in equation 3.4. As a result, it is necessary to go to small angles to examine large structures in materials which are strong absorbers at high wavelengths.

3.4 Small-Angle X-ray Scattering

At small angles one can make several approximations about the x-ray scattering observed: the scattering is assumed to be purely elastic (ie. no measurable Compton scattering), the polarization factor of equation 3.1 can be treated as one, and the phase factor in equation 3.5 can be rewritten as:

$$\varphi = -\vec{q}\cdot\vec{r} \quad \text{with} \quad |q| = \frac{4\pi\sin\theta}{\lambda} \approx \frac{4\pi\theta}{\lambda} \tag{3.7}$$

Because small angle scattering usually involves transmission, one must be concerned with the sample thickness. An increase in thickness will result in a linear increase in scattering intensity. At small angles, however, it will also result in an exponential increase in absorption.[38,41] The optimum thickness for small angle scattering is therefore:

$$t_{opt} = 1/\mu_x \tag{3.8}$$

where μ_x is the linear mass absorption coefficient used in equation 3.3. When the sample is close to the optimum thickness one can assume that an x-ray photon will interact with

only one electron as it passes through the material. This means that one can ignore the possibility of multiple scattering confounding the diffraction pattern.[38]

In order to calculate the amplitude, $A(\theta)$, of the scattered wave one must combine the waves scattered by every portion of the material taking into account phase differences:

$$A(\theta) = \int dV\, \rho(\vec{r}) e^{i\varphi(\vec{r})}, \tag{3.9}$$

where $\rho(\vec{r})$ is the electron density at $\vec{r}$, V is the entire volume irradiated by the x-ray beam, and $\varphi(\vec{r})$ is the phase factor defined in equation 3.7. The intensity observed is proportional to the absolute square of the amplitude, $I \propto AA^*$. Using equation 3.7 one has:

$$I(q) = \tilde{I} \int\int d^3r_1 d^3r_2\, \rho(\vec{r}_1)\rho(\vec{r}_2) e^{i\vec{q}\cdot(\vec{r}_1 - \vec{r}_2)}. \tag{3.10}$$

where $\tilde{I}$ includes factors from the incident intensity, absorption by the sample material, and scattering from a single electron. In the discussion to follow, $\tilde{I}$ will be set to one as this can be done with no loss of generality.

The scattering intensity depends only on the relative displacement of scattering centers and on variations in the density of these centers. If one assumes that only two electron densities provide the structural contrast; it is convenient to subtract the mean density, which does not contribute to the scattering, and define a correlation function, which is independent of absolute electron density and depends only on the structure:

$$\gamma_o(\vec{r}) = \overline{(\Delta\rho)^2} V \int d^3r_2 \left(\rho(\vec{r}_2)\rho(\vec{r}_2 - \vec{r}) - \bar{\rho}^2\right), \tag{3.11}$$

with $\vec{r} = (\vec{r}_2 - \vec{r}_1)$, $\bar{\rho}^2$ being the square of the average electron density, V being the total volume irradiated by the x-ray beam, and $\overline{(\Delta\rho)^2}$ the mean square electron density contrast. The fundamental scattering equation thus becomes:

$$I(q) = \overline{(\Delta\rho)^2} V \int d^3r\, \gamma_o(\vec{r}) e^{-i\vec{q}\cdot\vec{r}}. \tag{3.12}$$

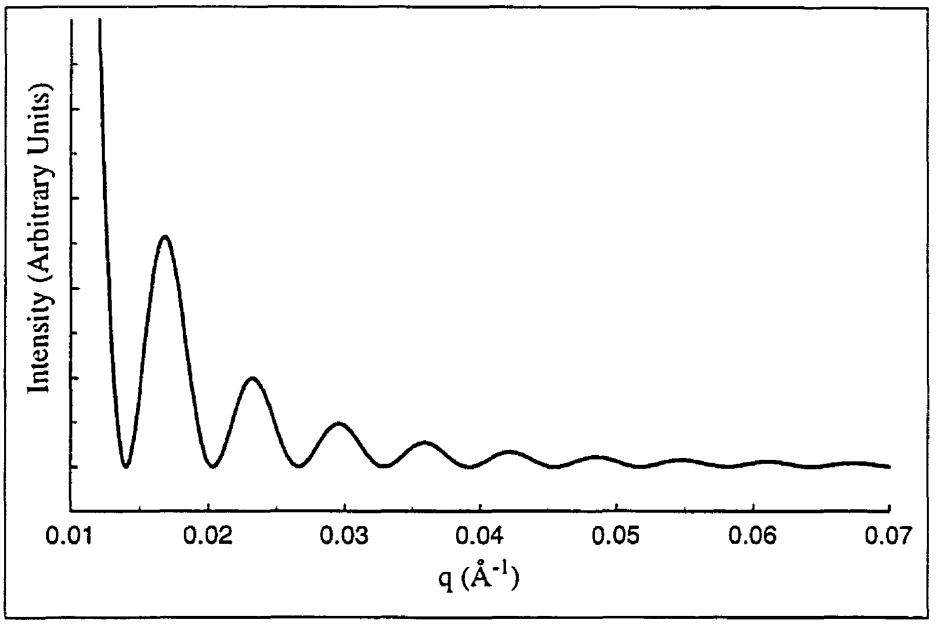

Figure 3.1: Ideal scattering from the cross-section of a single cylinder, showing the peaks that result from such a regular structure.

3.5 Direct Interpretation of SAXS Data

3.5.1 Scattering Peaks

The most common use of wide angle x-ray diffraction is in the identification of Bragg scattering peaks from crystal structures. This type of analysis is also applicable to SAXS data where ordering exists. If long range order is present, the familiar Bragg's law (equation 3.6) applies just as it does for wide angle scattering. For systems in which the ordering is only short range in nature, Bragg's law can only give approximate values, and a knowledge of the scattering geometry is required for more accurate lengthscale measurements[42]

Regular interparticle distances are not the only source of peaks in SAXS data. The form factor for a single regular object will also give a series of peaks, as shown in figure 3.1. Applying Bragg's law to these peaks will result in misleading information regarding the structure under observation. Care must always be taken in identifying the type of structure under observation before interpreting peaks observed in SAXS data.

Variations in particle size or irregularities in the particle structure will often reduce these

peaks to the point where they are completely smoothed out. Interpretation of apparently smooth scattering intensities is accomplished by Fourier transforms of the scattering data, to regain the correlation function, or by assuming structural models to generate a theoretical scattering curve with one or two free parameters which can be fit to the actual data.

3.5.2 Fourier Transform

As noted earlier, the scattering intensity is a Fourier transform of the correlation function, so that the most straightforward method for data interpretation involves a Fourier transform of the scattering intensity. There are several drawbacks to this approach. First of all, the scattering intensity is obtained over a finite range in q and has a finite resolution. Effects from the cutoff points in the intensity data can often introduce significant amounts of error into the transform solution. This problem has been partially solved using the indirect transform method introduced by Glatter[41,43] and developed by Svergun[10-12] in which the intensity is fit to a polynomial series which is invariant under Fourier transformation. Using this procedure, the pair distribution function ($r^2\gamma_o(r)$) may be determined.

In the direct-indirect transform method the scattering data is represented by a series of orthogonal Hermite polynomials where the coefficients of the polynomials in the series may be evaluated using the method of least squares. To ensure fast conversion of the series in both q space and real space, a scale factor is applied to q such that the scaled value corresponding to the maximum q is of the order of 1 to 10, where the Hermite polynomials are known to converge rapidly. This scale factor may be determined from the maximum and minimum q limits combined with the selection of the number of polynomials to be included in the series.[11] Because the number of polynomials included in the series affects the value of the scale parameter, the choice of the ideal number of polynomials is not well-defined. In the method described by Svergun,[10,44] the identification of the ideal number of polynomials to use in the transform is based on a series of tests of the solution. These tests include a χ^2 test, a test for systematic deviations, and a test of the smoothness of the solution.

3.6 Standard SAXS Analysis Models

In addition to the mathematical complexities of the transformation itself, there are difficulties in interpretation of the results. The relation between the correlation function and the physical structure it represents is not always obvious. For simple objects such as spheres, the correlation function has been calculated. However, for objects with intricate form or for systems with interactions between objects (non-random placement relative to each other), the interpretation of the correlation function is not a trivial task. It is often preferable to sacrifice generality in order to extract more specific information from the scattering data. Additional assumptions are often made regarding the structure of the materials and the scattering intensity to develop models from which parameters relating to specific structural properties may be extracted through fitting procedures.

Over the years, standard models have been developed for use with SAXS scattering patterns which can be applied to a broad scope of materials. These standard models use two fundamental assumptions. Firstly, it is assumed that the system is statistically isotropic. In other words, there is no preferred orientation in the system. Secondly, it is assumed that there is no long range order.[41]

The second assumption implies that at sufficiently large r the density distribution will approach the mean density, resulting in

$$\gamma_o(r) \rightarrow 0 \text{ for large } r. \tag{3.13}$$

This condition is necessary in order to place a meaningful maximum limit to the integral in equation 3.12

From the first assumption one can average the exponential factor from equation 3.12 over all orientations as follows

$$\left\langle e^{-i\vec{q}\cdot\vec{r}} \right\rangle = \frac{\sin(qr)}{qr}. \tag{3.14}$$

Combining this with equation 3.12 gives

$$I(q) = \overline{(\Delta\rho)^2} V \int_0^\infty 4\pi r^2 dr\ \gamma_o(r) \frac{\sin(qr)}{qr}. \tag{3.15}$$

3.6.1 Invariant

The most general of the standard model parameters is the invariant, obtained by setting $r = 0$ in equation 3.15. An inverse Fourier transform of this expression combined with the fact that at $r = 0$ the correlation function is equal to the average electron density fluctuation (a constant) gives

$$Q = \int_0^\infty q^2 dq I(q) = \overline{(\Delta\rho)}^2 V. \tag{3.16}$$

The invariant is dependent only on the volume of the scatterers and their electron density contrast, not on the their relative placement. This means that reordering of the system, while it might change the scattering pattern considerably, will not affect the invariant.

The true invariant for a closed system does not produce much useful information regarding the objects under investigation. The effective invariant, which measures the contribution to the invariant from the scattering range under investigation, provides information regarding the volume of scatterers with lengthscales corresponding to the q range used. While the true invariant must always remain constant, the effective invariant may change significantly as a result of changes in the structure being examined.

In some cases it is of interest to obtain absolute scattering intensities by calibrating the scattering intensity from a particular x-ray source using a known standard. If the average electron density fluctuation is known, the absolute scattering intensity may be used to calculate the volume of the scatterers within the appropriate range of lengthscales.

3.6.2 Guinier Approximation

The Guinier approximation deals with the coarse features in the structure. If interparticle interactions are ignored, the correlation function of a particle can be approximated by an averaging of the particle in space and orientation giving a Gaussian distance distribution

function.[45]

$$\gamma_o(r) = e^{(-3r^2/4R_g^2)} \tag{3.17}$$

where R_g is the radius of gyration.

Applying a Fourier transform to the correlation function of equation 3.17 one obtains Guinier's law,

$$I(q) = I(0)e^{(-R_g^2 q^2/3)} \qquad (qR_g \ll 1). \tag{3.18}$$

This equation is valid in the limit of q approaching zero, where the details of the particle's internal structure are not seen. In order to obtain an adequate measure of R_g using Guinier's law, a rule of thumb states that[41]

$$q_{min} D \leq \pi \tag{3.19}$$

where q_{min} is the lowest q point obtained and D is the particle diameter.

Guinier's law allows one to obtain a measurement of the average particle size without making any assumptions about the particle shape. Corrections to the law can also be made for flat platelets and long thin rods.[41] Guinier's law will fail, however, when significant inter-particle interaction occurs. In those situations particles are no longer distributed randomly and the correlation function is not well described by a Gaussian distribution.

3.6.3 Porod's Law

Porod's law is derived by ignoring the large lengthscale features and focusing on individual particle details. It relies on the assumption introduced in equation 3.11, namely that the surfaces of the particles in the system have well-defined boundaries with sharp changes in the density.

The correlation function can be written as a polynomial expansion in r:

$$\gamma_o(r) = 1 - ar + br^2 + cr^3 - \ldots. \tag{3.20}$$

For uniform particles with sharp boundaries, $\gamma_o(r)$ will differ from one at small are by a

ratio[12]

$$\gamma_o(r) \cong 1 - \left(\frac{S}{4\mathcal{V}}\right) r + \ldots. \tag{3.21}$$

Applying this to equation 3.15 gives, to a first order approximation,

$$I(q) \cong (\Delta\rho)^2 V \frac{2\pi S}{q^4 \mathcal{V}} \Rightarrow \frac{I(q)}{Q} = \frac{S}{\pi \mathcal{V}} q^{-4} = K q^{-4}, \tag{3.22}$$

where S and $\mathcal{V}$ are the surface area and volume of the particle, respectively, and K is referred to as the Porod constant. Porod's law is valid even with very anisotropic particles, densely packed particles, and non-particulate scatterers, since it is based on scattering from r values which are small compared to the overall particle size (large q values).

3.6.4 Babinet Principle

Since Porod's law is not affected by relatively large lengthscale features, it is still valid for materials with strong interparticle interference, such as a close-packed structure. In materials of this nature, however, Babinet's Principle of reciprocity[41] cannot be ignored. This principle states that it is impossible to distinguish between scattering from particles and scattering from voids; ie. scattering from a random collection of spheres will be the same as scattering from a solid with a random collection of spherical holes of identical dimension and distribution. In a dilute system, particle scattering dominates and void or interparticle scattering may be ignored. In the case of densely packed particles, both inter- and intraparticle lengthscales contribute to the observed scattering intensity, adding a factor $1/v_1 v_2$, to the electron density contrast, where v_1, and v_2 are the volume fractions of the particles and the void spaces between particles, respectively,

The form of Porod's law remains the same when this principle is applied. However, the surface-to-volume ratio contains contributions from both the voids and particles. A determination of the average particle size, $\bar{l}_1$, requires a knowledge of the volume fraction of the particles:[41]

$$\frac{I(q)}{Q} \cong \frac{S}{\pi v_1 v_2 \mathcal{V}} q^{-4} = \frac{4}{\pi v_2 \bar{l}_1} q^{-4}. \tag{3.23}$$

3.6.5 Deviations from Porod's Law

In practice, the high-q scattering intensity is often not proportional to q^{-4} and modifications to Porod's law are necessary for applications in non-ideal systems. Ruland[46] examined the scattering behavior in Porod law regions for non-ideal systems and categorized them as being either positive or negative deviations. Positive deviations describe scattering patterns in which the intensity decreases *less* rapidly than q^{-4} and negative deviations *more* rapidly than q^{-4}. The positive deviations are generally ascribed to structure within the particles and the negative deviations to poorly defined boundaries.

Many structural models and empirical corrections for positive deviations have been described in the literature.[47–51] The simplest correction for positive deviations[1] is the introduction of a constant background term (*Constant Background* model) to equation 3.22. This correction assumes that the structure within the particles causing the positive deviations is at sufficiently small lengthscales that the scattering from it may be treated as constant in the region of interest. The surface-to-volume ratio of the particles can then be determined from the intercept on a plot of $q^4 I(q)$ vs. q^4.

Another explanation for positive deviations in Porod's law is the presence of a fractal-type structure.[51–54] A fractal is a complex geometrical object which is self-similar on different lengthscales. The volume and surface area of such an object are not well-defined and are functions of the lengthscale used to measure them. The scattering from a fractal object follows the form:

$$I(q) \propto q^{-\alpha} \tag{3.24}$$

where α describes the fractal dimension and is within the ranges:

$$\begin{array}{lcll} 2 < \alpha < 3 & \mapsto & D_{mass} = \alpha & \text{mass fractal} \\ 3 < \alpha < 4 & \mapsto & D_s = 4 - \alpha & \text{surface fractal} \end{array} \tag{3.25}$$

For α in the mass fractal range the particles are fractal in nature throughout and their

characteristic parameter is D_{mass}. For α in the surface fractal range the particles are solid, but their surface is fractal and their characteristic parameter is D_s. The case of $\alpha = 3$ corresponds to a uniform solid with no surfaces, resulting in no scattering being observed. The case of $\alpha = 4$ corresponds to the traditional Porod's law.

Several models have also been proposed to account for negative deviations from Porod's Law. A technique for describing diffuse boundary conditions, introduced by Ruland,[46] describes the particle profile as the convolution of an ideal particle with sharp boundaries and a smoothing function. As discussed in appendix C, the convolution method is useful because the diffuse boundary correction may be treated separately from the ideal particle structure under Fourier transformation. The effect of the smoothing function is dealt with in more detail in section 7.2.1. In the *Sigmoidal-Gradient* model,[46,55] this smoothing function is a Gaussian distribution and the model predicts an intensity distribution given by

$$I(q) = \frac{K}{q^4} e^{-4\pi^2 \sigma_s^2 q^2}, \tag{3.26}$$

where K is the Porod constant and σ_s^2 describes the diffuse boundary thickness.

Another model, similar to the *Power-Law* model described in appendix C, developed to deal with boundaries possessing a finite width describes the change in electron density as a power law function of the form[53,56]

$$\Delta(x) = \Delta_o (x/\Lambda)^\beta. \tag{3.27}$$

Here $\Delta(x)$ is the change in electron density as a function of distance perpendicular to the boundary, Λ is the thickness of the boundary region, and β is a model-dependent parameter. The scattering intensity from this system will be

$$I(q) \propto q^{-(4+2\beta)}. \tag{3.28}$$

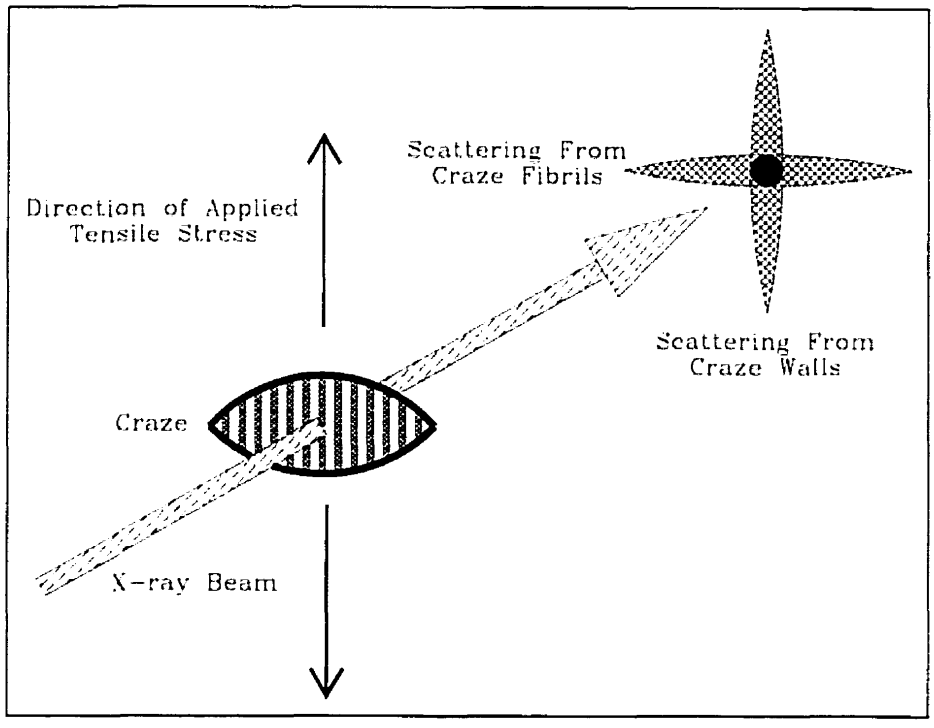

Figure 3.2: A craze structure showing the resultant scattering from the crack walls and craze fibrils.

3.7 Interpretation of Anisotropic SAXS Data

In section 3.6 assumptions of statistical isotropy and lack of long range order were introduced. If one removes the first assumption of a statistically isotropic system, then equation 3.14 is no longer valid and must be replaced with an integration factor which reflects the anisotropy of the system. Here we will examine the case of oriented rod-shaped particles which is applicable to the craze structure — consisting of a crack with load-bearing fibrils spanning the opening — as described in section 2.3.1. X-rays impinging upon such a structure will scatter from both the walls of the crack and from the fibrils (figure 3.2). Because these fibrils are ideally all aligned in the direction of the applied tensile stress, the resultant scattering perpendicular to the applied stress may be modeled as due to scattering from the cross-sections of a system of oriented rods.

The general scattering equation for oriented rod-shaped particles has been determined

by Brown et al.[2] with smearing effects due to a one-dimensional slit detector directly incorporated into the derivation. The smearing effect has only a minor influence on the form of the equation, resulting in a change in the dependence of the scattering intensity on the length of the rods. A detailed derivation which does not include smearing effects, more relevant to the scattering obtained using a highly collimated synchrotron source, is given in appendix A.

To obtain the scattering equation describing craze fibrils, the general equation 3.14 can be separated into two parts representing the long axis and the cross-section of the craze fibrils. Only the cross-sectional term, $I_f(q)$, is of interest, and a two-dimensional phase average results in a scattering equation of the form

$$I_f(q) = 2\pi \cos(\Delta\omega)\overline{(\Delta\rho)^2}AL^2 \int r dr\ \gamma_f(r) J_0(qr) + \text{Interaction Terms}, \tag{3.29}$$

with $\gamma_f(r)$ the correlation function for the craze fibril cross-section, A the cross-sectional area of the craze fibrils, L the length of the fibrils, $\Delta\omega$ the small angular variation in the orientation of the craze fibrils, and J_0 the zeroth order Bessel function.

In order to extract information regarding the fibril structure and mean diameter, modifications must be made to the equations of section 3.5. The fibril scattering intensity (equation 3.29) differs from the standard model (equation 3.12) due to the phase factor of equation 3.14 being replaced with a Bessel function. With this modification, the derivations of section 3.5 proceed in a similar manner.

The oriented rod model results in a change in the invariant of equation 3.16 to[2]

$$Q_f = \int_0^\infty q dq I_f(q) = \Delta\omega\overline{(\Delta\rho)^2} 2\pi A L^2. \tag{3.30}$$

Guinier's law (equation 3.18) requires only a change in the exponent due to the fact that it is now dealing with a 2-dimensional rather than a 3-dimensional object[41]

$$I_f(q) \propto e^{(-R_g^2 q^2/2)}. \tag{3.31}$$

For Scattering Intensity $I \propto q^{-\alpha}$		
α	Description	Dimension
$1 < \alpha < 2$	Random walk mass fractal	$D_{mass} = \alpha$
$2 < \alpha < 3$	Surface fractal on rod boundaries	$D_s = 4 - \alpha$
$\alpha = 3$	Porod's Law for Oriented Rods	$D_{mass} = 2, D_s = 1$

Table 3.1: Fractal dimensions and power-law exponents for oriented rods

The modification of Porod's law (equation 3.22) for oriented rods is

$$\frac{I_f(q)}{Q_f} = \frac{4}{\pi \bar{D}_f} q^{-3}, \tag{3.32}$$

with $\bar{D}_f$ being the mean fibril diameter. This equation has been in use for some time,[1,2,57] yet no derivation or proof of its validity has been found in the literature. For the sake of completeness, and to verify the equation, a derivation is in appendix B.

The interpretation of fractal scattering is also modified due to the change in the underlying Euclidean dimension[54] and fractal dimensions associated with various power law exponents (α) for anisotropic scattering is summarized in table 3.1.

This suite of modified equations may be applied to the scattering from polymers undergoing tensile deformation to determine the structure and size of resultant craze fibrils. In addition, parameters such as the x-ray transmission and applied stress can be combined with time-resolved SAXS data to look for indications of non-crazing deformation mechanisms and to determine the onset time for crazing. The surface energy involved in the extension of craze fibrils may also be determined. With this information, it is possible to critically examine current theories of polymer molecular motion which provide predictions of the fibril surface energy.[6,13,37]

Chapter 4

Craze Structure & Measurements: Literature History

As polymers were developed for an increasing number of applications, the unique deformation properties of these materials underwent considerable study. A desire to understand the mechanisms which occur during the deformation and failure of polymers was realized as the demand for new materials tailored to specific applications grew. Of the different deformation modes observed in polymers, crazing attracted much interest. Crazes were identified as a major source of energy absorption in the deformation process.[14] Crazes were observed to occur in a wide variety of polymer materials under quite different circumstances.[3] Crazes were also easy to study because they resulted in distinct changes in the material structure.

Craze deformation provides an opportunity to study the microscopic processes which govern the motion of polymer molecules below the glass transition temperature. This is possible because significant amounts of stress are transferred onto individual molecules and craze growth is controlled by the response of these molecules to the applied stress.[58] Measurements of craze growth are, therefore, indicative of the motion of individual molecules, and the dependence of temperature, molecular weight, and applied force on the motion of polymer molecules may be examined through appropriate measurements of craze dynamics.

4.1 Craze Growth and Reptation

Very early in the study of craze processes it was noted that there exists a distinct relationship between molecular weight and craze growth.[59] At that time, however, no theoretical basis was available to provide a quantitative explanation of the link between molecular structure and the craze phenomenon.

Paredes and Fischer[1] first provided this link when they observed that the applied stress, σ_a, multiplied by the fibril diameter, $\bar{D}_f$, was a constant. They interpreted this factor, $\sigma_a \cdot \bar{D}_f$, as being proportional to the surface energy, Γ_f, required to lengthen craze fibrils.

This interpretation of craze growth was expanded upon by Kramer[3] using the *Meniscus Instability* growth model as applied by Fields and Ashby.[28] They determined that the 'surface energy' factor measured by Paredes and Fischer should be

$$\sigma_a \cdot \bar{D}_f = \frac{8\Gamma_f}{\xi}\sqrt{v_f} \tag{4.1}$$

where v_f is the volume fraction of fibrils in the craze, and ξ is a constant ($0 < \xi \leq 1$).

Berger and Kramer[36] examined the requirements for the surface energy term in equation 4.1. From this they developed an explanation of the molecular weight influence on crazing observed earlier by Gent and Thomas.[59] By measuring the interface velocity as a function of molecular weight they were able to observe a change from a chain scission dominated surface energy to one dominated by disentanglement forces. They also noted that the disentanglement times scaled with molecular weight in agreement with that predicted by the reptation model, described in section 2.1.3.

The reptation model, as developed by deGennes,[26] was intended to describe Brownian motion in which there is no net force on the system. McLeish et al.[37] modified the reptation model for the case where a polymer chain is experiencing a net force on one end. This is argued to be the case in craze growth where fibrils, and hence individual polymer chains, are being drawn out of the material.

The forced reptation model developed by McLeish was applied by Plummer and Donald[6]

to crazes growing in polymer films. They measured the mean fibril diameter in a craze by means of TEM and calculated surface energy values using the equation (4.1) developed by Kramer.[3] From this, they observed a change in the surface energy which compared favorably with that predicted by the forced reptation model of McLeish. Plummer and Donald also used the forced reptation model to describe the stress-to-fracture in PS films due to craze fibril breakdown[19] thereby illustrating that this microscopic model could be used to predict macroscopic behavior.

Recently, Krupkin and Taylor[60] proposed a new model of forced reptation in which the extrapolation to zero applied force is dealt with more carefully. This is important for situations of polymer fatigue in which a material is subjected to repeated transitory applications of external stress lower than the yield stress for the material. The authors admit that the new model does not include surface energy effects which are critical to the crazing process. They claim that it is possible to include these effects in their model, and plan to do so at a later time.

A *coil-strand-transition* model has been proposed to describe the microscopic process of craze formation and growth.[61] This model is based on an order/disorder transition between the undeformed polymer (coil) and the extended fibrils (strand). The authors claim that it is superior to the *Meniscus Instability* model because it includes an entropy term. In the process of developing their model, however, they claim that the entropic contribution is minor. They also assume that the surface energy is a constant whereas, it has been unequivocally demonstrated[1,6,13,37] that the surface energy is dependent on both molecular weight and temperature. The experiments performed by the authors to test their theory were done at only one temperature with only one thin film sample material (constant molecular weight) being deformed at only one strain rate. The results of their tests, not surprisingly, indicated that surface energy could be treated as a constant.

At present, the *Meniscus Instability* model of craze growth combined with the forced reptation theory appears to be the best description of craze growth. The experimental verification of craze growth by forced reptation has been limited to TEM studies of the growth

of a single craze in a thin film, where the craze fills the entire thickness of the material. It has been reported that macroscopic properties, such as the glass transition temperature, may exhibit large differences between thin films and corresponding bulk materials.[62,63] It cannot, therefore, be stated with certainty that the *Meniscus Instability* model of craze growth and forced reptation are also applicable to bulk materials, where deformation produces thousands of crazes much thinner than the width of the material.

4.2 Production of Crazes in Bulk Materials

The study of crazes in bulk materials is not as straightforward as that in thin films, where one is dealing with a single craze produced under well-controlled conditions. In bulk materials one is dealing with many crazes and the conditions under which those crazes are produced cannot be readily controlled. The measurement of crazes in bulk materials is also complicated by the difficulties of probing a bulk material and interpreting results of measurements averaged over many crazes. There exists several techniques for examining crazes at surfaces but small-angle scattering, by either x-rays or neutrons, is the only practical method for probing the interior of the sample.

When bulk materials are produced, the resulting polymer structure may be slightly anisotropic. As well, internal stresses are often introduced into the material during the molding process. Internal residual stresses and structural anisotropy make it difficult to identify stress and strain processes at a microscopic level and deformation measurements may often give irreproducible results. The issue of the manufacture of bulk polymer material with consistent material properties is an enormous field of research on its own[15] and will not be discussed further here.

In order to effectively study crazes in bulk materials, samples containing uniform crazes in a localized region are desired. Large variations in crazes throughout the sample limit the accuracy of averaging techniques necessary for the study of bulk deformation. It is desirable to have the crazes localized to ensure that active deformation occurs only in the region under examination. There are several methods in use for producing crazes in a sample, each with

its own advantages and disadvantages.

Until recently, the most commonly used method for inducing deformation was three-point bending.[5,14,24,29,30,64] This is a simple technique for producing crazes at a consistent location. However, it has inherent problems in that the applied stress is not uniform across the material resulting in significant variations in craze structure.

Commercial machines are available for applying tensile stress to a material in a very accurate manner. Unfortunately, the machines are large and the samples must be removed from the stress environment prior to measurements of the crazes.[2,8,9,65] The importance of maintaining tension on the deformed sample while the crazes are being measured was discussed by Brown and Kramer,[2] who demonstrated that unloading the samples caused the fibrils to buckle with a loss of orientation and size alteration. They designed a special rig to maintain tension on their samples after being removed from the stretching apparatus.

An apparatus to apply stress while using x-ray scattering to simultaneously monitor the deformation microstructure was designed by Bubeck et al.[17,23,57] This consisted of a stretching rig supported by an optical table placed in the x-ray beam path. The sample was pulled from one side while the entire table top was moved in the opposite direction to keep the center of the sample in the beam path. This design resulted in the sample being in constant motion relative to the x-ray beam with no guarantee that the same region of the sample was being examined at all times. Another drawback to this design is its obvious lack of portability which limits its use to one x-ray source and detector configuration. Ijichi et al.[25] used an in-situ rig in which both sides of the sample were pulled on at the same rate, resulting in a symmetric deformation of the sample and a stationary sample region relative to the x-ray beam path. This design has been the best concept to-date and provided the basis for the present design discussed in chapter 5

In the majority of experiments to-date, crazes in bulk polymer samples have been produced at room temperature. Craze measurements in bulk polymers at temperatures other than room temperature have only been reported by Westbrook et al.[65] They used an Instron tensile tester equipped with a temperature-controlled sample chamber to examine

craze structures at a few selected temperatures. In this case the samples were heated, strained, released, and cut into sections before being examined by x-ray scattering. This paper concentrated on systematic strain rates rather than a systematic temperature study. As mentioned above, the necessity of removing the samples from the stress and temperature-controlled environment prior to any craze structure measurements resulted in the loss of much of the information.

The poor thermoconductivity of polymers has been the primary reason for the lack of temperature-dependent studies of crazes. This limitation makes it difficult to ensure a uniform temperature throughout the material. The problem of providing accurate temperature control for bulk polymers is discussed in further detail in section 5.2.3.

4.3 SAXS Analysis of Craze Structure

For bulk samples, the size of the material prevents in-situ study of the craze structure by TEM. As well, the process of microtoming and staining the material destroys the structure one is attempting to observe.[2,64] For this reason, alternative microstructural measurement techniques are required. The technique of SAXS has proved to be an excellent tool for examining craze structure in bulk materials and thus probing the dynamics of polymer motion.[2,8,9,23,57,64]

In early work, Zhurkov[22] used SAXS to detect submicrocracks forming in some polymer materials when tensile stress was applied. He noted that these long thin cracks formed in large numbers with distances between the cracks on the same order as the dimensions of the cracks. These cracks, later designated as crazes, became the subject of intense study which is still going on today.

The analysis of data obtained from SAXS is highly model-dependent and therefore its interpretation is not as straightforward as the pictures obtained from TEM. The x-ray scattering from crazes is extremely anisotropic; it typically appears as two long thin streaks approximately perpendicular to each other, as shown in section 3.7. As a result of this anisotropy, craze scattering is far more complicated in structure than the standard amor-

phous particle models permit. It has therefore been necessary to develop models of scattering which are specific to crazes. This has been a slow process because our understanding of craze microstructural details has developed in conjunction with the development of these scattering models.

In 1979 two German scientists, Edgar Paredes and Erhard Fischer,[1] developed the first model of SAXS scattering from crazes. By examining the anisotropic scattering, they identified the streak parallel to the tensile direction as coming from the crack walls and the streak perpendicular to the tensile direction as coming from the craze fibrils. Since scattering in different directions comes from different sources, the interpretation and study of these two orthogonal profiles is best done separately.

The study of the SAXS patterns from crazes can be separated into several topics including the interpretation of the scattering pattern parallel to the tensile direction, the measurement of craze fibrils, the calculation and meaning of the invariant (a SAXS parameter proportional to the volume of the scatterers), and methods of distinguishing craze deformation from other mechanisms. A brief description of the development of these topics, along with a discussion of existing controversies regarding data interpretation, is presented in the following sections.

4.3.1 The Scattering Pattern in the Tensile Direction

Small-angle scattering in the tensile direction was examined by Brown and Kramer,[2] who refer to it as *anomalous scattering*. By tilting a sample back and forth through small angles parallel and perpendicular to the tensile direction while noting changes to the observed x-ray scattering pattern, information regarding sources of scattering was obtained. They observed that rotation about the tensile axis produced no change in scattering intensity — an effect consistent with x-ray diffraction. Rotation about the axis perpendicular to both the tensile axis and the x-ray beam, however, resulted in significant changes to the anomalous scattering while exhibiting no changes to the scattering perpendicular to the tensile axis. From this it was concluded that the anomalous scattering was due to reflections from the

craze surface rather than from diffraction processes.

In 1994, Hristov et al.[8] re-examined Brown's assertion[2] that the anomalous scattering pattern produced by crazes in the tensile direction is due to reflections from partially smooth surfaces. A fractured sample was placed in the beam path and rotated about the two axes perpendicular to the axis normal to the fracture surface. A maximum reflection intensity was obtained from this and compared to the anomalous intensity from a crazed sample. Surface areas were compared in both cases and it was determined that the maximum possible intensity resulting from total external reflection off of the craze surfaces was four orders of magnitude lower than the actual scattering measured. In addition, the anomalous scattering pattern was shown to follow Porod's Law. The source of the scattering perpendicular to the tensile direction is well accepted as being due to x-ray diffraction from craze fibrils. Interpretation of the scattering in the tensile direction is, at present, relatively incomplete making it unsuitable for studies of craze growth.

In order to resolve the apparent contradictions in the interpretation of the scattering parallel to the tensile direction a systematic study of both scattering theory and craze structure will be needed. In the absence of this basic information, the study of craze structure is focused on the interpretation of scattering from the craze fibrils.

4.3.2 Fibrils

The scattering from crazes fibrils has not suffered from interpretation problems of the tensile direction scattering. Paredes and Fischer[1] applied a phenomenologically modified *Constant Background* form of Porod's law, as described in sections 3.6.3 and 3.7.

$$I(q) = \frac{K}{q^3} + b \tag{4.2}$$

in which K is the Porod constant, which is related to the diameter of the fibrils and b is the constant background term which is said to be due to inhomogeneities in the craze fibrils. The q^3 term accounts for the fact that the fibrils are oriented parallel to each other. This relation has been the most accepted interpretation in the analysis of craze

fibrils,[2,3,9,17,23,24,29,57,64,66] but is challenged by the results of this work.

Brown and Kramer[2] expanded on the fibril scattering analysis done by Paredes and Fischer. They derived an intensity function for the scattering from fibril cylinders, including a correction factor for the volume fraction of fibrils in the crazes. They also showed that equation 4.2 was valid when the size distribution of the craze fibrils followed a Gaussian form.

In later work, Brown et al.[4] introduced a power-law size distribution function based on the *Meniscus Instability* model.[3] He shows that if the craze velocity is governed by non-Newtonian dynamics, described in equation 2.11, the fibril size distribution, $N_f(D)$, should follow a form

$$N_f(D) = \left(\frac{1 - D_{min}/D}{D}\right)^{\eta} \tag{4.3}$$

where D_{min} is determined from the applied stress and surface energy by:

$$D_{min} = 4\Gamma_f \sigma_a \sqrt{v_f}/\xi. \tag{4.4}$$

Brown et al. calculated theoretical $\gamma_o(r)$ curves in which they observed little variation for different size distribution functions. From this they concluded that x-ray scattering from craze fibrils is not sensitive to the form of the size distribution in craze fibrils. It has been shown that it is possible to obtain precise measurements of the polydispersity.[12] Therefore, their results indicate a low polydispersity or large noise in their $\gamma_o(r)$ data.

The fibril diameters for crazes produced in HIPS at impact speeds were measured using Porod's law.[57] It was observed that the fibril diameter remained constant for the different strain rates examined. This suggests that examining craze growth as a function of strain rate may not provide information on polymer dynamics and that some other parameter, such as temperature, needs to be varied to obtain this information. The strain rates used in this paper, however, were quite high and it is possible that knowledge of the mechanisms involving crazing is obtainable from variations among much lower strain rates, where the relaxation times are longer.

Westbrook et al.[65] used Guinier analysis to measure a mean fibril radius. They acknowledged that the Guinier approximation is valid only where no interparticle interference exists. However, Westbrook argues that no such interference was observed in the fibril scattering. The results from Westbrook et al. are marred by the fact that tension was not maintained on the samples during the x-ray analysis. After the samples were deformed, they were unloaded and cut using a diamond saw. Westbrook claims that the cutting had no effect on the scattering pattern, however, he is unable to test the effects of unloading on the sample shape.

The standard model of craze fibrils as straight parallel cylinders has long been known to be overly simplistic. Deviations from precise orientation will result in a broadening of the craze fibril scattering band. Observations of this effect in HIPS, made by Bubeck et al.,[57] were attributed to the disordering effects of the rubber particle inclusions. The presence of these particles is said to deflect the applied stress slightly causing variations in the orientation of crazes relative to each other. In 1990, Kramer and Berger[13] discussed the effect that cross-tie fibrils had on craze scattering. They noted that the volume fraction of these fibrils is sufficiently small that scattering from the cross-ties themselves is relatively insignificant. These cross-ties, however, have the effect of bending the craze fibrils up to 5° off of the idealized parallel rods picture. Kramer and Berger demonstrated that it was possible to use low-angle electron diffraction (LAED) to resolve these bent rods as two separate scattering streaks approximately 5° on either side of the normal fibril scattering direction. The model describing craze fibril scattering, mentioned above, is based on the assumption of perfect orientation among the fibrils. Observations of non-ideal fibril orientation, particularly in rubber-toughened materials such as HIPS, point to the necessity of examining the validity of the *Constant Background* model of section 3.6.5.

4.3.3 Interpretation of the Invariant

The invariant, a measure of the total volume of scatterers, is also used in connection with Porod's Law to calculate the fibril diameter. Thus, its calculation and accuracy is significant

both in the measure of craze fibrils and in the measurement of craze growth.

In his 1981 paper,[2] Brown and Kramer determined the form of the invariant applicable to fibril scattering. In later work, Brown et al. examined a large single craze in PS generated by three-point bending using both SAXS and optical microscopy.[4,64] From this they demonstrated that the invariant calculated from the fibril scattering pattern is a good measure of craze volume. They also observed that the craze maintained a constant width over most of its length.

Brown and Kramer also used the invariant to calculate the mean fibril diameter.[2] He determined the relation between the value of K, from equation 4.2, and the mean fibril diameter, $\bar{D}_f$, to be:

$$\bar{D}_f = \frac{2Q_f}{\pi^2(1-v_f)K}. \tag{4.5}$$

where Q_f is the invariant and v_f is the volume fraction of the craze fibrils.

Bubeck et al.[23,57] discussed the uncertainties in the calculation of the invariant. They noted that the largest uncertainty is due to the limited range over which the scattering is measured. The contribution to the invariant in the limit as $q \to 0$ is considered to be small. However, the contribution to the invariant in the limit as $q \to \infty$ is expected to be quite significant. An additional term may be added to the invariant to account for the high-q scattering. This term is calculated by assuming that the scattering follows Porod's law up to $q \to \infty$. Bubeck calculates the contribution to the invariant from this term to be approximately 30% of the total value. These results suggested that the accuracy of the invariant is governed by Porod's law measurements.

The invariant is used by Bubeck et al.[17,23,57] as a measure of craze strain. They assumes that the fibril volume fraction is independent of strain rate and conclude that, for craze growth, the invariant should be proportional to the strain and therefore linear with time for constant strain rate tests. The constancy of the fibril volume fraction has been generally accepted,[3,13] however, they neglect to account for the loss of scattering material out of the region irradiated by the x-ray beam.

4.4 Other Deformation Mechanisms

Although an accurate interpretation of craze structure is of primary importance to this type of work, the ability to distinguish between craze formation and other deformation mechanisms is also a fundamental requirement. In order to isolate effects attributable to crazing, an understanding of how crazes interact with other mechanisms in the deformation process is needed. Current theories[2] developed for the analysis of craze scattering have been used to examine the relationship between crazing and other deformation processes.

There exist two different types of crazes resulting from the application of tensile stress; Dettenmaier[66] identifies these as intrinsic and extrinsic. Extrinsic crazes, or Crazes I, are the ordinary crazes examined thus far. Intrinsic crazes (Crazes II) are a secondary phenomenon, occurring only after the polymer has undergone considerable deformation through some other mechanism, and showing considerable differences in size and structure to that of ordinary crazes. Intrinsic crazes are significantly smaller and occupy a much larger fraction of the sample volume than do extrinsic crazes. The number density of the craze fibrils occurring in intrinsic crazes is also larger than that of ordinary crazes. Number and size differences between these two types of crazes is explained by the fact that the polymer has generally undergone significant orientation prior to the formation of intrinsic crazes and nucleation sites for intrinsic crazes are much more numerous.

While comparing the data obtained from RTSAXS measurements of the deformation of HIPS and Acrylonitrile Butadiene Styrene (ABS),[23] Bubeck et al. noted that shear deformation does not contribute to the scattering process and that craze formation which is preceded by shear banding results in crazes which are not perpendicular to the tensile axis. From this he concluded that crazing and void formation are the primary modes of deformation in HIPS. The diamond-like scattering pattern from ABS in which the two streaks were broadened to the point that they were no longer separable was suspected to be due to shear banding prior to crazing, where the shear bands deflected the direction of stress so greatly that a preferred orientation for the crazes no longer existed.[23]

A detailed study of the deformation microstructure of HIPS and ABS was done by

Bubeck et al.[17] Using changes in sample shape determined from changes in x-ray absorption and craze volume calculated from the invariant, total strain and strain due to crazing were determined. This involved the assumption that the entire amount of strain applied to the sample is limited to deformation within the volume irradiated by the x-ray beam. From this they concluded that crazing accounts for about half of the strain in HIPS and less than half in ABS. The remaining strain is considered to be due to cavitation in HIPS and shear banding in ABS. Details of the method for determining relative strain were to be published, but have not yet appeared.

This work was extended by Magalhaes et al.[9] Using the peaks in a log-log plot of the scattering data as a guide, they divided the scattering into a component due to crazing and a component due to void scattering. This separation was then used to calculate an invariant which is solely due to crazing. The total strain and crazing strain were calculated using the x-ray absorption and the invariant following Bubeck et al.[17] Magalhaes claimed that the percentage of strain due to crazing was less than half for HIPS. In this case, however, the measurements were not on previously stretched samples and did not use RTSAXS. As a result, it is unclear whether the two mechanisms were at work simultaneously or sequentially. Magalhaes' results agree with those of Bubeck et al., however, both groups follow the same unproven method for determining relative strain.

An examination of HIPS and a blend of Nylon-6 with PolyPhenylEther were examined at low deformation rates by Ijichi et al.[25] They observed the shape of the background-subtracted scattering pattern and noted a generally amorphous growth in the Nylon sample whereas the HIPS scattering showed the distinct anisotropy of craze formation. It was concluded that crazing was the primary deformation mechanism in HIPS and that the Nylon sample deformed by void formation.

Craze deformation in polymers provides an opportunity to link current theories of polymer molecular motion with the macroscopic properties of polymer materials. The study of craze dynamics, however, is complicated by the need to isolate craze deformation from other mechanisms. Identification of crazing processes and the measurement of craze structure may

be accomplished using the method of RTSAXS. In addition, the literature indicates that HIPS provides an excellent material for the study of crazes.

At present, the interpretation of data obtained from SAXS and RTSAXS it still in the process of being established. A clear understanding of the results obtained from SAXS measurements of crazes will be necessary for it to be possible to use this tool to test the theory of forced reptation in bulk polymers. These issues are addressed here in the course of analyzing the RTSAXS data obtained with in-situ measurements of deformation in HIPS and a PS-PB blend.

Chapter 5

Apparatus Development and Experimental Techniques

5.1 Apparatus Requirements

The use of SAXS as a tool for the study of polymer deformation and craze growth is well-established.[3] Structures of interest range in size from 50 Å to 1 μm. Thus the non-invasive tool of SAXS,[41] employed in conjunction with a 2-dimensional detector, is capable of resolving the anisotropic structures of polymer crazes.

Although SAXS analysis of crazes has been in use for more than a decade, the techniques used to generate and control the deformation process, described in section 4.2, are still under development. Machines designed for controlled deformation of polymers, such as those made by Instron^{TM}, are usually quite large and cannot easily be placed in the confined space of an x-ray beampath. Samples which are deformed first and then placed in the beampath will relax, providing limited information and eliminating the possibility of dynamical studies which are necessary for the identification of specific deformation modes.

Custom-designed tensile stress equipment, intended to fit in a beampath, must satisfy the constraint that the region of deformation be of comparable size to the x-ray beam and be maintained in the beam for the duration of the deformation process. As a result, the

three-point bending method, in which the stress is applied cantilever style, has become the most common technique for in-situ deformation experiments. This technique, although fulfilling the above requirements, is limited in that the applied stress in the region of study is not uniform which greatly complicates the interpretation of the results.

Another important issue is that of sample relaxation. Ideally, tests of deformation processes should include a measure of the sample relaxation after the applied stress is removed as this provides significant information regarding deformation mechanisms. In addition, polymer fatigue (the cumulative damage to a material after a series of small deformation cycles) is of great interest to industry. The deformation cycles used for fatigue testing are expected to follow a pattern of applied tensile stress followed by free relaxation; in practice, the process usually involves alternating between tensile and compression stress. A mechanism enabling free relaxation of the samples by rapidly removing the applied tensile stress without inflicting compression stress, bringing the experimental conditions closer to the ideal scenario, is to be desired.

The amount of strain a sample has undergone is typically inferred from the motion of the sample clamps. This method is prone to errors as there is always potential for considerable slippage in the clamps and for strain to occur outside the region under investigation. Resistive strain gauges (commonly used for strain measurements in metals) are inappropriate for measuring strain in polymers as the yield point of most polymers is more than 10 times the maximum which can be measured by standard resistive gauges. A new system for local strain measurement in polymer materials at the site of x-ray irradiation is, therefore, desirable.

Temperature control has also been a complex issue for bulk polymer systems. The poor thermal conductivity of polymers renders conventional contact heating methods inadequate for thin film polymers and nearly useless in bulk polymer studies. As a result, there have been few investigations of the temperature dependence of deformation processes. A more reliable method of heating and measuring the temperature of bulk polymers would be an asset, making available information previously unattainable

This research project has been dedicated to the development of a portable sample chamber capable of state-of-the-art deformation studies of polymer materials using in-situ SAXS. Symmetric tensile deformation over a wide range of strain rates is a design goal. It is also required that the chamber be compact enough to be easily placed in the limited space of an x-ray beampath for portability. Near-instantaneous stress removal is required in order to allow the samples to undergo free relaxation. The ability to regulate and measure sample temperature is also a necessary design feature. In addition, the chamber is to be capable of providing a means of measuring applied stress and true local strain.

5.2 Development Process

The development of a sample chamber which meets the demands described above required extensive testing and refinement. The chamber has evolved through several test versions over the course of three years of active refinement. Several experiments were run at the X12B beamline of the National Synchrotron Light Source (NSLS) at Brookhaven National Laboratories (BNL) in this time period, during which the chamber's performance was tested and initial data acquired for use in refining the data analysis procedures. A brief description of development stages in the project and improvements yet to be made to the apparatus are presented here to provide a context within which the present state of the apparatus may be appreciated.

5.2.1 Deformation Samples

The choice of materials for the deformation experiments was based on materials commonly used for crazing studies reported in the literature. The most common material used for studying crazing has been PS,[2,24,64,65] however, this material will not craze when in bulk form near room temperature.[3] The next most common material is HIPS.[17,23,57] This was chosen as the primary material for investigation. In addition, a novel blend of PS and PB[29] was examined. Details of these materials are given in section 5.4 and will not be discussed further here.

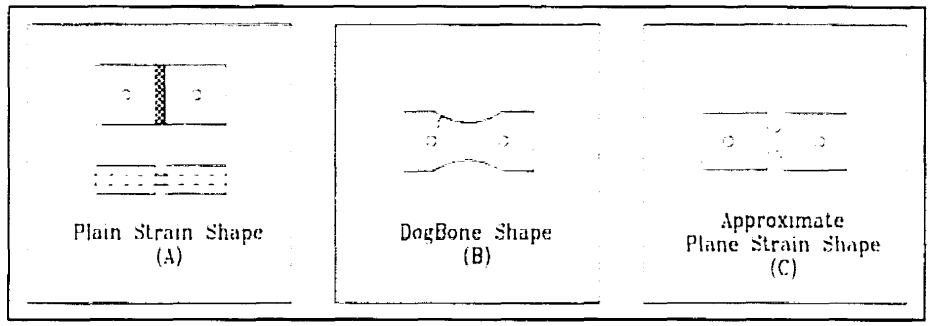

Figure 5.1: Various sample shapes used. (A) True plane strain, (B) *Dog-Bone*, (C) Approximate plane strain

Upon the advice of an experienced materials scientist,[67] it was decided that rather than employing the traditional friction clamps, samples would be secured to the clamps via bolt holes in the end regions of each sample in order to avoid slippage of the sample in the clamps. In addition, a slotted rectangular sample shape (figure 5.1) was suggested for use in tensile deformation experiments. This shape was expected to provide true plane strain conditions[14,67] which would simplify the relation between the stress applied to the whole sample and the stress felt locally at a particular point in the sample. It is not possible to obtain the dimensions recommended with pre-molded materials. An attempt was made to use solvent glues to provide the added thickness necessary on the outer portions of the sample for plane strain effects. Extensive deformation tests later revealed that solvents weakened the samples at the edge of the plane strain region causing premature failure.

Abandoning the true plane strain shape, samples were then cut in the *bow tie* form commonly reported in the literature.[25,57] Circular stress concentrators were cut using a round sanding disk. This method successfully avoided the premature failure observed with previous arrangements. Tests on this sample shape revealed that the ideal clamping mechanism was a combination of bolts and friction clamps. However, as shown in fig 5.1, the sample would sometimes fail at intermediate points along the curved region rather than in the center portion. A lack of reproducibility in the measurement results, attributed to non-uniformity in sample cutting, was also observed. Attempts were made to correct the reproducibility problem by directly molding the polymer material into the desired sample

shape. This attempt failed, largely because design considerations such as oxygen degradation and viscous flow of the polymer melt during molding were far more complex than originally anticipated.

Based on these results an approximate plane strain shape[14] achieved with a custom built cutting jig to ensure reproducibility was adopted (figure 5.1C) . The initial sample material was received from DOW Chemical Canada inc.^{TM} as 2 mm compression molded plates. These plates were cut to the sample dimensions using a diamond saw with a cutting frame attached. The cut samples were then mounted in a separate frame which was used to guide the milling of the stress region and the placement of clamping holes. Deformation tests on these samples gave a high degree of reproducibility in their stress-strain curves.

5.2.2 Tensile Apparatus

An initial study was made of the conventional methods for applying tensile deformation under the conditions described in section 5.1. The use of screw-rods with a gear and chain assembly was found to be preferable to a hydraulic means of applying force for several reasons. Firstly, the screw-rod mechanism could be set to ensure symmetric deformation; this would be difficult, if not impossible, with independent hydraulic rams. Secondly, the space needed for hydraulic equipment was considerably greater than for a motor-driven assembly. Finally, the price difference was heavily in favor of the motor-driven assembly. Further details of this design are given in section 5.3.1.

The force required to break the samples was determined by hanging weights from a sample until it broke. From this information, the torque necessary to drive the apparatus was calculated and then increased by a factor of 10 to allow ample margins for friction. Based on this torque value, the selection of motors to drive the apparatus was made. Initially a commercial motor control system which could drive the apparatus over several orders of magnitude in speed was desired. A market survey revealed that while stepper motors could deliver over an order of magnitude in speed range, they lacked the necessary torque to operate the apparatus. For this reason, synchronous motors which operated at fixed speeds

were selected. Several different motor and gear assemblies were purchased which provided operation at different speeds by interchanging motors, with the maximum speed being set by the torque limitations.

Early experiments revealed that the speeds available from the faster synchronous motors (0.04 mm/s) resulted in deformation processes which were too rapid for time-resolved data acquisition at the X12B SAXS beamline. Use of multiple motors was found to provide an inadequate range of strain rates. A modified motor controller for the synchronous motors,[68] described in section 5.3.1, was therefore designed to allow operation over several orders of magnitude in speed without a loss of torque.

In the majority of tensile test measurements on polymers, strain measurement is obtained using an estimation of the active volume[17] and the known motion of the sample clamps. This is a relatively inaccurate way of determining the true local strain in the region of interest. Commercial resistive strain gauges were applied to samples from this project in an attempt to measure the true strain. These strain gauges failed due to poor adhesion to the polymer surface and the fact that polymers are able to support strains much larger than those the gauges were rated for. Modified strain gauges which are designed for high strains were not considered to be feasible here as their size and mounting mechanisms would interfere with the acquisition of x-ray data and temperature control. An alternative technique was proposed for measuring the true strain, involving laser diffraction from reflective grids deposited on the sample surface. Developing strain in the material leads to a change in grid line density and concomitant changes in the diffraction pattern. The changes in the diffraction pattern can be interpreted to provide direct strain measurements. Recent strain tests have been performed with results suggesting that such a technique is possible. However, difficulties in both grid deposition and interpretation of complex Fresnel diffraction patterns have hindered its realization to date. Work on this technique is in progress.

In lieu of a measure of the true strain, the motion of the sample clamp was monitored to provide an estimate of the total strain. These measurements were obtained by counting the signals sent to the motor by the controller during the process of applying strain to the

samples. After the most recent set of experiments was performed, it was discovered that the motor signals were not being measured at the correct point in the circuit, resulting in low signal and a ringing effect. At sufficiently large motor speeds, this effect did not hinder measurements, but at slower speeds the counter would sometimes miss measurements and sometimes count them more than once. From this it became clear that while the strain rates were consistent and reproducible, the measurements of the strain rate at low speeds were inaccurate by as much as a factor of 2. The problem was found to be due to a fault in the controller assembly and has since been repaired.

5.2.3 Temperature Control

Measurements of polymer deformation as a function of temperature are a significant design feature. To achieve this, early attempts were made to use the interior of the sample chamber as a small oven through the use of convection heating in a low pressure helium atmosphere. An outer vacuum chamber with inner and outer walls of stainless steel was used to provide insulation for the sample chamber. This method of sample temperature control failed due to extensive heat loss. Even with a 500 watt heater in place, the timescales required to reach equilibrium were much longer than was practical in the limited time available for synchrotron experiments.

An alternative to environmental heating was found in radiant heating. Heat lamps with reflectors were placed around the sample to provide uniform heating while minimizing the amount of radiation going down the beampath (possibly affecting equipment and detectors which are part of the beamline assembly). Thermocouples were sandwiched between two sheets of the polymer material to ensure that the temperature they recorded reflected the temperature of the bulk sample and placed in several locations around the sample to confirm the existence of uniform heating. More detail on the temperature control configuration is given in section 5.3.1.

5.3 Current Experimental Setup

5.3.1 Sample Chamber

The current apparatus consists of a portable sample chamber designed to allow transmission mode SAXS.[7] It is currently used with an in-house x-ray tube source (Cu and Cr anodes) as well as at off-site synchrotron facilities of the NSLS at BNL. A direct radiant heating technique is used to provide temperatures of up to 200 °C with +/- 0.5 °C precision and uniform temperature across the sample. Symmetric stretching with variable extension rates ranging from 49.6 μm/s to less than 0.033 μm/s is available. The applied stress is measured with an Entran^{TM} load cell accurate to $\pm$ 5 N and capable of withstanding loads of up to 4.45×10^2 N at temperatures up to 120 °C. Sample clamping is arranged to make possible the rapid removal of applied stress enabling measurement of free relaxation while avoiding the application of compression stress. As mentioned above, a novel method of measuring local strain at the site of x-ray transmission by means of laser diffraction is currently being developed.

The chamber is a stainless steel cylindrical can; 200 mm in diameter and 165 mm high with 2 mm thick walls. Entry and exit ports were cut, 64 mm in diameter, in the cylinder wall at opposite ends for transmission mode SAXS (see fig. 5.2). Sealed 0.003 inch Kapton^{TM} windows may be fitted to the ports to allow for an isolated vacuum or helium environment in the chamber. Kapton^{TM} is used because of its low x-ray absorption and minimal scattering at small angles.[69]

The x-ray windows are centered on the middle of the sample and are large enough to accommodate an unstressed reference blank above the test sample and uninterrupted beam path below (fig. 5.3A). This makes it possible to supplement the scattering data from the stressed sample with reference scattering data from the unstressed blank and the empty beam path without interruption of the x-ray beam. External translational stages are required to reposition the sample and blank in the x-ray beam when necessary.

Extending radially outwards, 115 mm from the chamber wall on both sides, is the me-

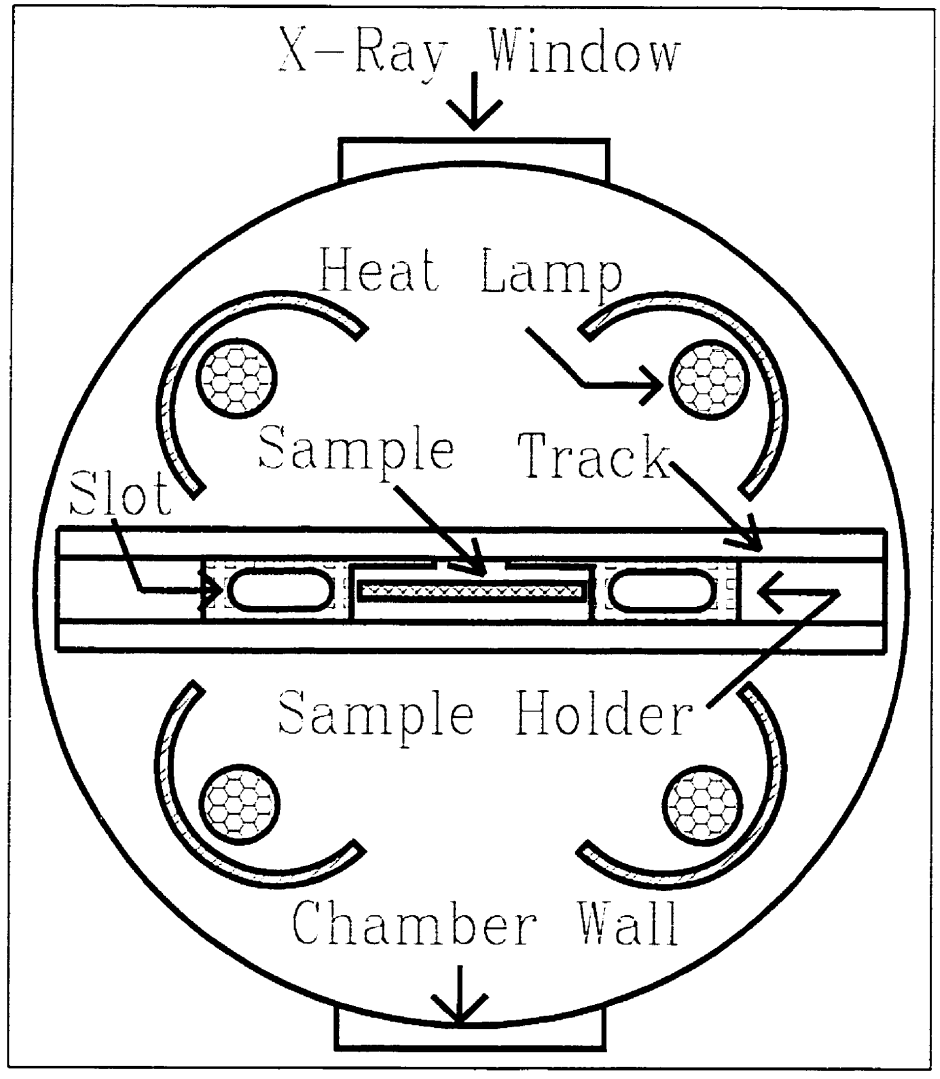

Figure 5.2: Top view of sample chamber showing heat lamps and sample holders with clamping slots. (Clamps not shown for sake of clarity.)

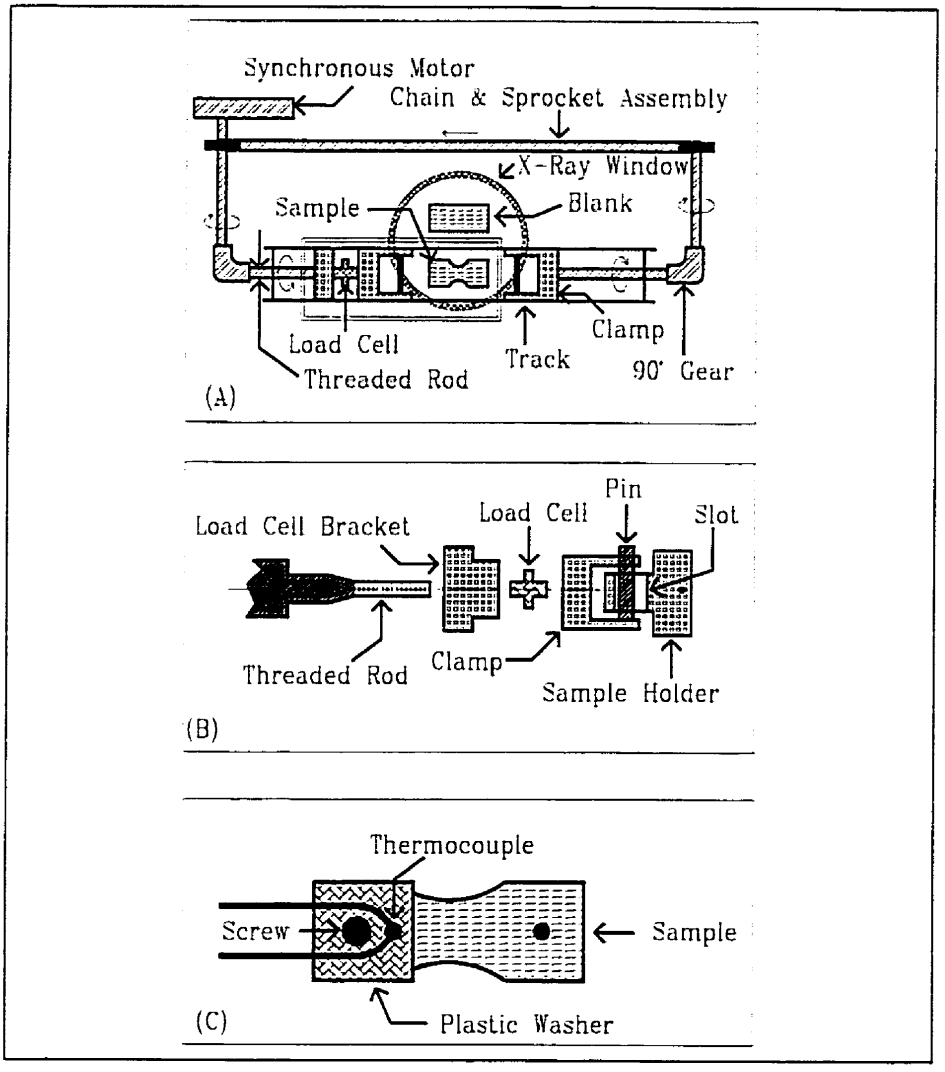

Figure 5.3: Side view of sample chamber, (A) Entire profile showing clamps, load cell, driving mechanism, and placement of sample and blank. (Sample holders omitted for the sake of clarity.) (B) Enlargement of region enclosed by double box. (C) Enlargement of a typical sample showing thermocouple and washer placement.

chanical device used to provide symmetric stretching. As shown in fig. 5.3A, rods with # 10 × 80 threads-per-inch ends are coupled to 90° gear assemblies which are linked by aluminum extension rods to a sprocket and chain set mounted above the furnace. Smooth motion of the chain produces simultaneous motion of the threaded rods in opposite directions. A freewheeling third sprocket (not shown) can be moved perpendicular to the other two in order to vary the path length circumscribed by the chain. This allows the chain to be kept taut to minimize backlash or loosened to allow independent motion of the rods. The entire stretching mechanism can be pivoted by 45° about the axis of the threaded rods, allowing it to be kept clear of detectors and other equipment in the x-ray enclosure.

The stretching apparatus is driven by a SAIA^{TM} UFR4 reversing synchronous motor with a 1:125 series F reduction gear. The motor is controlled by a custom-designed power supply which produces two 90° out-of-phase sine waves at 24 volts and up to 300 mA (see fig. 5.4). The two out-of phase sine waves are encoded as 256 points each onto an 8-bit EPROM and generated by two digital-to-analog converters. The sine wave frequency is controlled by a pulsed input signal directed to a counter. The input signal can come from a variety of sources: an internal oscillator, a voltage-to-frequency converter, or an external function generator. With this arrangement, the system was shown to be capable of producing extension rates of up to 49.6 μm/s at a maximum load of 5×10^4 N and as low as 0.033 μm/s, with the possibility of even lower speeds.

A motor control feedback system between the motor driver and the load cell was implemented such that a constant stress may be maintained on the sample. In addition to constant stress experiments this system allows one to provide an initial consistent tightening of the sample clamps prior to the beginning of a constant strain rate experiment. Safety features were also included in the feedback system to ensure that the motor would stop if the sample broke, the stress became larger than the equipment tolerances, or the motor motion triggered limit switches.

The threaded rods of the stretching apparatus fit into clamps 30 mm high by 8 mm wide. The clamps are connected to sample holders by means of 5 mm diameter pins which

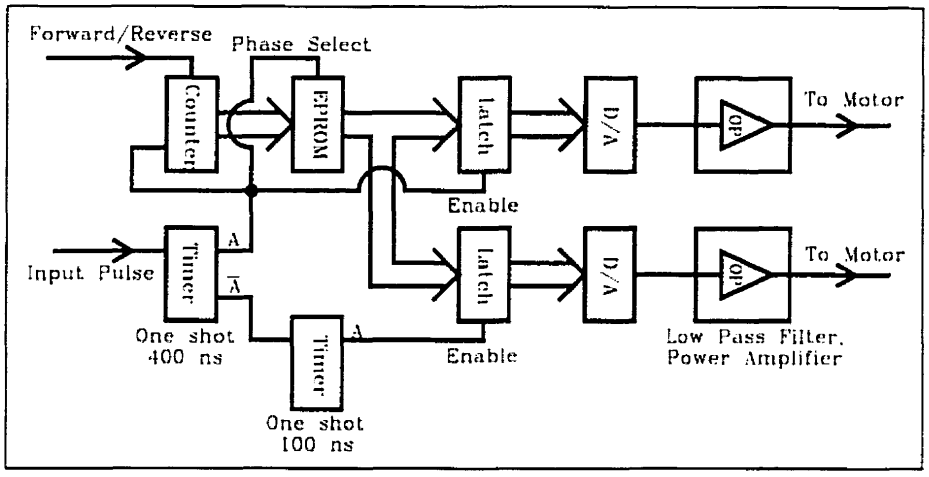

Figure 5.4: Block diagram of the motor controller circuit. Amplitudes for two 90° out of phase sine waves are stored in different parts of the EPROM memory. The *phase select* chooses between the two address regions. The low pass filter, and power amplifier are standard circuits.

fit into 12 mm long slots in the sample holders (fig. 5.3B). These slots protect against the inadvertent application of compression stress when the tensile stress is released through reversal of the motor motion. The slot and pin arrangement also makes the process of changing samples relatively efficient, since the sample is released simply by extracting the pins. This is an important consideration given the restrictive confines of the chamber. The pair of clamps and sample holders slide back and forth in a smooth, 9 mm wide slotted track which provides a guide for the stretching motion.

The sample is fastened to the holders by means of two # 4 screws inserted through holes at either end of the sample (fig. 5.3C). This arrangement ensures that no slippage of the sample in the holder occurs during stress/relaxation, a common problem with frictional clamping methods. Each screw is fastened with a steel washer and a 5 mm square piece of sample material between the screw head and the sample ensuring that the clamping force is spread over a large area to minimize breakage at the clamp region.

Temperature control is provided by four 50 watt halogen lamps, as depicted in fig. 5.2, mounted symmetrically around the inside of the chamber and focused on the sample site. Lamps on one diagonal are offset vertically from those on the other diagonal by 22 mm in

order to produce uniform heating and to ensure that the stressed sample and unstressed blank remain at the same temperature. A Eurotherm^{TM} temperature controller regulates the radiant heating of the sample and unstressed blank by controlling the current supply to the lamps. Tests done on this system using type-J thermocouples sandwiched between two 30 mm × 12 mm pieces of 2 mm thick high-impact polystyrene (HIPS) indicate that, with an initial temperature of about 22 °C and a set point of 70 °C, the temperature of the sample center is within 3 °C of temperatures 10 mm distance to one side, and is stable to ± 1 °C after 10 minutes of equilibration. The primary thermocouple used in temperature control is embedded in one of the square pieces of sample material used to hold the sample as shown in fig. 5.3C. In this way, the temperature probe is as close as possible to the center of the sample without interfering with the passage of x-rays.

5.3.2 X-ray Source

The apparatus described above was used at the NSLS on the SAXS beamline, X12B.[70] This beamline uses a double mirror monochromator and multiple slit beam shaping to provide a 1.59 Å circular beam which is approximately 2 mm in diameter at the sample. During the alignment process, the width of the beam was shown to correspond to the width of the stress concentration region, ensuring that the entire stress concentration region was examined. The sample chamber was mounted between two ionization monitors, approximately 2.6 m upstream from the detector.

The detector used to examine the x-ray scattering pattern at X12B is a 10 cm × 10 cm 2-dimensional delay line proportional counter[70] with 512×512 pixel resolution mounted on the end of an evacuated beampath which could be varied in length to adjust the available angular range and resolution. For the data presented here, sample-to-detector distances of 275 cm and 100 cm were used. The furnace was mounted such that the stretch direction was diagonally across the detector with the undeflected x-ray beam focused on its center. This ensured the widest available symmetric angular range and removed the possibilities of systematic errors that might have occurred from having the stretch direction parallel to the detector wires.

5.4 Samples

Two materials were the primary focus of the deformation experiments: High Impact Polystyrene (HIPS) and, following the report of Brown et al.,[29] a custom blend of Polystyrene (PS) and low molecular weight Polybutadiene (PB). The HIPS material was provided by DOW Chemical Canada, Inc.^{TM} in the form of compression molded 2 mm thick sheets of HIPS (DOW Canada Styron^{TM} 484C). The custom blend was made by the Industrial Materials Institute (IMI) from DOW Canada Styron^{TM} 685D PS with a molecular weight of about 300,000 and a polydispersity of about 2.4 combined with RICON RESINS, Inc.^{TM} PB of a molecular weight of about 2,000. This material was blended to an 8.5 wt% concentrate with the PS by passing it twice through a co-rotating twin-screw extruder running at 400 rpm at a temperature of 175–180 °C. From this concentrate, blends of 5, 2, and 1 wt% were produced by the addition of neat PS via an extensional flow mixer. These blends were then sent to DOW^{TM} Canada where they were molded following a procedure identical to that used for the HIPS material. Preliminary examinations resulted in the selection of the 2 wt% blend for further experiments as this blend appeared to have the greatest toughness.

Attempts to obtain TEM pictures of the sample material were met with mixed success. The microtoming process tends to rip out rubber particles and generally distort the structure. Nevertheless, images of the HIPS material were obtained which were very similar to typical pictures reported in the literature.[21] The results for the custom blend were not so successful. The low molecular weight rubber would not maintain its structure under the microtoming stress and no clear pictures were obtained. An obvious solution is to perform the microtoming at reduced temperatures, unfortunately, microtoming apparatus capable of such low temperature work was not available at the time.

The glass transition temperature (T_g) of the materials was obtained using differential scanning calorimetry (DSC) measurements at the Queen's University Department of Chemistry. The results of these measurements are shown in table 5.1, where it can be seen that, as expected, increasing amounts of toughening additive result in decreasing T_g.

The samples were cut into 30 mm by 12 mm pieces. This was done using a water-cooled

Material	T_g (±0.5°C)
PS	106.7 °C
PS & 1 wt.% PB blend	103.2 °C
PS & 2 wt.% PB blend	102.1 °C
PS & 5 wt.% PB blend	101.0 °C
HIPS	97.6 °C

Table 5.1: Glass transition temperatures for the sample materials

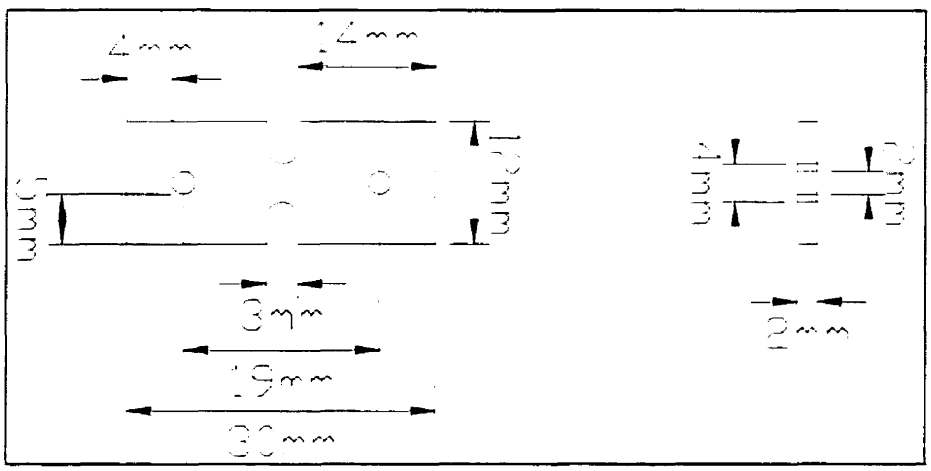

Figure 5.5: Sample dimensions

diamond saw to minimize the size and number of defects produced by the cutting process. Slotted indentations of radius 1.5 mm were cut to a depth of 4.0 mm with a resulting minimum height of 4.0 mm at the middle of the sample (see figure 5.5). This provides a well-defined region for stress concentration. Holes of 2.0 mm diameter were drilled near the ends of the sample for attachment to the sample holders.

A mean cross-section in the stress concentration region of the samples was determined to be 9.0 mm^2. This provides a conversion factor between measured force from the load cell and applied stress. The conversion is based on assumptions that the proportion of strain at a given point in the sample is linearly related to the width of the sample at that point, and that no strain occurs outside of the stress concentration region. An average cross-section can be calculated from an average length within the stress concentration region as shown

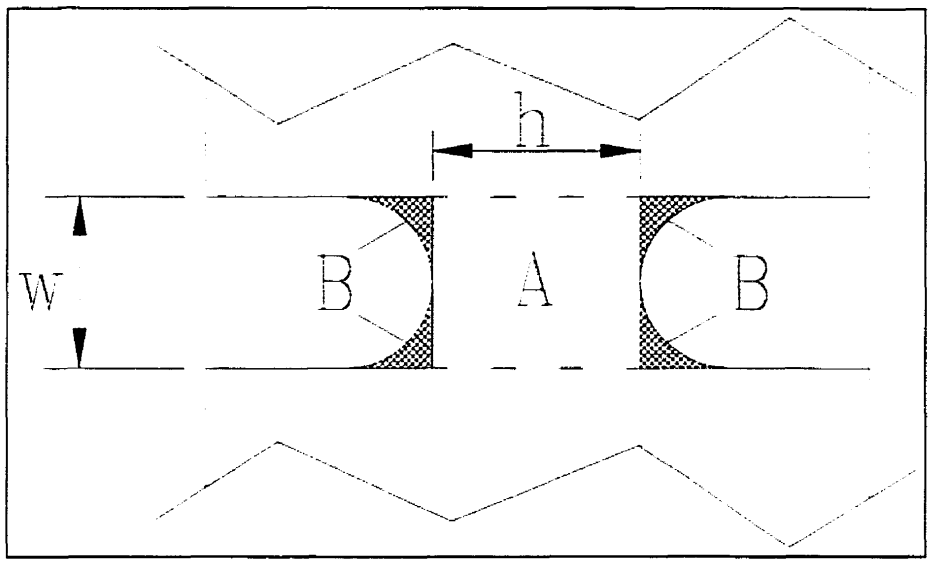

$$\text{Total Area} = A + B = hw + w^2\left(1 - \frac{\pi}{4}\right)$$

$$\text{Average Length} = \text{Total Area}/w = h + w\left(1 - \frac{\pi}{4}\right)$$

Figure 5.6: Calculation of the average length by summing the A and B areas and dividing by the width.

if figure 5.6. These approximations are commonly accepted and considered to be the best alternative to measurements of true strain.[67]

5.5 Experimental Conditions

In the course of an experiment a given sample was heated to a preselected temperature and allowed time to equilibrate for a minimum of 15 minutes. The sample was then deformed under a constant tensile strain rate while recording the applied stress. As the sample was being stretched, a timed series of 25–35 x-ray scattering measurements were recorded using the beamline's 2D wire-based detector. Each measurement consisted of an integration time of 3 to 10 seconds in duration. Prior to these measurements, a long-time (1 minute) scan of undeformed sample material was performed to provide a background reference. In addition

to the x-ray scattering and applied stress measurements, the incident x-ray intensity before and after the sample was recorded for each time slice.

The experiments were limited to the two materials discussed in section 5.4, 2 wt% PS-PB blend and HIPS, due to time constraints at the X12B site. The use of two materials provided both a comparison and confirmation of deformation processes. Both materials are known to craze heavily, but, as discussed in section 2.2.2, the craze formation and growth mechanisms are predicted to be different. A comparison of the results for these two materials provides a confirmation of the observations of craze structure and allows one to look for differences in craze growth mechanisms.

The temperature range chosen for these experiments was from room temperature (~30° C) to 70° C. The lower limit was dictated by the lack of an active cooling mechanism in the sample chamber. As described in section 2.3.3, current theories of craze formation and growth predict that below a critical point (reported as ~60° C in PS[6]) craze growth is independent of temperature. For this reason, it is not expected that the low temperature limit is in any way restricting the study of temperature dependency of craze formation.

The upper limit to the temperature range was chosen for several reasons. Most importantly, the load cell used for measuring applied stress is not accurate above 100° C and should not be subjected to temperatures above 120° C. The use of radiant heating results in uneven temperatures throughout the interior of the sample chamber, and this temperature distribution has yet to be mapped out. It was, therefore, considered prudent to ensure that the temperature remained well below the load cell limits.

The upper temperature limit was also based on estimates of the onset of reptation-driven craze growth. This transition point in pure PS was reported to be at 70° C.[6] The addition of toughening agents to pure PS is expected to significantly reduce this temperature. It was therefore decided that 70° C would be an appropriate maximum.

Measurements were taken at three different strain rates to provide a comparison of deformation processes with strain rate. The majority of the measurements (65 %) were done at the middle strain rate. The three strain rates used were 5×10^{-3} s^{-1}, 5×10^{-4} s^{-1},

and 1×10^{-4} s^{-1}, with the primary rate being 5×10^{-4} s^{-1}. This is much slower than the impact strain rate of 3 s^{-1}, used by Bubeck et al.,[17] but comparable to the strain rate used by Ijichi et al.[25] of 9×10^{-4} s^{-1}.

During the course of the experiments, two different sample-to-detector distances were used. This provided a means to test the reproducibility of the scattering data and ensure that data interpretation was not compromised by detector characteristics. Due to the difficulties involved in changing sample-to-detector distances (such as realignment and recalibration), this distance was only changed once. As a result, the first third of the experiments were performed at the large sample-to-detector distance and the remaining two thirds were done with the detector closer to the sample, providing access to higher scattering angles

With the detector at the largest distance from the sample (2.445 m), the scattering angle range, in q, was determined to be $5.3 \times 10^{-3}\text{Å}^{-1}$ – $7.3 \times 10^{-2}\text{Å}^{-1}$. This corresponds to a Bragg-type d-spacing range of approximately 1000 Å – 80 Å. Similarly, with the detector at the closest distance to the sample of 1.000 m, the range of q measurements was determined to be 0.01 Å – 0.18 Å corresponding to a d-spacing range of approximately 450 Å – 35 Å. This lengthscale range is more than sufficient to examine the craze fibril structures (section 2.3.1) of interest to this study.

Chapter 6

Data Reduction

6.1 Summary of Data Obtained

The data referred to in this chapter was obtained from deformation experiments which were performed at the X12B Beamline of the NSLS at BNL in August of 1996. The low intensity of the in-house x-ray source precludes its use for real-time measurements, however, the in-house setup was used for initial testing and calibration of the apparatus. In addition, two other experiments were performed at the X12B beamline. These experiments were used to further the development and testing of the apparatus, described in chapter 5, as well as to develop the analysis procedures used here. Earlier data contain similar information to that described in this chapter, however, the experimental conditions vary widely, and in many cases the resolution was poorer. Thus in the interest of brevity and clarity, only the most recent data is discussed.

The purpose of these experiments is to identify craze structures in bulk polymer materials, investigate changes in these structures, and monitor the temperature dependence of craze growth. To this end, time-resolved x-ray measurements were performed during the tensile deformation of two different materials undergoing uniform strain rate at varying temperatures and for two sample-to-detector distances. Table 6.1 summarizes the conditions extant for the data obtained with the two materials.

Strain Rate	Material	q Range	Temperature	# Samples
5×10^{-4} s^{-1}	HIPS	0.0053 $Å^{-1}$ - 0.073 $Å^{-1}$	5.0°C Steps	6
5×10^{-4} s^{-1}	HIPS	0.01 $Å^{-1}$ - 0.18 $Å^{-1}$	2.5°C Steps	13
5×10^{-4} s^{-1}	2 wt% PS-PB blend	0.0053 $Å^{-1}$ - 0.073 $Å^{-1}$	5.0°C Steps	6
5×10^{-4} s^{-1}	2 wt% PS-PB blend	0.01 $Å^{-1}$ - 0.18 $Å^{-1}$	2.5°C Steps	15

Table 6.1: Experimental conditions for the data

The data obtained from the two-dimensional detector cannot be interpreted directly in a quantitative way. Several procedures must be followed prior to any model fitting to ensure that the results are accurate. Firstly, the data must be calibrated; this involves both a conversion from pixel position to scattering angle and corrections to the intensity for detector non-uniformity, dead time and incident intensity. Secondly, a subtraction of the background scattering intensity must be done. Finally, it is necessary to identify the deformation processes occurring so that scattering related specifically to craze growth may be studied. In each of these steps, precise data handling is required in order to ensure that the integrity of the data is maintained and the resulting interpretations are valid.

6.2 Calibration and Reduction

6.2.1 Detector Correction.

As mentioned above, intensity values from the wire-chamber detector, measured as counts per second, cannot be used directly. Counts recorded must be adjusted for dead time and detector nonuniformities. Dead time corrections are relatively simple; the counts per second values are scaled by the time required for the detector to recover from the previous signal measurement. This dead time factor is calculated automatically by the data acquisition software.

The detector nonuniformities are compensated using the procedure available on the X12B beamline. In this procedure, developed by Capel et al.,[70] a small amount of air is allowed into the flight path just in front of the detector. The x-ray beam scatters off of

this air producing a uniform image on the detector. After adjusting for $1/r^2$ reductions in intensity by dividing the image by a smoothed version of itself, this image can be used as a measure of the efficiency for any point in the detector, providing a matrix of pixel-by-pixel correction factors.

6.2.2 Calibration

Materials with known scattering patterns are used as references to convert detector pixel positions to angle or q values. For the low angular range, a sample of Europrene SOLT 161B Styrene-Butadiene-Styrene triblock copolymer (SBS) material, which had been previously prepared and calibrated in-house, was used. For the high angular range, the beamline manager provided a calibration standard of cholesterol myristate with a lamellar d-spacing of 50.7 Å. Both of these samples produce diffraction patterns containing a perfectly symmetric primary circular ring which could be readily identified.

The conversion of detector pixel position into q values requires a knowledge of the location of the beam center. This can be determined from the circular scattering patterns of the calibration standards. Initially, the beam center is approximated as being at the center of the 512 × 512 pixel detector. Horizontal and vertical line sections (0°, 90°, 180°, and 270°) passing through this center are then extracted from the calibration data. By comparing the position of the peaks at opposite angles, the center position can be correctly identified in both directions.

Once the new beam center has been determined, the process of extracting horizontal and vertical lines is repeated to confirm the accuracy of the beam center. Due to the integer nature of the pixels, the software used to process the data can only accept integer values for the beam center, and this integer accuracy is the limiting factor in determining its location.

Slight differences in the two sets of delay lines in the detector result in slightly different pixel sizes in the horizontal and vertical directions. To correct for this, the horizontal and vertical axial lines passing through the beam center were compared and a scaling factor was applied to the vertical direction to cause the locations of the horizontal and vertical peaks

to coincide.

The q value at which the calibration peak is known to occur can then be associated with a specific detector position calculated as a distance from the beam center in units of pixels. Having obtained a q value for one pixel position, the peak position, q values were then assigned to all pixel distances from the beam center on a linear scale.

A circular beamstop, placed on the front window of the detector, results in a region of zero intensity recorded by the detector at the beam center. From the calibration and compensation x-ray patterns, the size of the beamstop was determined to be 11–12 pixels in radius. To protect against any parasitic scattering from the beamstop edge, a low-q limit to the data was taken from a radius of 15 pixels. In addition, near the detector edge the efficiency became so poor that intensity measurements were dominated by detector effects. The maximum distance from the beam center was set therefore set to 220 pixels instead of 256 pixels.

A verification of the calibration procedure was made using direct measurements of the angles involved. The distance from the sample to the detector was obtained using the surveying equipment available at the beamline for both angular ranges. The x-ray wavelength was determined independently using Bragg's law and the known angle of the Si III monochromator relative to the incoming white x-ray source.[71] The pixel-to-q conversion was calculated using the definition for q given in equation 3.7

$$q = \frac{4\pi}{\lambda} \sin\left(\frac{\tan^{-1}(r/d)}{2}\right) = \frac{4\pi}{\lambda} \sin\theta \tag{6.1}$$

where λ is the x-ray wavelength, d is the sample-to-detector distance, and r is the distance on the detector plane from the beam center in units of pixels. The calibration values calculated from the sample-to-detector distance agreed with the values obtained from the calibration standards to within 1.5%. To allow for additional inaccuracies in the calibration due to beam center location, X-Y ratios, and nonlinear pixel scaling, the q values were assigned an error of $\pm 2.5\%$, used in determining the accuracy of peak and breakpoint locations.

Figure 6.1: A typical two-dimensional scattering pattern

6.2.3 Identification of Crack and Craze Directions

The scattering pattern from a typical craze formation is extremely anisotropic, consisting of two perpendicular x-ray scattering bands, as shown in figure 6.1. These two bands may be associated with craze wall and craze fibril scattering. In order to proceed with a study of craze formation and growth, the craze fibril band must be identified and extracted from the two-dimensional data.

The band in the direction of the applied stress may be identified as coming from the walls of the crazes,[2,3] while the band approximately perpendicular to the applied stress is due to scattering from the craze fibrils (section 3.7). A knowledge of the detector orientation

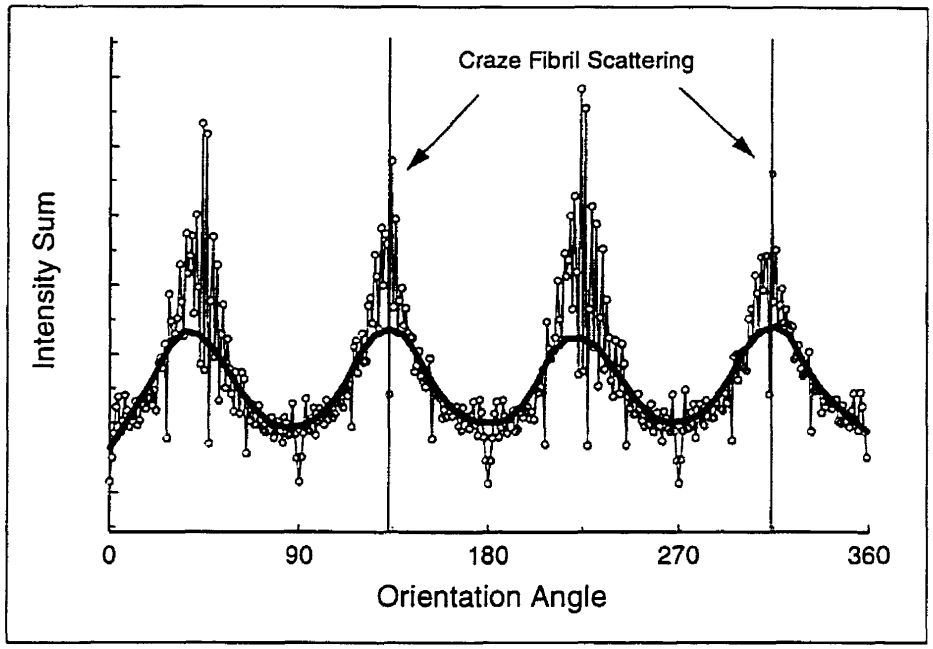

Figure 6.2: Craze fibril directions identified through intensity integrations with the solid line indicating parabolic fitting.

relative to the tensile stress direction will provide a crude estimate of the direction of the craze fibril band in the 2D scattering pattern. However, a more precise identification of the azimuthal angle corresponding to craze fibril scattering (orientation angle) is required due to the possibility of slight irregularities in the samples. To this end, a sum of the intensities at all radii was calculated for each direction. Using these values, plots of intensity sum vs. orientation angle were made (figure 6.2), and peaks in these graphs, corresponding to different scattering bands, could be identified. Parabolic fits to the peaks were used to select the peak center from which precise orientation angles for the craze fibril scattering were obtained.

To ensure the accuracy of this method, the peak positions were compared to orientation angles obtained from contour plots of the two-dimensional data. In most cases the two results agreed to within 2°, the limit of accuracy in the contour plot measurements. In the few cases where large discrepancies appeared, the parabolic fitting technique seemed to be biased by one or two extreme points that can be explained by electronic jitter. Such

cases could also be identified by large discrepancies between the peak positions at opposite angles. For these samples, the angles obtained from the contour plots were used.

The craze fibril peak position was quite consistent between different samples, varying by about 5°. This was a good indication not only of the applicability of this method, but also of the reproducibility in the samples and tensile deformation mechanism.

One of the PS-PB blend samples examined showed angular peaks quite different from other samples. This difference indicated that the sample had probably failed due to some intrinsic fault in the material. Such failure is not expected to occur by the same mechanisms of craze formation and growth, and therefore the data from this sample was omitted from further analysis processes.

It is also worth noting that prior to deformation, the samples showed slight anisotropic scattering at angles above 0.08 $Å^{-1}$.This anisotropy, which was observed in both materials, but not seen in the calibration standards, is believed to be due to a slight orientation of the polymer molecules during the molding process. It's location at q values beyond the primary fitting region and the fact that it is quite faint suggests that it does not have a significant effect on scattering measurements.

6.2.4 2D to 1D Reduction

Having identified the craze scattering region on the detector, the data was compensated and converted to one-dimensional scattering profiles. Each x-ray scattering measurement was compensated for regional variations in detector efficiency, as described in section 6.2.1. As part of this process, data from pre- and post-sample ion counters was used to normalize the intensity, making it independent of fluctuations in beam intensity, sample thickness, and detector dead time.

Pie-shaped sectors 10° wide, centered on the angular peaks associated with craze fibril scattering, were extracted from each two-dimensional data image. For each sector the intensity values at equal radii were averaged to produce a one-dimensional intensity profile. Errors in the intensity for each radius were calculated using counting statistics which assume

a normal distribution.

The choice of 10° wide sectors is based on previously reported TEM work which described the craze fibrils as being out of alignment by up to 5° in either direction.[13] Observations of individual thin film crazes by LAED produced two scattering bands 10° apart. The scattering average over thousands of crazes causes these bands to merge into one single band.

Statistically significant systematic differences in the intensity at opposite angles were observed. It was not possible to reconcile these differences through a simple shifting or scaling of the radius, as would have been expected if they were due to calibration inaccuracy. These systematic differences could come from a number of sources, but are most likely due to a slight wandering of the beam center in the course of a series of time-resolved measurements. As a result of this effect, the intensity values from opposite angles were not binned, but were recorded separately as distinct observations.

6.3 Background Subtraction

The observed x-ray scattering in the craze fibril direction is a combination of scattering from the electron density contrasts between craze fibrils and voids, between the toughening additive and the polymer matrix, and between the polymer chains and intermolecular spaces. To isolate the craze fibril scattering, x-ray patterns from all other sources must be treated as background and subtracted from the observed scattering.

Undeformed polymer material, maintained at the same temperature as the deformed polymer, was used as a source for background correction. In most cases this came from a separate piece of identical sample material, placed adjacent to the sample undergoing deformation. Scattering patterns were obtained from this material prior to the beginning of each crazing experiment so that, in addition to a background correction, the sample to be tested could be checked for initial damage. This background data was compensated and binned in exactly the same manner as was done for the sample data. A preliminary check of both background and sample data was possible through a comparison of the background

data with the prestress data from the sample. For a few cases where this background measurement was unavailable or corrupted, the first few measurements on the sample prior to its deformation were used. Due to the systematic differences observed in opposite angles, separate background corrections were produced for both angles. In this way, each sample was assured of its own unique background correction to avoid systematic errors.

Smoothing was done to the background data to avoid significantly increasing the error in the intensity values of the sample data. This was divided into three parts as no single smoothing algorithm could deal adequately with the entire intensity range. At the lowest q values corresponding to data below the beamstop edge no smoothing was done. Low-q data, where intensity changes are rapid, were smoothed using the Savitski-Golay algorithm with zero degree.[72] At large q values, the data was smoothed using locally weighted least squares.[73] The data supplied to both algorithms for smoothing included a buffer region above and below the range of interest to ensure a smooth transition between regions.

A comparison of smoothed background scattering intensities to the original intensities on both linear and logarithmic scales (figure 6.3) shows a consistent representation of the original data in the smoothed curve. Examinations of background-subtracted data at low strain values (prior to the formation of craze structure) were performed to ensure accuracy; no systematic deviations from zero scattering intensity were observed. Due to the complexities involved, no error calculations were performed.

6.4 Volume Contribution

The invariant, discussed in section 3.6.1, is related to the volume of material which contributes to the scattering. It is used as a parameter in the Porod models which provides a measure of the size of particles. The true invariant cannot be determined from the scattering data, so an approximate effective invariant is used. This effective invariant provides a measure of the volume of the particles which contribute to the scattering within the q range examined and, thus, it is valuable to examine it more closely to gain insight into the relative contributions to the scattering volume from different lengthscales. This is done by

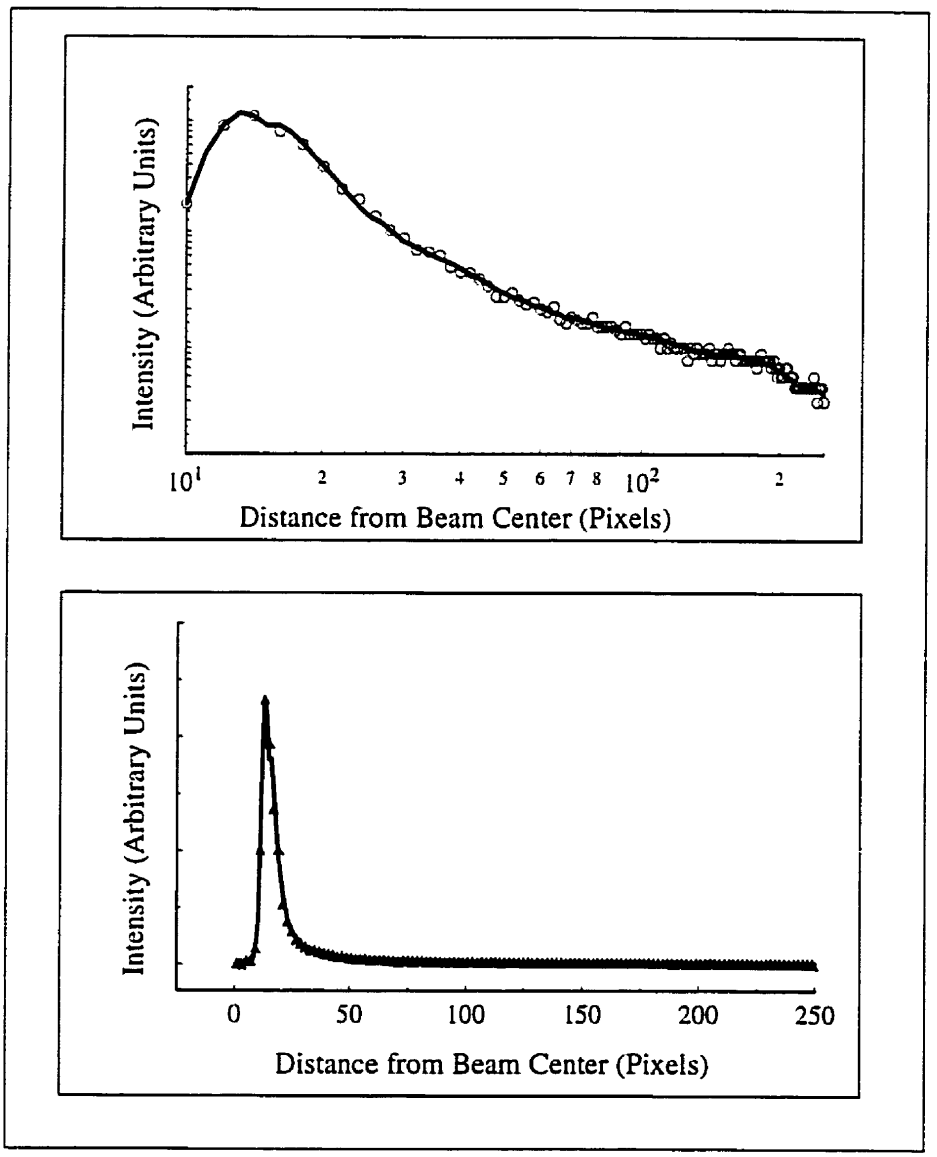

Figure 6.3: Background data in the high-q range showing smoothing on both linear and logarithmic scales with the solid line indicating the smoothed data. (Data for HIPS at 42.5° C.)

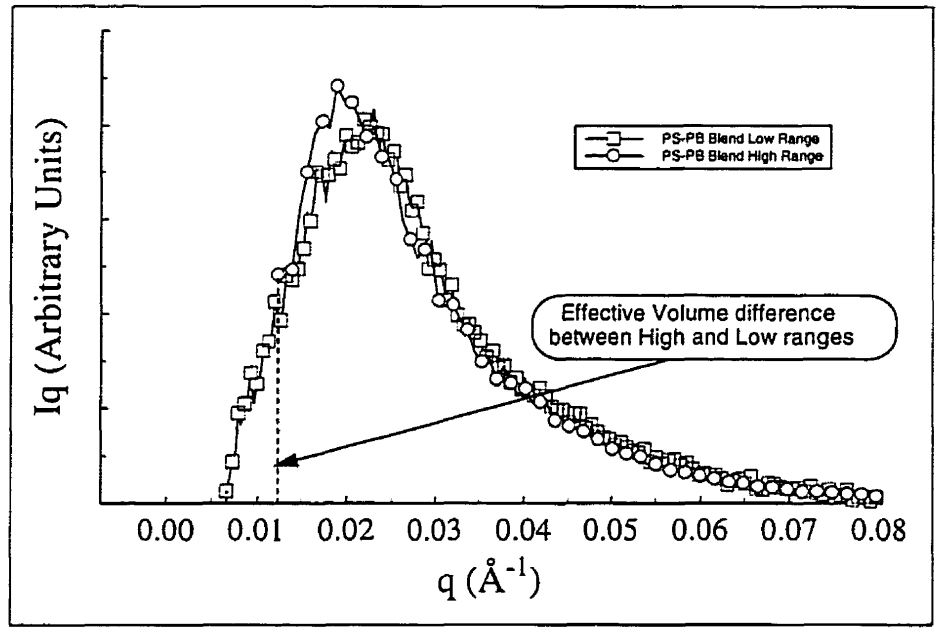

Figure 6.4: Volume plots for high-q (○) and low-q (□) range data, indicating the difference in the effective invariant calculated for these two ranges. (Data from PS-PB blend samples at 67.5° C and 65° C.)

creating volume plots which are graphs of intensity $(I)\times q$ vs. q. The area under such a curve is the effective invariant.

Typical volume plots for the PS-PB blend material are shown in figure 6.4. From these plots it can be seen that the volume contribution from different lengthscales contains a well-defined peak at $q \approx 0.02$ and reduces to near zero at the low-q cutoff.

There are two scattering ranges in use which implies two different low-q cutoff values. Since the $I \times q$ values are not zero at the low-q cutoff point, there will be a systematic difference between the invariant values calculated for the low-q range data and those calculated for the high-q range. Examinations of the volume plots suggest a difference of about 10%. Unfortunately, there were far less measurements done at the low-q range and so this data is insufficient to provide direct corrections to the effective invariant calculations.

6.5 Deformation Mode Parameters

Prior to the interpretation of the scattering data in terms of models of craze structure, it is necessary to confirm the appearance of craze formation and growth stages in the deformation process. No single measurable parameter, however, is sufficient proof of active crazing and therefore a combination of several different measurement techniques are required to ensure that the craze growth deformation mode is properly identified. The three measurements used here to aid in identifying deformation modes are those of applied stress, x-ray transmission and x-ray scattering invariant.

6.5.1 Applied Stress

An examination of the relation between applied stress and resulting strain (figure 6.5) allows for initial identification of deformation modes.

Elastic deformation, defined as a reversible strain response to applied stress, is typically identified with the linear low-strain portion of a stress-strain curve. Such linear stress-strain behavior was observed for a large portion of the total strain. In some cases, notably at temperatures below 50° C, the slope of the stress-strain curve would suddenly decrease and yet remain linear. This suggests that the linear strain behavior is not purely elastic. However, there is currently no suitable method for measuring strain relaxation under the experimental conditions imposed here. Therefore, the existence of elastic deformation cannot be directly verified in this data.

As the strain progressed, the samples would typically reach a yield point defined here as the maximum stress point in the stress-strain curve.[15] In general, the maximum applied stress at the yield point was 10–20% larger in the PS-PB blend than in the HIPS material. For many samples, most commonly the PS-PB blend, no stress peak was observed, rather, the linear stress-strain behavior continued for the entire deformation process. Such observations were interpreted as indicating that insufficient strain was applied to these sample for it to reach its yield point.

Beyond the yield point, the two samples behaved quite differently. In the PS-PB blend

a sharp decrease in stress followed the yield point after which sample failure generally occurred. In the HIPS material a slight decrease in applied stress followed the yield point, after which the stress remained relatively constant for some time, indicating extensive plastic deformation.

6.5.2 X-ray Transmission

With each x-ray scattering image observed, ratios of x-ray intensity entering and exiting the sample (τ) were determined. As described in equation 6.2, two processes could affect this ratio: a change in sample thickness or a change in sample density.

$$\tau = I_{out}/I_{in} = e^{-(\frac{\mu_x}{\rho})\rho z} \tag{6.2}$$

where I_{out}/I_{in} is the ratio of transmitted intensity to the incident intensity, ρ is the density, z is the sample thickness, and $\frac{\mu_x}{\rho}$ is an x-ray mass absorption coefficient.[38]

A parameter $\widehat{\rho z}$ is introduced here, which will be called the reduced thickness-weighted density. It was determined from the transmission ratio measurements by

$$\widehat{\rho z} = \frac{\ln(\tau)}{\ln(\tau_o)} = \frac{\rho z}{\rho z_o} \tag{6.3}$$

where τ_o and ρz_o are the transmission ratio and thickness-weighted density prior to the onset of deformation.

In situations where constant sample density may be assumed, such as during elastic and shear deformation, $\widehat{\rho z}$ reduces to $\epsilon_2 + 1$ with ϵ_2 being the strain in the direction of the x-ray beam. For elastic deformation, this strain component is related to the strain in the tensile direction (ϵ_3) by

$$\epsilon_3 = -\nu\epsilon_2 \tag{6.4}$$

where ν is Poisson's ratio. Calculations of Poisson's ratio for data at low strain levels gave values of about 0.03. In contrast, a Poisson's ratio of 0.5 indicates constant volume deformation.[27]

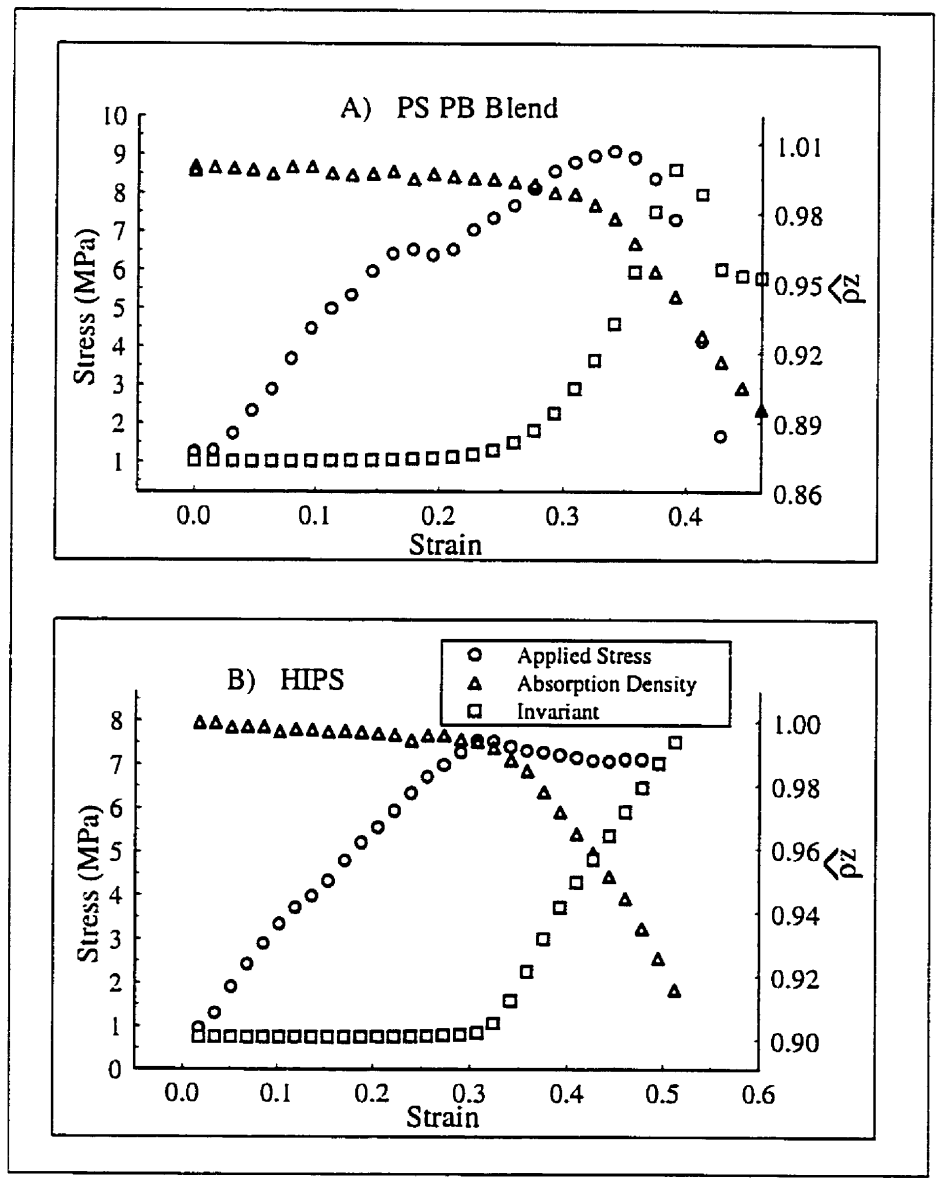

Figure 6.5: Applied stress(○), $\widehat{\rho z}$(△), and invariant(□) curves for PS-PB blend at 67.5° C (A) and HIPS at 57.5° C (B)

It is more precise to interpret the parameter $\widehat{\rho z}$ as a ratio of the number of electrons in the beam path at any given time, $N_e(t)$, to the initial number of electrons in the beam path, $N_e(0)$,

$$\widehat{\rho z} = \frac{N_e(t)}{N_e(0)}. \tag{6.5}$$

At the onset of craze or other void formation, regions of empty space are formed and electrons are moved out of the beam path. In crazes, the volume fraction of empty space has been shown to remain constant,[3] and therefore, the number of electrons displaced may be given by:

$$N_e(t) = N_e(0) - v_f V_{cr}(t) \tag{6.6}$$

where $V_{cr}(t)$ is the craze volume at a given time t and v_f is the volume fraction of the craze fibrils.

During the initial formation of crazes, the relation between the craze volume and the macroscopic strain is quite complex due to non-linear relations between craze growth in the tensile direction and in lateral directions.[28] As the crazes expand, however, they will begin to encounter other crazes or the polymer surface. At this point, lateral craze growth stops and the craze volume expands purely by the lengthening of the craze fibrils, giving a linear relation between $\widehat{\rho z}$ and the macroscopic strain. Such linear relations are observed at large strains (figure 6.5).

6.5.3 Invariant

The effective invariant, described in section 3.6.1, provides an indication of the volume of the scatterers. The anisotropic nature of craze fibrils requires a modified version of the invariant, described in section 3.7. An effective invariant may be calculated for the data by:

$$Q_f = \delta q \sum_{i=1}^{n} q I_f(q), \tag{6.7}$$

where $I_f(q)$ is the background-subtracted intensity in the craze fibril direction, δq is the pixel-to-q conversion factor, and the sum is over all valid data points. For the purposes

used here, no corrections are attempted for the finite upper and lower q limits as these are highly model-dependent and changes in the invariant, rather than absolute numbers, are of interest here.

In the case of polymer deformation, the scattering is due to the electron density contrast between polymer matter and voids within the material. The invariant, therefore, will not respond to shear deformation but will indicate the presence of dilatational strain due to crazes and voids. Thus, the onset of changes in the invariant may be interpreted as the onset of craze formation. The invariant begins to increase shortly before the stress maximum is reached in the HIPS materials. In the PS-PB blend materials, the invariant begins to increase at about the midpoint in the linear stress regime.

The anisotropic invariant of equation 3.30 is related to the number of craze fibrils, their cross-sectional area, and their length. Since the fibrils maintain a constant diameter during deformation, their cross-sectional area does not contribute to changes in the invariant. At later stages of craze growth, no new fibrils will be created and changes in the invariant should be proportional to the square of the length of the craze fibrils.

An additional factor affecting the invariant, however, is the loss of craze material outside the irradiated area as the material expands. Following similar arguments to that of section 6.5.2, the amount of craze fibril within the region of observation decreases linearly with strain, resulting in a complex relation between the invariant and strain. Near the large strain limit, the amount of new fibril formed will approach the amount of fibril material leaving the observed region, causing the effective invariant to approach a constant value. This is observed in some of the HIPS materials.

Three parameters, applied stress, $\widehat{\rho z}$, and effective invariant which directly contribute information regarding the deformation process have been calculated. An examination of the changes in these parameters shows that craze formation occurs in both sample materials under investigation. In chapter 8 these changes will be examined in more detail to map out the deformation history for both materials.

With the confirmation of the presence of crazes in the samples, the craze fibril scattering

data which had been isolated previously may now be examined with confidence. The analysis of the fibril scattering data will be described in chapter 7 where several different models will be applied to interpretation of the data.

Chapter 7

Data Analysis

The previous chapter described the calibration of the SAXS data, the identification of the craze fibril scattering band, and the background subtraction procedure used to isolate the craze fibril scattering from other sources. Having done this, the resulting x-ray scattering data may now be interpreted in terms of craze fibril structures.

To begin with, the overall fibril scattering pattern will be examined to obtain relevant lengthscales and general structural features. This will be followed by an application of Porod's law to identify details of the craze fibril structure. Finally, the results from Porod's law will be compared with results from other SAXS analysis techniques.

7.1 Identification of Relevant Scattering Lengthscales

The interpretation of SAXS data, as described in chapter 3, is highly model-dependent. Due to approximations made in both the assumed structure under investigation and the resulting scattering pattern, the models in most common use do not apply to the entire x-ray scattering pattern, but are limited to specific angular regions. Analysis therefore involves a search for peaks on the background-subtracted data followed by an examination of log-log plots of the data to identify regions in the scattering data corresponding to distinct structural details.

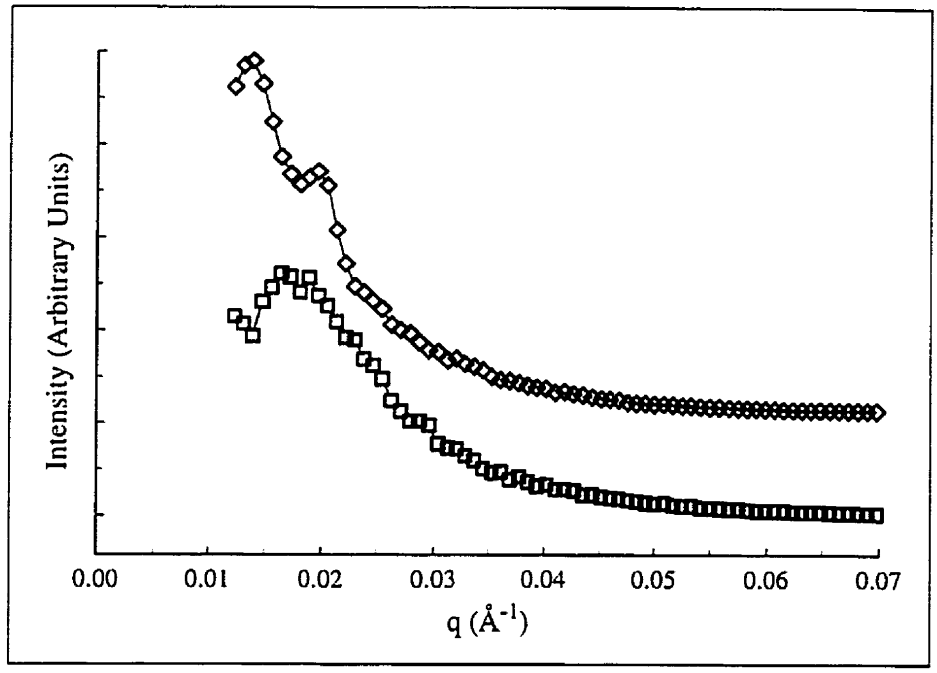

Figure 7.1: Scattering data showing a peak in the PS-PB blend material at 67.5° C (□) and a shoulder in the HIPS material at 45° C (◇). In both cases the data is from the high-q range at a 40% strain.

7.1.1 Scattering Peaks

The most readily accessible information which can be obtained from x-ray diffraction data is the location of observed peaks. A search for peaks, Bragg-type or otherwise, is therefore, a reasonable place to begin in interpreting the scattering from a given structure.

Scattering data from deformed HIPS and PS-PB blend material is shown in fig. 7.1. A peak could clearly be observed between $q = 0.015$ and $q = 0.02$ Å^{-1} in scattering data from deformed PS-PB blend material at both the low-q and high-q ranges. This corresponds to distances of 200–300 Å. In addition, several other weak peaks appear to be present at higher q values. The HIPS data contains possible peak structures at similar q values, however, these were broader and tend to appear as shoulders rather than as well-defined peaks.

The locations of the high-q peaks were compared to the flood-frame data used for intensity corrections (section 6.2.1). This comparison revealed that the peak positions are

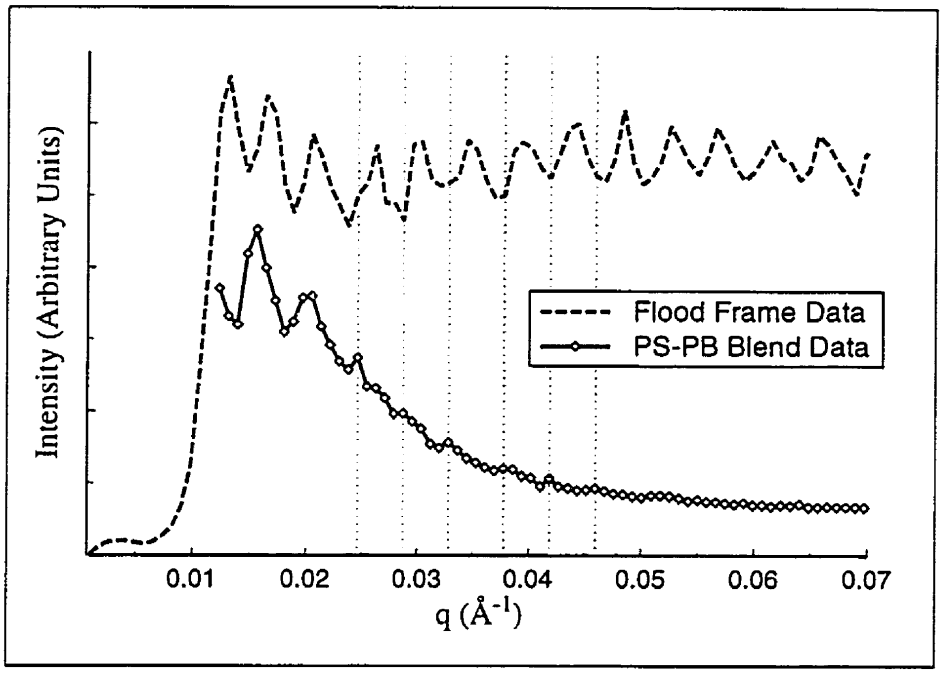

Figure 7.2: Detector compensation data (dashed line) compared with scattering peaks in the high-q range from PS-PB blend material ($\diamond$) at 55° C. The dotted lines indicate the locations of the high-q peaks in the PS-PB blend data.

consistent with the wire pattern in the detector, an effect which has been previously noted in the literature.[70] The location of the large peaks at low-q values were observed to occur at similar q values in the data from both q ranges and do not follow the pattern observed among the high-q peaks, however, it is conceivable that the wire patterns are affecting these peak locations as well.

There is no evidence of long range order between the craze fibrils, and their isotropic nature precludes the use of the interpretation of short range ordering, provided by Klug and Alexander.[42] A standard Bragg interpretation of the low-q peaks is therefore used to obtain approximate near neighbour distances.

In the background-subtracted data for a few of the PS-PB blend samples, small but systematic negative intensities at q values greater than 0.07 $Å^{-1}$ were observed. This is best explained as due to a slight orientation of the polymer chains occurring as a result of shear and crazing deformation. This orientation will cause the polymer chains to exhibit

a small degree of short range ordering, reducing the amount of scattering at the larger lengthscales and resulting in negative intensities in the background-subtracted data. The location of these effects at the extreme high-q end of the data, where signal-to-noise ratios are poor, inhibits a systematic search for peaks relating to this process. The reason this was observed in only a few samples is believed to be due to irregularities between samples. In conclusion, the locations of low-q peak structures are used to infer approximate fibril spacing distances while detector-based inconsistencies preclude systematic interpretation of the possible high-q peak structures.

7.1.2 Power Law Regions

Log-log plots of the data were generated to identify scattering associated with particular data structures, such as rod, fractal, and Porod regions. This is accomplished through an initial cursory examination of the general trends in the scattering intensity. It was observed that the x-ray scattering curve could be divided into 3 regions, as illustrated in fig. 7.3. The first (low-q) region had a slope of -1 or shallower; the middle region's slope was between -3 and -4 and the slope of the third region was steeper than -4. The observed peaks, mentioned previously, do not change the trend of the monotonically decreasing intensity.

At this point a digression to clarify terminology is deemed prudent. As described at the beginning of this chapter, x-ray scattering measurements were taken with the detector in two different positions, giving scattering patterns in what will be termed high- and low-q ranges. The actual q values spanned by the two ranges overlapped considerably. Different ranges refer to distinct experiments performed at different times. Individual scattering patterns could be readily separated into 3 distinct regions based on their slopes in a log-log plot. The dividing point between low-, intermediate-, and high-q regions was independent of the total q range (sample-to-detector distance) under examination.

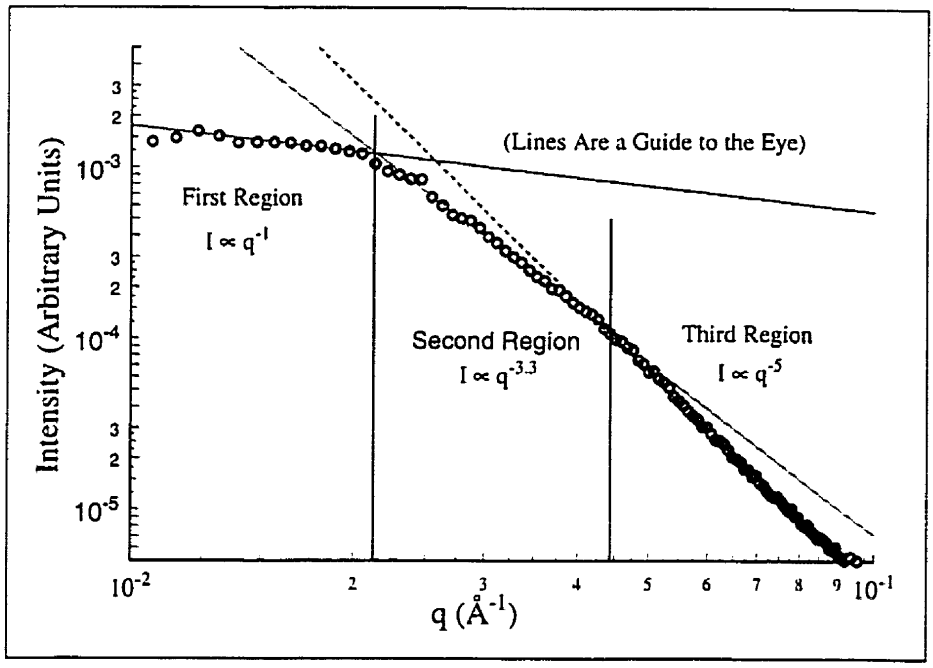

Figure 7.3: A typical log-log plot for HIPS data showing the three linear regions. (Data from high-q range at T=47.5° C.)

q Range	1st Region	2nd Region	3rd Region
Low-q	100	150	120
High-q	20	60	65

Table 7.1: Approximate number of data points in each data range

7.1.3 Fitting to Identify Regions

The three identifiable q regions were fit to a segmented power law equation to confirm the slopes observed on the log-log plots and to systematically isolate particular regions for more detailed study. The fitting was done using the SAS^{TM} statistical analysis package Release 6.09, with a custom-designed fitting algorithm, employing the grid search technique applied to a three section linear equation in which two breakpoints (where the curve changes slope) are defined. The approximate number of data points in each range is given in table 7.1. More details on the fitting methodology are given in appendix D.

To examine the validity of the fitting technique, residuals were examined from the power-

law fitting before and after the introduction of the breakpoints. Prior to the introduction of the breakpoints into the data, clear changes in the residuals could be observed (figure 7.4A). After the two breakpoints were included in the fitting, the residuals remained constant, showing no systematic trends (figure 7.4B). This indicates that the inclusion of the two breakpoints is necessary and that the model provides a good description of the data.

A few extreme residual values (on the order of 5 points out of 200) were observed. It is possible for the corresponding anomalous data points, known as outliers, to have a severe effect on the fit parameters. These points are, therefore, examined more closely.

Outliers can come from several sources: incorrect detector operation resulting in extremely large or small intensity values, peaks in the data, or from the transition area between power law regions. The outliers occurred at extreme low- and high-q values and thus could not be due to either the observed peaks nor the transition regions. These outliers are, therefore, most likely due to detector effects such as scattering from the beamstop and can clearly be discarded. The fitting was repeated with the outliers excluded from the data resulting in no significant change to the fit parameters. This indicated that the effect of the outliers need not be a concern in further model fitting of this data.

As noted in section 6.2.4, a systematic difference in scattering at opposite angles was observed. The same direction was found to consistently give better $\overline{R^2}$ values than did its opposite. This points to an unknown systematic error in the experimental setup. In order to appropriately weight the fitting results while tracking the level of deviation, a variable was included in the fit model which indicated which of the two opposite angles a given data point came from (see appendix D for more details). This variable was either 1 or 0 depending on which angle a particular data point was associated with. Perfectly symmetric data would then result in a value of zero for the parameter associated with this variable, while a non-zero value indicates a significant systematic difference between the two opposite angles.

Tests of the angle parameter indicated that prior to the removal of the outliers the probability of it being zero (the ideal case) was greater than 10%. A probability less than

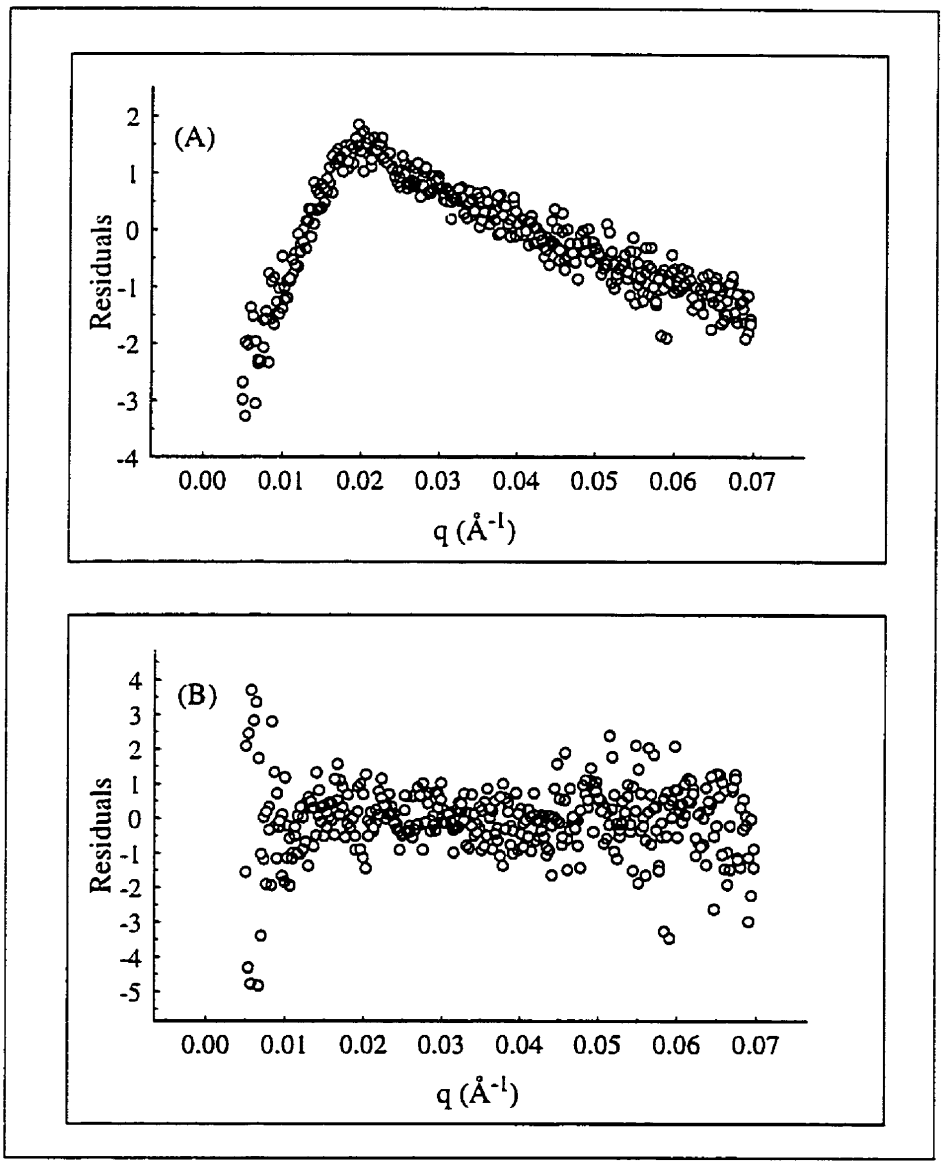

Figure 7.4: Plots of the residuals from the segmented power law fitting before (A) and after (B) the inclusion of the breakpoints. (Data for HIPS low-q range at 70° C.)

Material	1st Region	2nd Region	3rd Region
HIPS	$\alpha \approx 1.02 \pm 0.65$	$\alpha \approx 3.39 \pm 0.30$	$\alpha \approx 4.88 \pm 0.55$
PB	$\alpha \approx 0.03 \pm 0.55$	$\alpha \approx 3.11 \pm 0.37$	$\alpha \approx 4.48 \pm 0.79$

Table 7.2: Weighted averages of the values of α for HIPS and PS-PB blend samples based on the equation: $I \propto q^{-\alpha}$

5% implies that a statistically significant asymmetry in the data indicating that the variable must be included for accurate weighting. After the outliers were removed, the probability of the angle parameter being zero dropped to less than 0.1%. The change in the significance of the angle parameter with the removal of the outliers, indicated a systematic difference in the data quality between the two opposite angles, probably due to scattering from the beamstop. The weighting of the fit results by the introduction of the angle parameter allows the data from both angles to be used while avoiding the possibility of misleading parameters which would result if the data from opposite angles were simply averaged.

The locations of the two breakpoints obtained from the segmented regression procedure were observed to be generally independent of strain. A small but distinct decrease in both breakpoints could be observed as a function of sample temperature. This decrease was of the same magnitude for both breakpoints and in both materials. It can be understood in terms of an increase in the fibril diameter with increasing temperature; and is discussed in more detail in chapter 8.

Weighted averages of the power law exponents obtained from the segmented regression for all data are given in table 7.2 and are used to provide an indication of general trends. These values confirm the observations made from the log-log graphs. It should be noted that in a few cases the scattering from a HIPS sample corresponded to that from a typical PS-PB blend sample and vice versa. Since the deformation process is highly statistical in nature, such occurrences are not unexpected.

Porod's law for oriented rods, described in section 3.6.3 predicts that at high-q the scattering intensity should be proportional to q^{-3}. As can be seen from table 7.2, scattering intensities in the second region tend to follow this form. The first region is clearly not asso-

ciated with Porod-type behavior, as expected for low-q scattering. A Porod interpretation of the third region cannot be ruled out at this point. For this reason, the second and third regions will be examined further in the context of Porod law analysis. The large deviations from Porod's law, observed for the third region are considered in chapter 8 along with a more detailed discussion of the interpretation of the different scattering regions.

The samples being examined initially contained no craze structure and thus, after background subtraction, the scattering pattern contained no regular structure. It is only during the course of the deformation that craze structure was formed resulting in the observed scattering pattern. In order to compare the models in a meaningful way, it is important to identify the point in the strain progress at which the craze structure first appears.

Upon the advice of Dr. J.T. Smith[74] of the Queen's University STATLAB, a systematic identification of the point of craze structure onset has been developed. The three standard deviations associated with the α parameters obtained from the breakpoint fitting procedure exhibit a sharp decrease at the same strain point before leveling off to a relatively constant value at larger strains. The point of sharp decrease is considered to be the onset point for craze structure. Of the three standard deviations the ones associated with the third region are selected, as they are quite consistent among all of the samples. It was also felt that, since the following data analysis was going to focus on the second region, the values from this region should not be used to avoid the possibility of a subtle bias.

The standard deviations from the third region are initially greater than 1.5 and decrease to values of about 0.5 beyond the point of craze structure onset. To ensure that all relevant data was applied to the subsequent model fitting a cutoff of value of 1.0 was chosen. Data with standard deviation values for the third region greater than 1.0 were considered to be without craze structure and thus not applicable to the craze fibril model fitting to follow.

7.2 Application of Porod's Law

As discussed in section 7.1.3, the data in the second region may be associated with Porod Law scattering for oriented rods. The power law values obtained, however, are not obviously

consistent with the ideal value of 3. A modified Porod's law model is, therefore, needed to account for the non-integer power law exponents observed. The traditional modification to Porod's law used when examining craze structure involves the addition of a *Constant Background* term.[1,2,5,57] This background term is attributed to structure within the fibrils due to the conformation of the polymer chains and has its basis in the fact that at relatively large q, scattering from a complex object containing no long range order should be independent of q.[46] Such a positive background term should give rise to a decrease in the α value associated with the scattering slope (positive deviations from Porod's law), whereas, the actual scattering slopes observed gave larger values of α (negative deviations from Porod's Law). The effects on the fibril diameter values obtained through a misapplication of the *Constant Background* modification of Porod's law will be discussed in section 8.3.2. Since the data obtained in this study were observed to contain negative deviations from Porod's law, it seems advisable to apply diffuse boundary variations to Porod's law.

7.2.1 Diffuse Boundary Models

As discussed in section 3.6.5, Koberstein et al.[55] describe a variation to Porod's law for negative deviations. Their *Sigmoidal-Gradient* model results in an intensity relation of the form:

$$I = Kq^{-3}e^{-q^2\sigma_s^2/2} \tag{7.1}$$

with I, q, and K being the intensity, scattering angle and Porod constant respectively, and σ_s describing the distance from the nominal particle boundary to the point at which the density is 0.856 of that at the center of the particle — the standard deviation of a Gaussian distribution.

To examine the applicability of this model to craze structure, graphs of the form $\ln(Iq^3)$ vs. q^2 (figure 7.5) were generated for the second and third regions of the data. These graphs indicated that the model describes the data quite well using the breakpoint obtained from the power-law fitting.

Another variation on Porod's law for negative deviations may be obtained by following

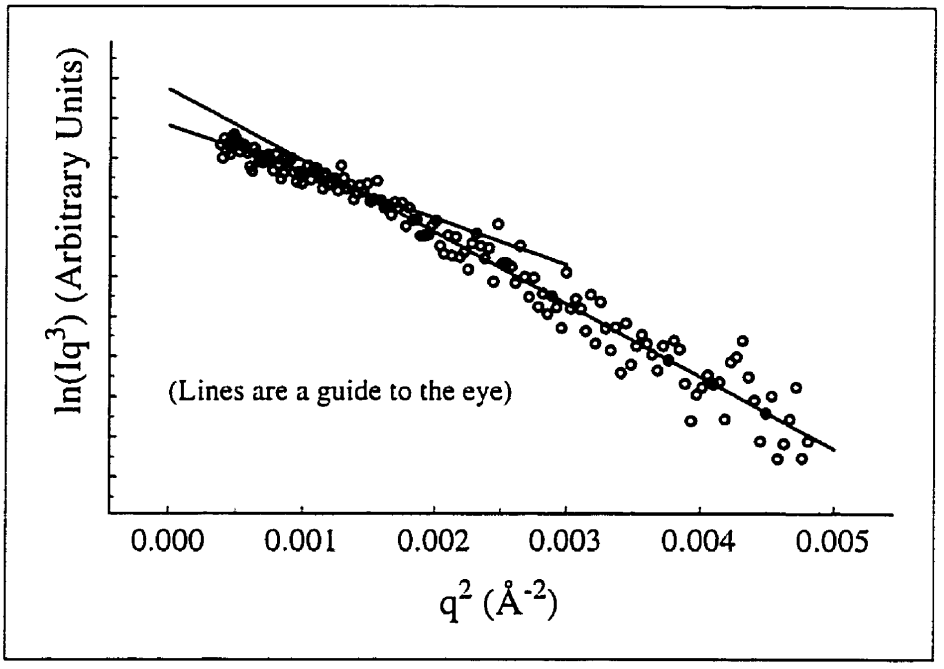

Figure 7.5: *Sigmoidal-Gradient* variation of the standard Porod plot for HIPS at 70° C in the low-q range.

the derivation of the *Sigmoidal-Gradient* model using a limited power-law distribution instead of an exponential distribution to describe the density variations. This model assumes density distributions at the boundary with shapes similar to that shown in fig. 7.6 with the resulting intensity being of the form:

$$I = K^* q^{-5+2\beta} \tag{7.2}$$

β is a fit parameter indicating the sharpness of the boundary, and K^* is related to the mean fibril radius, $\bar{R}_f$, by:

$$\frac{K^*}{Q_f} = \frac{2}{\pi}\left(\frac{(1-\beta)\pi}{2\Gamma(\beta)\cos(\beta\pi/2)}\right)^2 \bar{R}_f{}^{-3+2\beta} \tag{7.3}$$

with Q_f being the invariant, and $\Gamma(x)$ being the gamma function.

The *Power-Law* model of equation 7.2 would appear to be more appropriate to craze

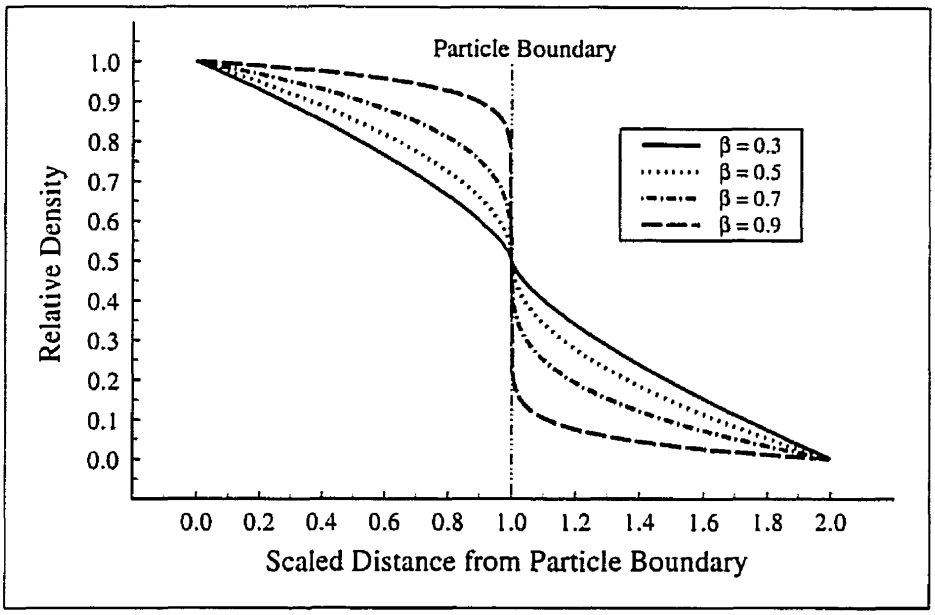

Figure 7.6: Density distributions in the *Power-Law* Model for different values of the β parameter.

fibrils, as the current theory of craze growth[3,4] predicts a power-law strain response to applied stress and a power-law stress gradient from the center of the fibril to the midpoint between fibrils. A full derivation of the *Power-Law* model is described in appendix C.

7.2.2 Model Fitting

The *Power-Law* and *Sigmoidal-Gradient* models were fit to the data using identical fitting techniques, described in appendix D. Fit corrections for opposite angle differences and a test of the validity of the breakpoint were included in both models. $\overline{R^2}$ measurements of the goodness-of-fit were obtained and typically found to be in the range between 0.8 and 0.98, indicating a good fit to the data for both models.

In addition to single model algorithms, an algorithm was also applied which selected between the *Sigmoidal-Gradient* and *Power-Law* models for the second and third scattering regions independently, yet maintained continuity in the intensity over the breakpoint (see appendix D). A comparison of the $\overline{R^2}$ values showed that the *Sigmoidal-Gradient* model best described the data in both regions. The comparison of the $\overline{R^2}$ values provides a method

for comparing models which is intrinsically the same as the well-known F-test.

To further compare the two models, ratios of the $\overline{R^2}$ values were obtained for all data in which craze structure was deemed to be present. Frequency histograms (figure 7.7) were then produced from the ratios for the two different materials, based on approximately 150 separate measurements for each material.

These histograms show that for both materials there is a distinct bias towards the *Sigmoidal-Gradient* model. While this bias is significant, it is not large. In contrast, the histogram of $\overline{R^2}$ values for comparison of the *Sigmoidal-Gradient* and *Constant Background* models (figure 7.8) shows an overwhelming bias against the *Constant Background* model.

To ensure that the bias for the *Sigmoidal-Gradient* model was not linked to $\overline{R^2}$, a plot of $\overline{R^2}$ ratios vs. $\overline{R^2}$ values was produced (figure 7.9) which shows that the $\overline{R^2}$ ratios are independent of the actual $\overline{R^2}$ values. The lack of a trend in figure 7.9 provides confidence that the preference for the *Sigmoidal-Gradient* model is not due to a confounding factor. For example, the lack of a trend proves that the ratios favoring the *Sigmoidal-Gradient* model do not come primarily from the poorer quality data and that the ratios favoring the *Power-Law* model do not come primarily from the data sets with the best $\overline{R^2}$.

7.2.3 Fit Parameters

Mean fibril diameters and diffuse boundary parameters were obtained for the *Sigmoidal-Gradient* and *Power-Law* models. The fibril diameter, $\bar{D}_s$, for the *Sigmoidal-Gradient* model was obtained using the relation:

$$\bar{D}_s = \frac{4Q_f}{\pi K}. \tag{7.4}$$

The fibril diameter D_p from the *Power-Law* model is given by:

$$D_p = \left[\frac{4Q_f}{\pi K^*}\left(\frac{(1-\beta)\pi}{2\Gamma(\beta)\cos(\beta\pi/2)}\right)^2\right]^{(2\beta-3)} \tag{7.5}$$

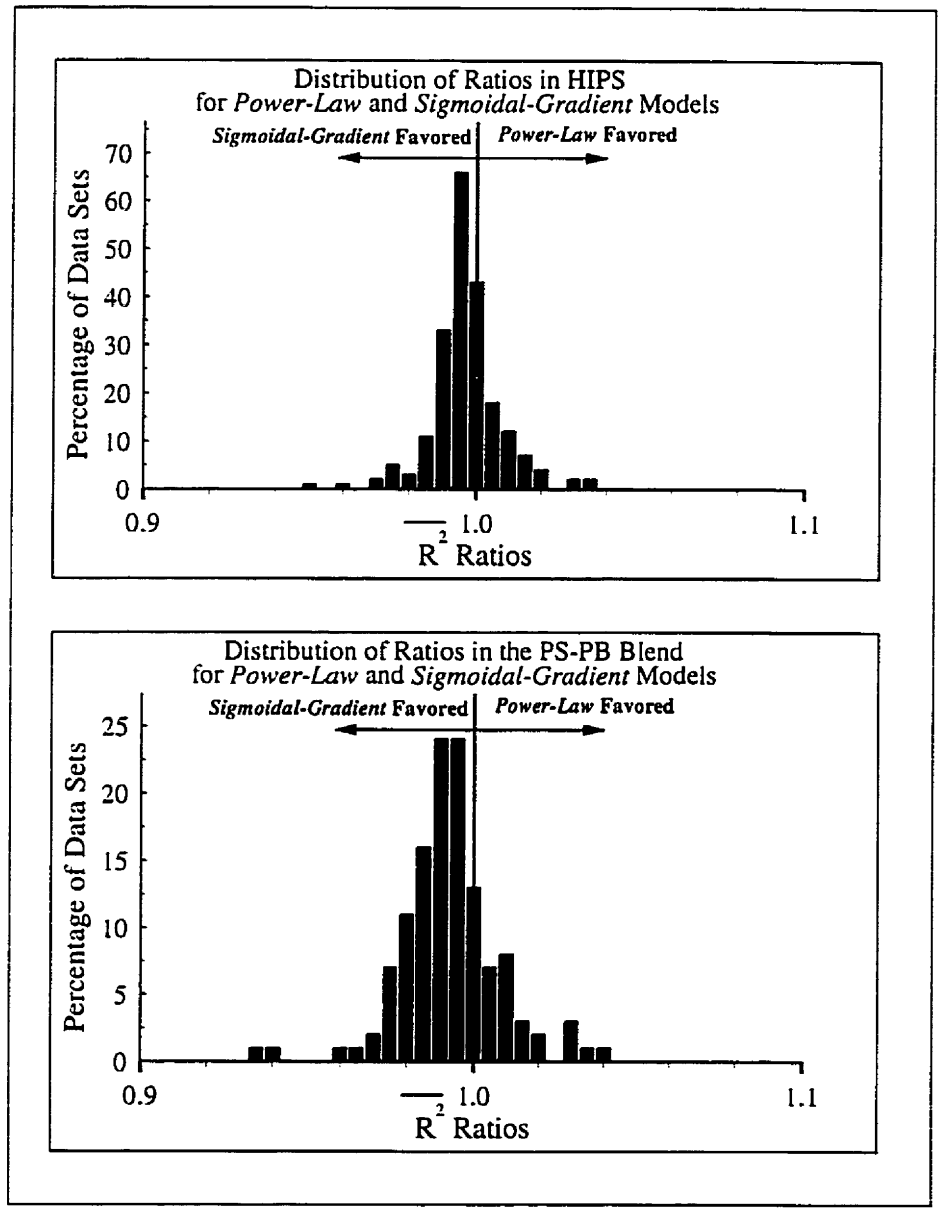

Figure 7.7: Histograms of $\overline{R^2}$ ratios comparing *Sigmoidal-Gradient* and *Power-Law* models for each material

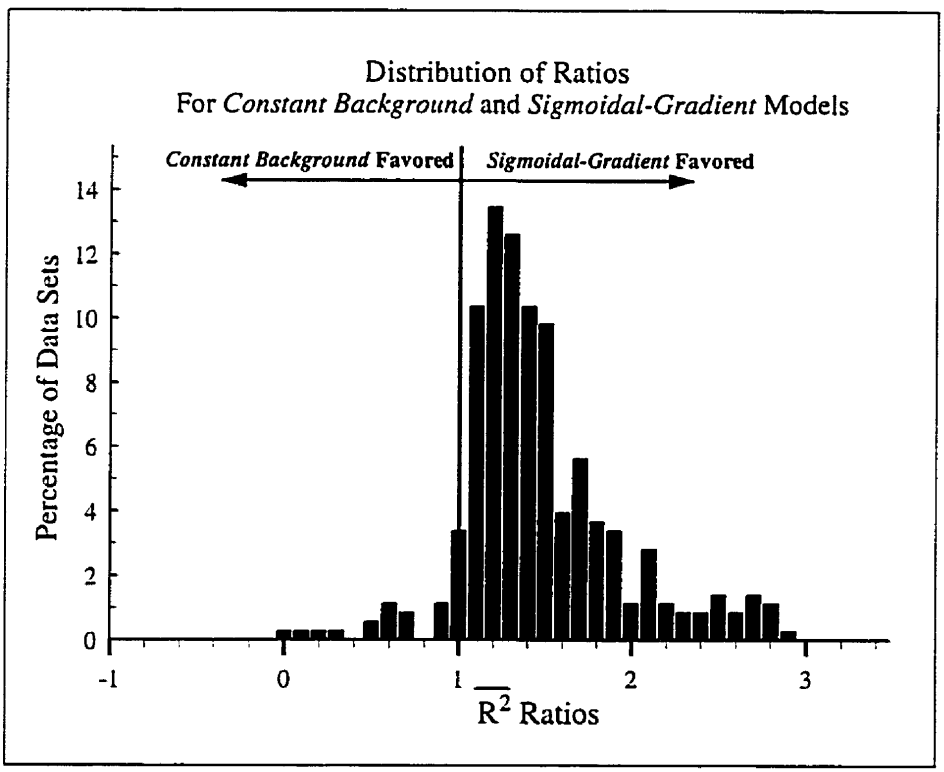

Figure 7.8: Histogram of $\overline{R^2}$ ratios comparing *Sigmoidal-Gradient* and *Constant Background* models.

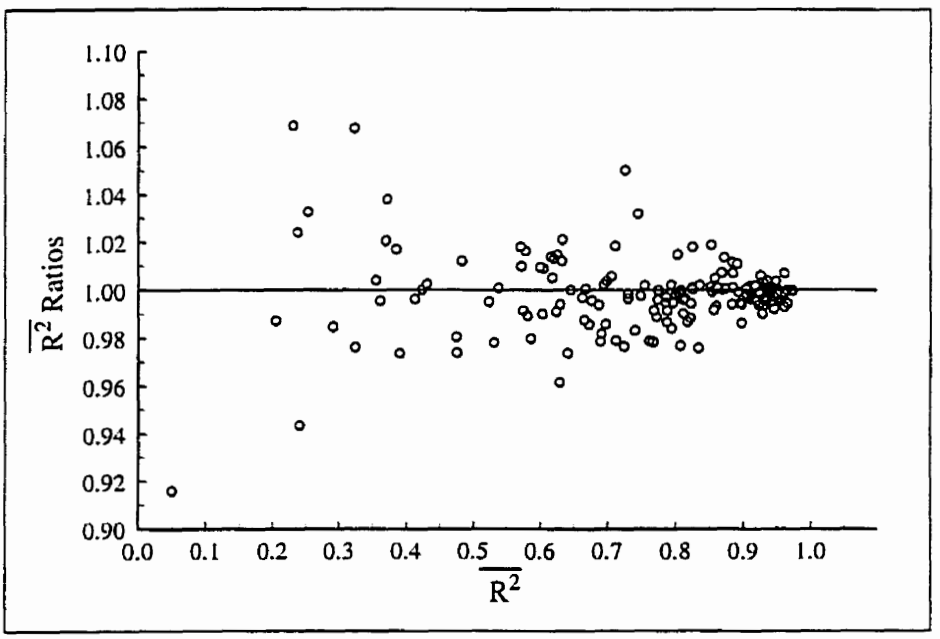

Figure 7.9: $\overline{R^2}$ ratios of the *Sigmoidal-Gradient* and *Power-Law* models plotted by the *Sigmoidal-Gradient* $\overline{R^2}$ values. The lack of a trend indicates that the distribution of the ratios may be assumed to follow a Gaussian distribution and are not biased by the actual $\overline{R^2}$ values.

The invariant, Q_f, used above to calculate $\bar{D}_f$ is defined by equation 3.30. Its value may be approximated from the data by:

$$Q_f = \sum_{q_{min}}^{q_{max}} I(q) q \Delta q \tag{7.6}$$

In this case the accuracy of the calculated invariant is limited by the upper and lower q values of the data, q_{max} and q_{min}. No reliable method has been suggested to correct the invariant for the lack of low-q intensities. Bubeck et al.[17] claim that the low-q correction is negligible, however, as described in section 6.4, volume plots suggest that the correction may be as high as 10% for some of the data. It is possible, as described by Bubeck et al.,[17] to correct for the lack of high-q data by extrapolating the models to infinity. This can be done exactly, for the *Power-Law* model but not for the *Sigmoidal-Gradient* model.

The *Power-Law* model correction to Q_f is given by:

$$(Q_{tail})_p = \frac{K^*}{3 - 2\beta} q_{max}^{(2\beta - 3)}. \tag{7.7}$$

An examination of the magnitude of this correction confirmed that it is on the order of 30%, as reported by Bubeck et al.[17]

It is not possible to obtain an analytic solution for the invariant correction of the *Sigmoidal-Gradient* model. In addition, no references to invariant corrections have been noted in the literature for the *Sigmoidal-Gradient* model,[46,55,75] Therefore, the correction for the ideal Porod's law,

$$(Q_{tail})_s = \frac{K}{q_{max}}, \tag{7.8}$$

was applied. This correction results in a slight over-estimation of the fibril diameters because intensities which follow the *Sigmoidal-Gradient* model will fall off more rapidly, and thus have smaller Q values than predicted by Porod's law.

As shown in fig. 7.10 the fibril diameters obtained from the *Sigmoidal-Gradient* model are significantly larger than those obtained for the *Power-Law* model. This is to be expected due to the high-q corrections to the invariant, as described above.

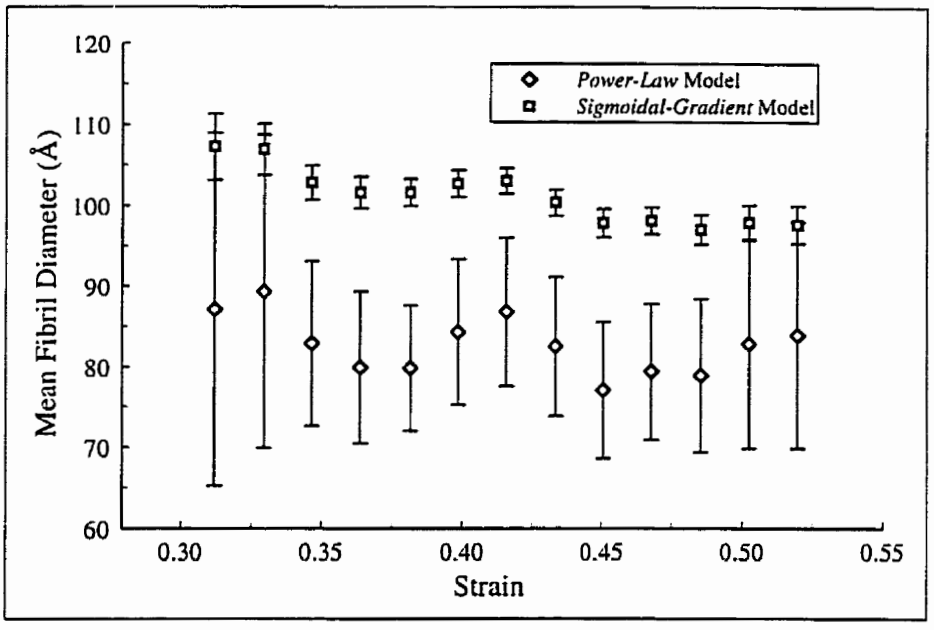

Figure 7.10: Fibril diameters obtained from the *Sigmoidal-Gradient* model (□), and the *Power-Law* model (◇). Data taken at the high-q range for HIPS at 30° C.

The errors in the fibril diameters are significantly larger for the *Power-Law* model than for the *Sigmoidal-Gradient* model. This is believed to be due to the way in which the models weight the different parameters. An examination of the equations for the fibril diameters (equations 7.4 and 7.5) show that the calculations for D include the β parameter in the *Power-Law* model, providing more opportunity for error propagation effects.

The trends observed in the fibril diameter values obtained from the two models are similar. However, *Power-Law* model results are believed to be more accurate due to the better invariant correction and they will be used for comparisons to values obtained from other models. The higher precision of the *Sigmoidal-Gradient* model makes it useful for examining trends in the fibril diameter which are not discernable with *Power-Law* model results.

As described in section 3.6.4, a correction must be applied to the fibril diameters as a result of the Babinet principle. The accepted value of 0.25^3 for the fibril volume fraction in PS based materials was used. This results in an increase in the final values of the fibril

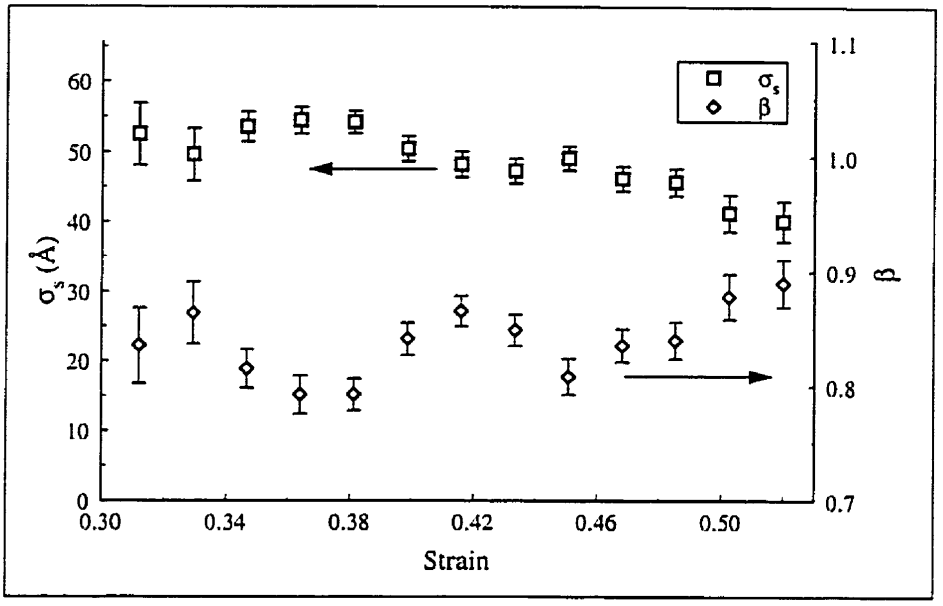

Figure 7.11: Diffuse boundary parameters: σ_s (□), from the *Sigmoidal-Gradient* model, and β (◇), from the *Power-Law* model. Data taken at high-q range for HIPS at 30° C.

diameters by a factor of 4/3.

A direct comparison of the diffuse boundary parameters obtained from the two models is not possible. The β parameter from the *Power-Law* model measures the steepness of the decrease in the density at the particle boundary, while the σ_s parameter from the *Sigmoidal-Gradient* model measures a width which describes the thickness of the region in which the density is changing. It is, however, possible to compare trends in the parameters. The graph in figure 7.11 illustrates a typical variation in the two parameters as a function of strain. In both cases the parameters indicate a trend toward sharper boundaries as the deformation progresses.

7.3 Comparison to Other Analysis Techniques

As mentioned previously, the analysis of SAXS data is highly model-dependent; this means that an alternate technique for measuring the fibril diameters would be valuable. Electron microscopy allows one to examine structure at these lengthscales, however, the necessary

process of microtoming and staining often destroys the fibril structure one is trying to examine. Acoustic measurement techniques can measure structures on this lengthscale without damaging the material, but these techniques are much more indirect than x-ray scattering and suffer from more serious model-dependent weaknesses than SAXS analysis.[76,77] With the lack of a suitable alternate measurement technique, the next best thing is to select alternate and independent analysis methods for the same data. This is done here.

7.3.1 Failure of Guinier Analysis

The technique of Guinier analysis is one of the most popular methods of SAXS data interpretation. It therefore is reasonable to examine its applicability to the study of craze structure. One of the primary weaknesses in the Guinier model is its sensitivity to interparticle interactions. This model is best used in situations of dilute particles in solution. In the present situation, the fibrils are far from dilute, as evidenced by the need to apply the Babinet principle.[41] In addition, the peaks at low-q values suggest that there are strong interfibril interactions. All of this evidence suggests that Guinier analysis is not appropriate for the study of craze structure, although, several groups[25,65] have used it for measuring craze fibril sizes. Therefore Guinier analysis will be attempted here for the sake of completeness.

Guinier's law states that, at low-q values, the relation between intensity and q follows the form given in equation 3.6.2, implying that a graph of $\ln(I)$ vs. q^2 should be linear. When such graphs were produced (figure 7.12), two linear sections were observed; the first being from $q \approx 0.015$ to $q \approx 0.03$ and the second from $q \approx 0.035$ to $q \approx 0.05$. It should be noted that the first section borders on the region used for Porod analysis and the second is inside the Porod region. It is generally expected that Guinier regions should be located at q values significantly lower that those used for Porod analysis.

The Guinier model was fit to both sections, giving R_g values of 60–70 Å for the first section and R_g values of 45–50 Å for the second section. To compare the R_g values from Guinier analysis to the fibril diameter obtained from Porod analysis, one needs to convert

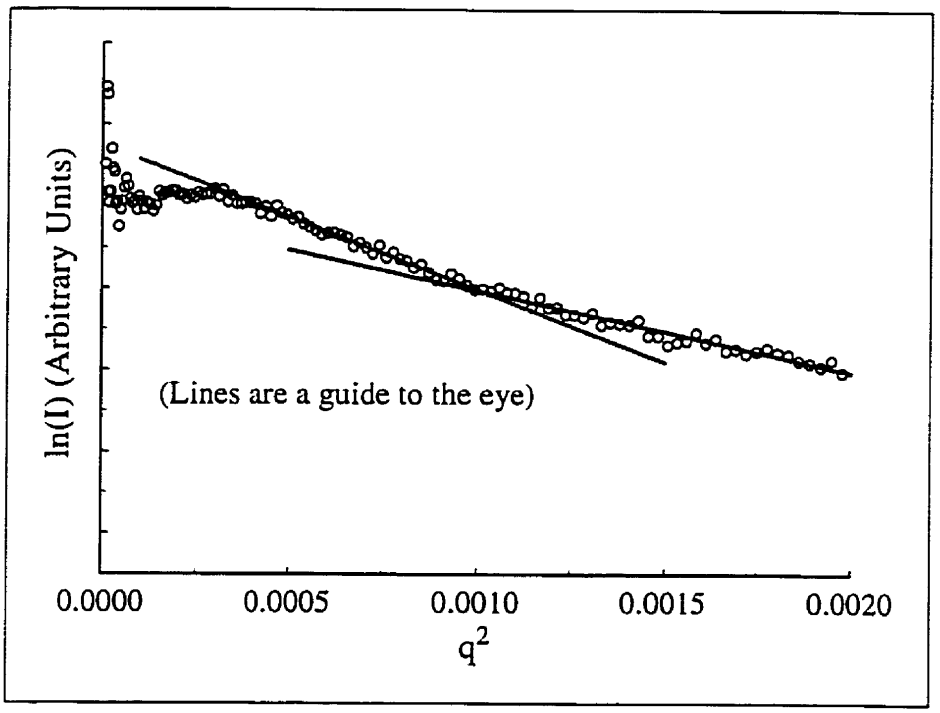

Figure 7.12: Guinier plot showing the two linear regions. Data from HIPS at 55° C in the low-q range.

radius of gyration to diameter. For an ideal cylinder, the relation can be calculated as:

$$D = 2\sqrt{2}R_g \tag{7.9}$$

For a cylinder with a diffuse boundary, the conversion cannot be determined analytically and numerical calculations were done to determine the conversion factor.

A comparison of the fibril diameters obtained from Guinier analysis to those obtained from Porod analysis shows that the Guinier R_g values obtained from the first section are about a factor of 2 larger than the values obtained from Porod's law, and the R_g values from the second section gives values which are about 20% higher (table 7.3).

The relationship between the Porod and Guinier models was examined by generating artificial data using Porod's law with a power-law diffuse boundary and parameters typical of the data. This artificial data was then fit to the Guinier model in the regions noted above (figure 7.13). A good fit was obtained, and the resulting R_g values were similar to those obtained from fitting the real data. From this analysis it is clear that the Guinier model is not appropriate for the craze structure and thus does not provide an adequate test of parameters obtained by Porod analysis.

7.3.2 Success of the Fourier Transform Technique

As described in section 3.5.2, The direct-indirect transform method is not as model dependent as either Guinier or Porod analysis techniques. In addition, it has been demonstrated that this technique works well even with a lack of low-q data,[78] thus addressing the weakness in Porod analysis due to its dependence on the calculation of the invariant. The drawback to this technique is its requirement for complicated nonlinear fitting, and the fact that the results obtained are often quite difficult to interpret.

To perform the direct-indirect transform analysis the program GNOM Version E4.2, written by D.I. Svergun, was used.[44] This program allows one to choose between several general structural models for analyzing the data. The model selected was that of a system of monodisperse rod-like particles, with the program output being related to the cross-section

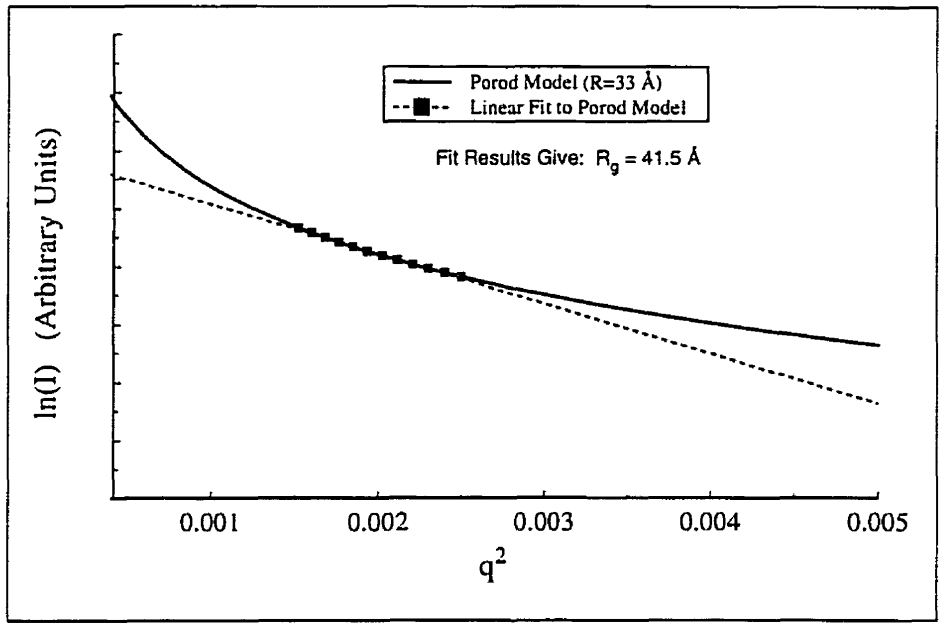

Figure 7.13: A fit of the Guinier model to ideal Porod model data

of the rods and the resulting pair distribution function obtained from the GNOM program, $P(r)$, being defined by:

$$P(r) = r\gamma_f(r) \tag{7.10}$$

where $\gamma_f(r)$ is the fibril correlation function described in equation 3.29.

In this analysis mode, the GNOM program follows the description of scattering from a randomly oriented system of rod-like particles, as given in the text by Glatter and Kratky,[41] which is shown to be the product of two terms:

$$I(q) \simeq I_l(q) \cdot I_f(q), \tag{7.11}$$

where $I_l(q) \propto q^{-1}$ is due to scattering from the long dimension averaged over all orientations relative to the incident x-ray beam. $I_f(q)$, the term of interest, is related to the cross-section of the rods. The experimental configuration used here implies near-complete orientation of rods perpendicular to the incident beam and isolation of the scattering perpendicular to the long axis. Therefore, the data is directly a measure of $I_c(q)$.

Since GNOM assumes the standard situation of equation 7.11, input data, $I(q)$ is automatically converted to a $qI(q)$ form. This is not appropriate for the data considered here, and input data is provided to GNOM as $I_f(q)/q$ so that it will correctly use the $I_f(q)$ data in its procedures.

The choice of the best $P(r)$ solution for the indirect transform of the scattering data is a complex issue. The GNOM program maximizes a parameter involving the weighted contributions from several different criteria.[44] These include a measure of χ^2, a measure of the smoothness of the solution, a test for the presence of systematic deviations between the solution and the data, and a test for stability of the solution with respect to the Lagrangian multiplier. Each criterion is assumed to follow a Gaussian distribution, $\mathcal{P}_c(i)$, described by:

$$\mathcal{P}_c(i) = e^{-\left[\frac{A(i)-B(i)}{\sigma(i)}\right]^2} \tag{7.12}$$

where $A(i)$ is the ideal value of the ith criteria, $B(i)$ is the actual value, and $\sigma(i)$ is a user-defined distribution width. An estimate of the goodness of a solution (a value between 0 and 1) is obtained from a weighted average of the $\mathcal{P}_c(i)$ values for each criterion, with user modifiable weights (w_i):

$$\frac{\sum \mathcal{P}_c(i)/w_i}{\sum 1/w_i} \tag{7.13}$$

with the sum being over all criteria.

Meaningful variation of these weights requires a priori knowledge of the structure. No useful information was available regarding the reweighting of any of the fit parameters, except that of oscillations in the $P(r)$ curve discussed below. Therefore, weights for these parameters were left at default values. These defaults values were checked by confirming that small changes in the values for any one parameter did not have a strong effect on the solution chosen.

As discussed in section 7.1.1, the structure of a craze consists of two quasi-independent lengthscales: that of the craze fibril diameter and that of the interfibril distance. A monomodal distribution is, therefore, not expected. To accommodate solutions with mul-

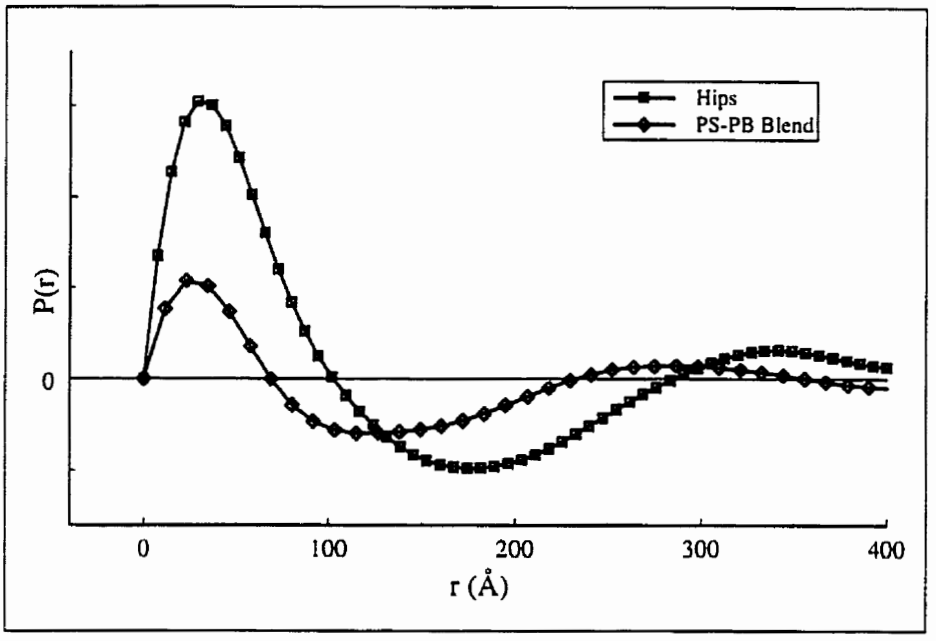

Figure 7.14: Pair correlation functions obtained from low-q range data of HIPS (□) and PS-PB blend (◇) samples at 65° C.

tiple peaks, the weight of the parameter measuring the smoothness of the solution was reduced by a factor of three.

To apply the method of indirect transform, an estimation of the maximum particle diameter D_{max} is required as input. In this case, the maximum diameter was set to 630 Å. This value was chosen because it corresponds to the minimum q value obtained ($D_{max} = \pi/q$). Larger and smaller values of D_{max} were tried giving almost identical results. A typical estimate of the goodness of the solution, determined for a representative HIPS sample, was given as 0.59 which the programs states to be a 'reasonable' solution.

The $P(r)$ solution obtained for HIPS and PS-PB blend samples in fig. 7.14 shows a primary maximum between 25 and 35 Å with a secondary maximum at about 350 Å in the HIPS, and at about 275 Å in the PS-PB blend. A region of negative $P(r)$, indicating void space, is observed in between the two peaks for both materials.

The primary purpose of using the GNOM program was to test the fit results for the *Power-Law* and *Sigmoidal-Gradient* models. The peak in $P(r)$ at low values of r is the

Typical Fibril Diameter Values (Å)			
Material	Guinier	GNOM	Porod
HIPS	115.8 ± 0.7	80 ± 2	84 ± 11
2 wt% PS-PB blend	103 ± 2	76 ± 3.5	73 ± 13

Table 7.3: Guinier and Fourier transform results compared to *Power-Law* model results from low-q range data for samples at 65° C.

one of interest because it corresponds to the fibril diameters measured by the Porod law fitting. To examine this peak more closely, the low-q data, which is attributed to inter-fibril scattering, was removed and only the high-q data were supplied to the GNOM program, along with a D_{max} of 100 Å. In this case, the $P(r)$ is expected to be monomodal and thus, the smoothness parameter was reset to its default value.

For representative samples of both materials at a range of temperatures, the solutions obtained for the truncated data had goodness-of-fit estimates greater than 0.9, which the program declares to be an excellent solution. A comparison of typical fibril diameter values obtained from GNOM and from the Porod analysis is given in table 7.3. It is clear that the values agree quite well when GNOM fitting is applied to the high-q regions of the data where interaction effects are negligible.

In this chapter scattering lengthscales relevant to craze fibril structure have been identified, the scattering due to interfibril interactions has been examined, and structural models of the craze fibrils have been identified which provide a good description of the scattering data observed. In chapter 8 the information obtained here will be interpreted in the context of current theories of craze formation and growth.

Chapter 8

Discussion

SAXS experiments were performed on two bulk polymer materials to study the craze deformation process in these materials. Included in this study is an identification of the macroscopic deformation modes occurring in the materials, an examination of the overall craze structure, a measure of the craze fibril diameter, an investigation of the fibril conformation, and a probe of craze growth mechanisms.

Deformation mode parameters, obtained in section 6.5, will be used to identify distinct stages in the deformation process. Analysis of the SAXS data, done in section 7.1, will be used to obtain an indication of the overall craze structure. Porod model fitting applied to the data (section 7.2) will provide more detailed information regarding craze fibril diameters and structure. Finally, observations of the temperature dependencies of the craze fibril diameter and applied stress will be used to provide indications of craze growth mechanisms.

8.1 Macroscopic Deformation

The identification of the macroscopic deformation modes relies on the determination of the applied stress, scattering invariant and reduced thickness-weighted density. These parameters provide information regarding the energy absorbed by the sample, the presence of dilatational strain, and changes to the sample thickness and density, respectively. A comparison of these parameters allows for the identification of the onset of craze formation and

the craze growth regions of the scattering curve, as discussed in section 6.5.

In the HIPS material, the deformation process begins with a linear stress-strain response (figure 6.5), a very gradual decrease in the $\widehat{\rho z}$ parameter, and no detectable change in the invariant. This can be interpreted as either elastic or shear deformation. As the deformation proceeds, a change in the slope of the stress-strain curve is observed, accompanied by changes in the invariant and a more rapid decrease in the $\widehat{\rho z}$ parameter. This stage is best described by a mix of deformation modes including cavitation, craze formation, and shear. At later stages in the deformation, the stress reaches a maximum and levels off. In addition, the rate of change in both $\widehat{\rho z}$ and the invariant increases; both are observed to be linear with strain at this stage. The approach to a constant stress is considered[14,66] to be an indication of deformation by craze growth, confirmed by the linear change in $\widehat{\rho z}$ with strain.

In the PS-PB blend, the deformation process also begins with a linear stress-strain response and a very gradual decrease in the $\widehat{\rho z}$ parameter. However, craze formation, as indicated by increases in the invariant, is observed to begin at an earlier stage than in HIPS. Either elastic or shear deformation or both, therefore, occurs during the initial stages with a smooth transition to a multiple mode deformation process involving craze formation and growth. The rapid drop in applied stress observed at large strain is characteristic of brittle failure of the material. The lack of a region of constant applied stress, combined with linear variations in $\widehat{\rho z}$, indicates that a region of pure craze growth does not occur.

It can be seen that the two materials exhibit distinct deformation processes; while both materials undergo craze deformation, it is only the HIPS material which can be seen to reach a stage where the deformation process is dominated by the extension of craze fibrils. In the PS-PB blend, craze formation begins early on in the deformation process, although it never becomes the dominant deformation mechanism. The observation of 'elastic' behavior in the HIPS material extending to larger strain values than in the PS-PB blend is most readily attributed to the elasticity of the rubber particle additive. A more precise identification of the deformation modes will require further testing in which the full range of deformation

conditions are employed. The apparatus described in this thesis is capable of making these measurements.

The lack of a pure craze growth deformation mode does not preclude the extraction of craze structure parameters from both materials. However, analysis of craze mechanisms requires the assumption that applied stress acts primarily to produce craze extension.

The PS-PB blend has its yield point at higher stress values than in HIPS, but has almost no extension beyond this point. Both facts point to a poorer mobility of the polymer chains in this material, indicating that the liquid rubber additive is not as effective as the higher molecular weight additive in the HIPS material. The lack of a constant stress region suggests brittle failure. However, brittle failure is generally assumed to occur immediately following the elastic region,[15] while these tests indicate that some form of plastic deformation occurs. This indicates that current concepts of brittle failure are oversimplified. In addition, the level of observation provided in this work represents a much more detailed insight into the performance of these types of toughened thermoplastics than is found in the general literature.

In both materials stages are observed in the deformation process where a combination of several deformation mechanisms are at work simultaneously. The measurements of applied stress, $\widehat{\rho z}$, and invariant are not sufficient to isolate contributions from the different mechanisms. A measurement of the true strain would provide information on the actual deformation in the sample region under observation and would allow for reversibility tests of elastic strain. Absolute scattering intensity measurements would allow true volume measurements from $\widehat{\rho z}$ and the invariant, allowing for a measure of the dilatational contribution to the strain. With this information available, the full deformation history of a sample may be accounted for.

8.2 Interfibril Craze Structure

The interfibril craze structure provides valuable information regarding the way in which crazes form and grow.[3,21] Measurements of the craze structure were obtained from direct-

indirect transforms of the SAXS data, observations of peaks in the scattering data, and power-law exponents with their corresponding scattering regions. From this information it is possible to probe the extent of interfibril interactions.

8.2.1 $P(r)$ Indications of Interfibril Structure

The GNOM program, discussed in section 7.3.2, provides pair distribution functions of the structure, $P(r)$, which are difficult to interpret for complex geometrical structures. In general, the $P(r)$ curves obtained show single peaks below 50 Å, negative regions from 100–300 Å, and shallow peaks tailing off to zero at large r values. In terms of known structures, peaks at small r values correspond to the single particle structure of craze fibrils, negative regions correspond to voids between fibrils, and shallow positive regions may be considered to be due to interfibril interactions. The two test materials give similar $P(r)$ shapes for the temperatures considered, but the PS-PB blend material has all the above-mentioned features occurring at slightly smaller lengthscales than in HIPS. $P(r)$ for the PS-PB blend material reaches 0 by 400 Å, while $P(r)$ from HIPS is still positive at this point. Apparently HIPS displays craze fibril structures that are similar to those occurring in the PS-PB blend, but at slightly larger lengthscales. This implies a greater sensitivity to the low-q cutoff in the HIPS data than with the PS-PB blend. These observations suggest in turn that indications of long-range ordering in the power-law analysis (section 8.2.3) may be an artifact of the finite data range.

8.2.2 Interfibril Interaction

The peaks observed in the data may either be attributed to short-range order peaks or to single-particle scattering from uniform objects, as mentioned in section 3.5.1. Using a Bragg law approximation, the primary peak observed in PS-PB blend data (figure 7.1) corresponds well to the maximum at large r in its $P(r)$ curve, a good indication that it is indeed an ordering peak. Although the pair distribution function does not give a well-defined maximum at large r for the HIPS material, it seems reasonable to assume that

the peak shoulder observed in the HIPS material may be interpreted in a similar manner following the discussion of section 8.2.1. In the absence of well-defined higher order peaks and given the convergence to zero at large r of the $P(r)$ curves, it appears that no long range fibril ordering exists.

8.2.3 Power Law Exponents

At low-q values, x-ray scattering from individual oriented rods or fibrils should be independent of q. In addition to the scattering from individual rods, there will also be scattering from the inter-rod distances. If there is no long range interaction between rods, this scattering will also become independent of q at sufficiently low-q. For the PS-PB blend material, a slope of 0 is commonly observed in the first region; this is not true for HIPS, suggesting that at distances corresponding to the lowest q values examined, there are still interactions between craze fibrils. This may be understood from the discussion of the $P(r)$ curves in section 8.2.1, where it was noted that the larger lengthscales in the HIPS crazes may result in the apparent of long-range order due to the low-q cutoff limits in the scattering data.

X-ray scattering from oriented rods with sharp interfaces will exhibit $I \propto q^{-3}$ anisotropic Porod law behavior. If there is sufficient loss of orientation, $1/q$ scattering from the long axis will become significant and the scattering pattern will follow the isotropic Porod scattering, $I \propto q^{-4}$. The orientation limits, at which the scattering from the rod cross-sections can be isolated from rod axial scattering may be calculated from a knowledge of the rod length and scattering range using equation A.3. The possibility that there is sufficient anisotropy in the craze fibrils to warrant the use of the standard $I \propto q^{-4}$ Porod model should be considered. In such a case, the scattering in the third region would be attributed to Porod law scattering, and the second region would be considered a transition region with the $1/q^3$ scattering describing surface fractal geometry in the craze structure. Such structures are not consistent with TEM observations of crazes and the arguments for an anisotropic interpretation cannot, therefore, be justified.

It must also be considered that the level of orientation causes the scattering to be in an

intermediate state between the oriented $I \propto q^{-3}$ and the random $I \propto q^{-4}$ states, resulting in the observed non-integer power-law exponents measured. From numerical simulations it can be shown that in this intermediate state the resulting scattering will not be linear on a log-log scale, which is in contrast to the clear linear regions observed in figure 7.3. This is also supported by the agreement between the fibril diameters calculated from the Fourier transform and modified Porod's law fitting.

If the interfaces are diffuse with a power-law density gradient, the Porod Law scattering for oriented rods will be:

$$I(q) \propto q^{-\alpha} \qquad [3 < \alpha \leq 5] \tag{8.1}$$

The exponents obtained in the middle region for the PS-PB blend samples were often within error of 3, implying predominately sharp boundaries. For the HIPS material, the exponent values were consistent with equation 8.1 and less than 4 in the second region, suggesting diffuse boundaries. The significance of the craze fibril structure will be discussed in more detail in section 8.3.

The middle q-region of the data was observed to occur between $q = 0.02$ and $q = 0.05$ Å for both materials, corresponding to lengthscales between 125 Å and 300 Å. This reflects interfibril lengthscales in the craze structure, and thus, the scattering may be interpreted as coming from the voids in the craze material.

The data in the third region and beyond, for both materials and all temperatures, decreases more rapidly than the expected $I \propto q^{-3}$. It is possible to fit this data to the same diffuse boundary models applied to the second region, implying that there are two different fibril structures at different length scales. This is not a particularly satisfactory explanation, as craze theory does not predict this and there have been no observations of multiple fibril structures reported in the literature.

A more satisfactory explanation of the general scattering in the third region is that the polymer chains, composing the craze fibrils, are rearranging themselves along the axis of the craze fibrils. This type of ordering would result in significant changes to the polymer scattering, causing the background subtraction to be incorrect in this region. Models of

polymer scattering in bulk materials is a complex issue,[45] and models of orientation processes in polymers linked to the formation of craze fibrils have not been reported in the literature.

To sum up the discussion of section 8.2, the craze structure consists of a forest of well aligned craze fibrils with weak interfibril interaction. Both the results from the GNOM program and the observed scattering peaks indicate that there are preferred distances between the craze fibrils. The lack of a series of well-defined peaks at regular intervals implies that the interfibril interaction does not go much beyond nearest neighbours.

Polymer chains within craze fibrils appear to undergo orientation processes. No details of this orientation can be determined at this time. A model of SAXS scattering which can account for both the interaction of craze fibrils and polymer conformation within fibrils would be a great asset for examining the contribution of polymer chain orientation to the deformation process.

8.3 Fibril Structure

The measure of the craze fibril diameters is key to the principal theory of craze growth,[13,28] where the craze fibril diameter is identified as an indicator of local stresses within a craze and therefore may be used to determine the energy required for craze growth. (See section 2.3.2 and 2.3.3 for more details.) It is assumed that the craze fibril boundaries are well-defined; an assumption which has been shown to be inaccurate in this work. It is therefore important to examine the nature of the fibril boundaries and consider possible effects of non-ideality on the theory.

Several different approaches are used to examine the fibril structure within the crazes. Two models of diffuse fibril boundaries, reflecting different boundary structures, were applied to determine the fibril diameter and identify a possible boundary structure. In addition, the GNOM program was used to examine the fibril scattering region in order to obtain alternative measurements of fibril diameter for comparison with those obtained from the models.

The commonly used *Constant Background* model, which assumes that there is uniform internal structure within the craze fibrils, has been shown to be inaccurate in a Porod analysis. An examination of the effect on fibril diameter measurements through incorrect application of this model is also presented here along with a comparison of the fibril diameters reported in the literature.

8.3.1 Diffuse Boundary Models

The HIPS material is believed to initiate crazing through cavitation at phase boundaries.[18,21,32] The *Sigmoidal-Gradient* model was developed to describe boundaries in two phase polymer systems,[46,75] and thus, may be consistent with the crazing mechanism of the HIPS material. The *Power-Law* model is based on assumptions of non-Newtonian plastic flow (equation 2.11) which point to a power-law strain-rate gradient between the center of the craze fibrils and the midpoint between fibrils. This strain-rate gradient will result in a density gradient while the material remains under tension. The PS-PB blend material is expected to form crazes through plasticization and plastic flow which follows non-Newtonian fluid flow, thus the *Power-Law* model is expected to hold.

From tests of the two models, it has been shown that the *Sigmoidal-Gradient* model provides a better description of the data than the *Power-Law* model for both materials. This indicates that the mechanism controlling the formation of craze fibrils is similar in both materials. Although the *Sigmoidal-Gradient* model does not have an established theoretical link to phase boundaries, it has been observed to hold well for two-phase thermoplastic materials.[46,55,75] Clearly the void-fibril interface can be thought of in terms of a two phase system, giving credence to the use of the *Sigmoidal-Gradient* model in this case. The fact that it holds better than the *Power-Law* model demonstrates that power-law strain gradients, implied in the *Meniscus Instability* model (section 2.3.2), have little effect on the density distribution within the fibrils.

The difference in the observed β and σ_s parameters for HIPS and the PS-PB blend material indicate that the fibril boundaries in the PS-PB blend material are sharper than

in the HIPS material. A comparison of the σ_s parameter to its corresponding mean fibril radius, however, reveals that the value of σ_s is about half the fibril radius. This indicates that variations in the density are not limited to a small region at the fibril surface; rather, the density varies throughout the fibril. This is quite significant for measurements of the fibril surface energy, described in section 2.3.3 and discussed in section 8.4; a large variation in the density within a fibril implies that the surface energy required to form the fibril is not well-defined.

8.3.2 Comparison to Constant Background Model Results

A sample of fibril diameter values obtained from the literature is given in table 8.1. The accuracy of the values given is not specifically stated. However, from the precision to which the numbers are quoted, it can be inferred that the variation in the diameters for similar materials at room temperature is significantly greater than the implied experimental uncertainty (accuracies of ± 10 Å are obtained in the present work). The large variation among these values is not well-understood. It is unlikely that the lack of invariant corrections at low-q can account for the diversity among the values reported by the same group because the low-q limit would be expected to remain constant. In his 1991 paper, Bubeck[17] suggests that detector saturation is to blame for previously observed lower values, however, no details are given to support this. It is possible that the variations in the results are due to the effects of polymer orientation at extremely high-q values. It is also possible that the variation is due to a misapplication of the *Constant Background* model.

To understand the effects of an incorrect application of background values, numerical tests were done by generating ideal data based on the diffuse boundary *Power-Law* model, described in appendix C:

$$I_f(q) = \frac{4}{\pi(1-v_f)} \left(\frac{(1-\beta)\pi}{2\Gamma(\beta)\cos(\beta\pi/2)} \right)^2 R^{-3+2\beta} q^{-5+2\beta} \tag{8.2}$$

Authors	Year	Material	Fibril Diameter
Brown et al.[2]	1981	PS	60 Å
Brown et al.[64]	1984	PS	120 Å
Bubeck et al.[57]	1986	HIPS	90–104 Å
Brown et al.[24]	1987	PS	65 Å
Bubeck et al.[23]	1987	HIPS	87 Å
Brown et al.[29]	1989	PS PB blend	87 Å
Bubeck et al.[17]	1991	HIPS	140 Å
Current Results		PS PB blend	73 ± 10 Å
Current Results		HIPS	84 ± 10 Å

Table 8.1: Fibril diameter values at room temperature obtained from the literature

with

$$\begin{aligned} R &= 30\ \text{Å} \\ v_f &= .25 \\ 0 < \beta &\leq 1 \\ .01\ \text{Å}^{-1} \leq q &\leq .11\ \text{Å}^{-1} \end{aligned} \tag{8.3}$$

The values chosen for R (the fibril radius), v_f (volume fraction of fibrils), β (*Power-Law* model boundary parameter), and q are based on typical values observed in the data. The chosen values of $\bar{R}_f$ and v_f result in a fibril diameter ($\bar{D}_f$) of 80 Å.

This ideal data was then fit to the *Constant Background* model: A plot of Iq^3 vs. q^3 is extrapolated linearly from the highest-q values and the low-q intercept is obtained. From this intercept value, diameters were extracted using the relation:

$$\bar{D}_f = \frac{4}{\pi(1 - v_f)K}, \tag{8.4}$$

where K is the intercept determined from the extrapolation.

The results of these tests, shown in fig 8.1, demonstrate that a non-integer power-law relation will appear as a good fit within the *Constant Background* model.

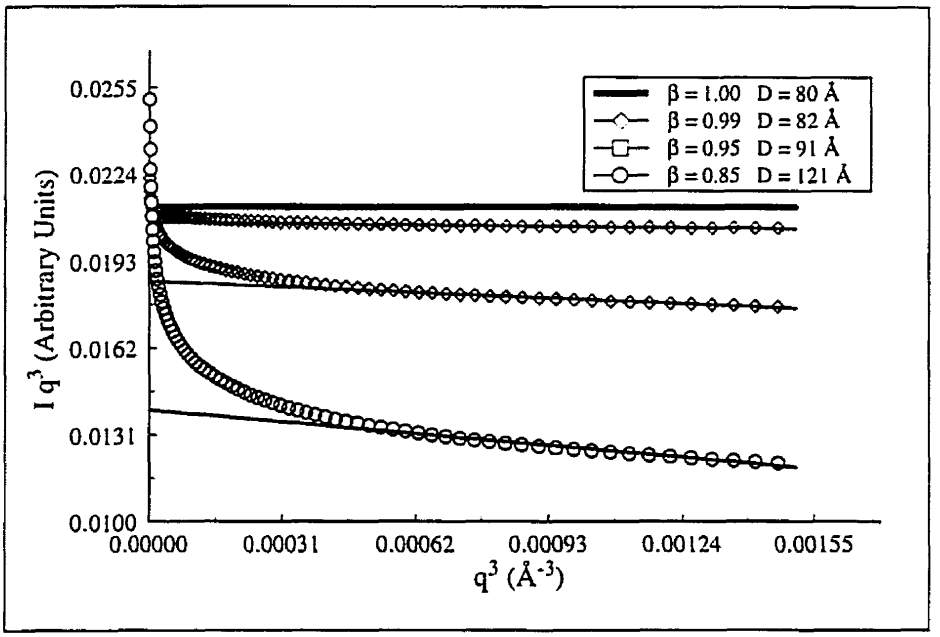

Figure 8.1: *Constant Background* model fit to ideal *Power-Law* model data

8.3.3 Detector Artifacts

Experimental sources of variations in measured fibril diameters must also be considered. As mentioned in section 6.1, the fibril diameters were obtained in a time series of measurements over a range of temperatures. Definite trends are observed in the fibril diameters with temperature for the HIPS material (figure 8.2), as predicted by the *Meniscus Instability* theory of craze growth. Two datasets are considered with significantly different electron beam current. The initially high beam current dataset is indicated on figure 8.2 by an 'X' with the highest temperature data corresponding to the beam current for that run. A distinct offset in trend between datasets can be seen. This discrepancy can be linked to a significant difference in both the electron beam current of the synchrotron and the measured detector live-time.

The most likely explanation for the presence of this offset is the occurrence of non-linearity in the detector response due to the presence of a field-masking ion cloud in the detector gas.[79] Such a situation would occur when there is a partial saturation of the

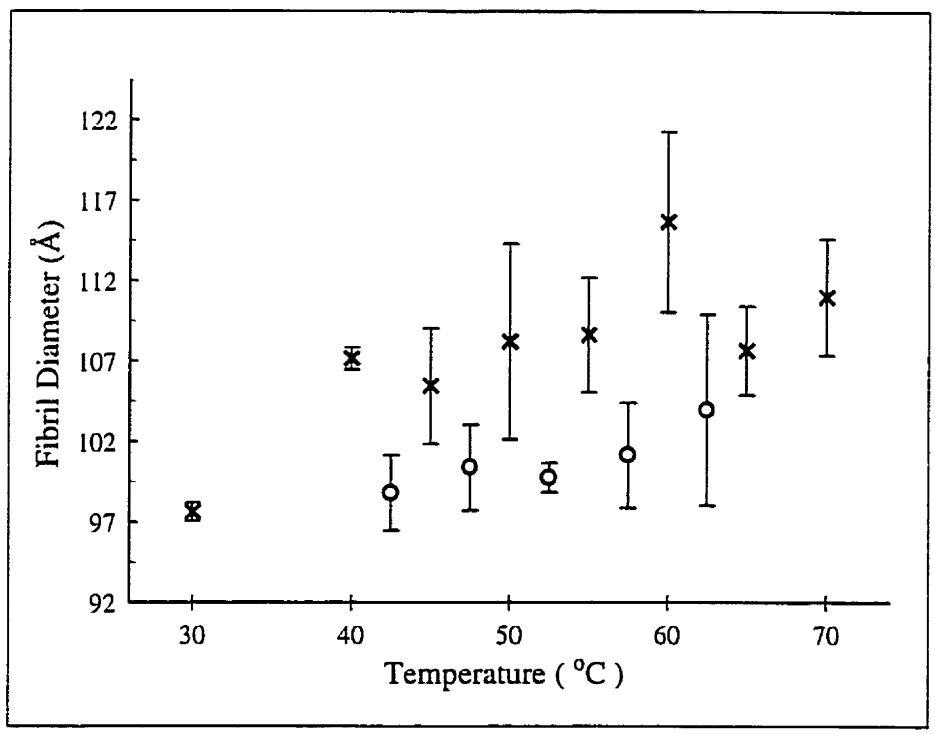

Figure 8.2: Craze fibril diameters obtained from the *Sigmoidal-Gradient* fit parameters as a function of temperature for the HIPS material over two datasets. Note that the two highest temperature data points from the first dataset, marked with an 'X', correspond to measurements taken at the end of a run.

detector from a high x-ray beam current. Detector saturation effects, such as those suggested to be present here, have been reported previously at other facilities.[80]

It is worth noting that when similar tests were done using the *Power-Law* model, the discrepancy noted in figure 8.2 was not visible. However, the scatter in the data due to inaccuracies in the model fitting were sufficiently large to obscure such an aberration if it did exist. Clearly the greater precision available with the *Sigmoidal-Gradient* model provides the capability to identify such a detector problem.

In conclusion to this discussion of fibril structure, the craze fibrils have been shown to follow a *Sigmoidal-Gradient* diffuse boundary model. This suggests that the power-law stress gradients expected from the *Meniscus Instability* model of craze formation and growth do not influence the density distribution within the craze fibrils. The extent of the density gradients within the fibrils indicates that any theory of craze fibril formation must take this factor into account.

The standard technique for obtaining surface energy values describing craze growth involves the use of the *Constant Background* model to obtain fibril diameters. From the numerical tests presented here, it is clear that this model can produce inaccurate results. A test for linearity in the plot is insufficient. Care must therefore be taken in selecting the appropriate model to use for determining fibril diameters.

The precision of the fibril diameter measurements from the *Sigmoidal-Gradient* model brings to light possible problems with the detector system. A correlation of the observed offset in fibril diameters of HIPS with the environment variables of electron beam current and detector live-time indicate that the detector may not be operating linearly throughout the accessible scattering angle range. This effect is subtle and indicates the need to thoroughly characterize the detector being used for this type of measurement to a greater degree than has previously been thought acceptable.

8.4 Microscopic Mechanisms of Crazing

As described in sections 2.3.2 and 2.3.3, the growth of crazes, which occurs through the drawing of new fibrous material out of the active zone at the craze boundaries, is governed by two competing mechanisms, chain scission and forced reptation. The probability for an individual chain to undergo scission is independent of temperature, while the probability for it to undergo forced reptation will increase with increasing temperature. From a knowledge of the probabilities of these two mechanisms, the energy required to lengthen a craze fibril by an incremental amount (an increase in the fibril surface), Γ_f, may be determined.[37] It can be deduced from the temperature dependencies of scission and reptation that at sufficiently low temperatures, where scission dominates, the surface energy will be independent of temperature. Above some critical point, reptation will begin to dominate the craze growth process and the surface energy will decrease with temperature. For pure PS, this critical temperature has been determined to be approximately 70° C.[6]

The *Meniscus Instability* theory of craze growth indicates that the fibril surface energy, Γ_f, is proportional to the macroscopic parameters of applied stress and fibril diameter (equation 2.16). The fibril diameter is predicted to increase with temperature and the applied stress is expected to decrease with temperature during constant strain rate tests. This results in competing trends of similar magnitudes affecting the surface energy which should cancel out at sufficiently low temperatures.[1,3] By comparing the trends observed in the surface energy with those predicted from the microscopic theory of polymer motion, it is possible to test equation 2.16 and the *Meniscus Instability* model of craze growth.

The surface energy derived from equation 2.16, assumes that all applied stress goes into the formation of new craze fibril surface. For this reason, the equation is only valid where the deformation is proceeding by pure craze growth. From section 8.1, it has been noted that this deformation mode is only observed in the HIPS material and thus, only fibril diameters and stress values from the HIPS data are used here.

As noted previously (figure 8.2), the fibril diameters are observed to increase with increasing temperature, consistent with predictions of the *Meniscus Instability* model. A close

examination of the trend in the fibril diameters indicates a possible transition from fibril formation via chain scission to that of formation via reptation at 55° C. The prediction of the *Meniscus Instability* model of decreasing applied stress with increasing temperature, shown in figure 8.3, can also be seen to hold.

Surface energy values, determined from a product of applied stress and fibril diameter (equation 2.16 with $\xi = 1$), are shown in figure 8.3. From a microscopic viewpoint, the surface energy is expected to be to be constant with temperature at low temperatures (scission) and decrease with temperature at high temperatures (reptation). The fibril diameter data suggests that such a transition occurs at approximately 55° C. It is not possible from this data to identify a transition point between regions of chain scission dominated and reptation dominated deformation. In particular, the estimated transition point from the fibril diameter data cannot be confirmed by the surface energy trends. The change in the surface energy is also suspiciously similar to that observed for the applied stress and thus the fibril diameter changes are not having as big an effect as suggested by the theoretical background.[1]

The equation for surface energy, developed as part of the *Meniscus Instability* model, does not take into account the diffuse boundaries of the craze fibrils which have been shown to exist. However, the observed Gaussian density distribution suggests the possibility that a mean surface energy might be defined which can account for the fuzzy boundaries. Power-law density gradients, suggested by the non-Newtonian fluid mechanics of the *Meniscus Instability* model, are not observed. Although power-law density gradients are not explicitly predicted in the *Meniscus Instability* model, the non-Newtonian fluid flow suggests that such gradients might be present during dynamical processes. The energy required for fibril orientation as well as the presence of surface stresses are not accounted for in this model. These observations thus bring into question the completeness of the model and the usefulness of the surface energy in accurately describing the mechanisms of craze fibril growth.

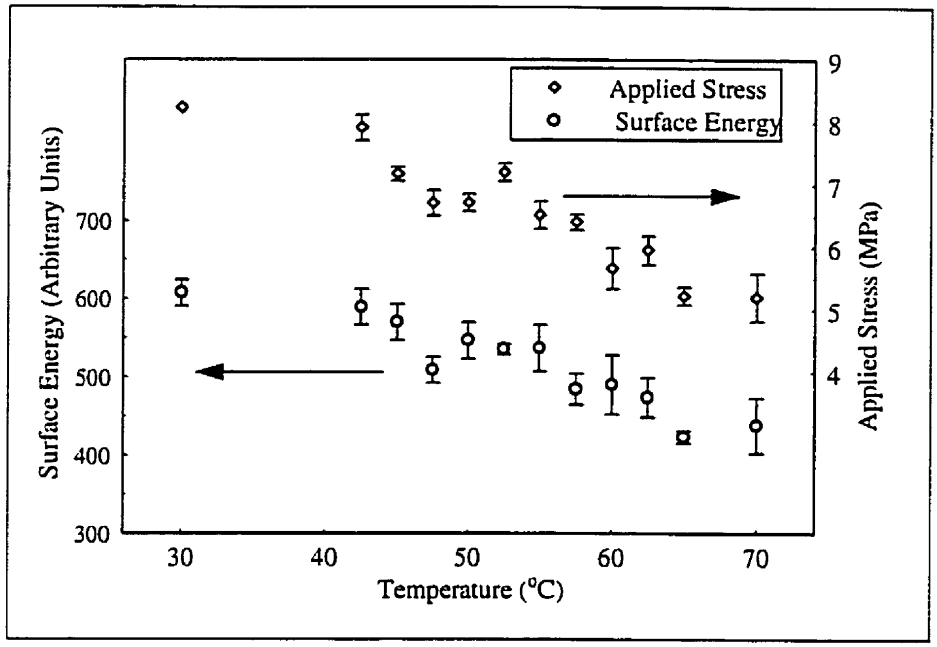

Figure 8.3: Weighted average of applied stress and surface energy as a function of temperature for the HIPS material, showing the similarity in trend for the two curves.

Chapter 9

Conclusion

An apparatus for real-time x-ray scattering measurements of crazes in bulk polymer materials has been designed and tested. The new design features overcome many of the shortfalls of previously reported techniques discussed in section 4.2. In particular, this apparatus is capable of symmetric tensile deformation which maintains the sample center in the x-ray beam (described in chapter 5). Slotted sample holders allow for stress relaxation in samples without imposing compression stress which obscures observation of the relaxation process. An Entran load cell is mounted in the system to provide direct measurements of the stress applied to the sample. A motor control system capable of variable strain rates is linked to the load cell to enable constant stress tests in addition to constant strain and constant strain rate experiments. The variety of testing methods allows the mechanical properties of polymers to be investigated with a focus on the differentiation of these properties. Progress has been made on developing a method of measuring the true polymer strain using laser diffraction from a reflective grid fixed to the sample. In addition, the radiative heating technique developed provides an accurate method for temperature-dependent investigations, valuable for probing the underlying mechanisms involved in polymer deformation. Finally, the entire deformation apparatus is contained in a portable sample chamber which can be readily adapted to different x-ray synchrotron and in-house sources.

The equipment was used to perform a constant strain rate investigation of two dif-

ferent polymer materials, HIPS and a novel PS-PB blend, at temperatures ranging from 30 to 70° C. Changes with strain in the applied stress, x-ray absorption by the sample, and effective scattering volume were used to obtain information regarding the macroscopic deformation process and identify the presence of craze formation and craze growth stages.

Both materials were observed to undergo craze deformation. A pure craze growth stage was observed in the HIPS deformation process, but not in the PS-PB blend. It was also noted that the yield point in the PS-PB blend occurs at higher stress values, followed by rapid failure. This indicates that the HIPS material has significantly higher polymer chain mobility than the PS-PB blend material, an unexpected observation given early reports on the performance of the novel material.

It was not possible to distinguish between elastic and shear deformation occurring in the deformation stage characterized by a linear stress-strain relationship. Neither elastic nor shear deformation results in changes to the x-ray scattering pattern in the angular range observed. In addition, it is not possible to directly link specific deformation modes with changes to the polymer conformation at monomer lengthscales. Free relaxation tests — which the current apparatus is capable of — combined with measurements of the true strain — possible using the laser diffraction technique currently under development — are required to identify these deformation modes.

The interpretation of SAXS data is highly model-dependent and so it is important to examine carefully the models used to confirm their applicability before extracting crucial information such as the fibril diameter. SAXS measurements from the constant strain rate investigation were used to examine the craze fibril structures. Ordering peaks were observed in the data, consistent with a regular interfibril distance predicted by the *Meniscus Instability* model. The *Constant Background* model was found to be inappropriate for the scattering data observed and it was shown that incorrect application of this model to data similar to that examined here could account for the variation in fibril diameters reported in the literature.

It was determined that the craze fibrils were best described by a diffuse boundary struc-

ture following the *Sigmoidal-Gradient* model. Fibril diameters obtained from diffuse boundary models agreed with those obtained from a direct-indirect transform of the scattering data. The preference of the *Sigmoidal-Gradient* model over the *Power-Law* model indicated that non-linear stress gradients predicted by the *Meniscus Instability* model do not have a significant effect on the structure of the fibrils and must be confined to the regions near the craze surface.

The *Sigmoidal Gradient* model has historically been associated with phase boundaries in polymer materials. Such surfaces could be expected from the HIPS materials if fibrils are formed from voids created by the separation of the rubber-particle additive from the PS matrix. The success of the *Sigmoidal Gradient* model for the PS-PB blend material cannot be accounted for in this way. Here the additive is in a liquid form and is expected to act as a plasticizer rather than as a void promoting defect. These observations indicate a shortfall in the *Meniscus Instability* model which does not allow for a Gaussian-type density distribution within the craze fibrils.

Craze fibril diameters were observed to increase and applied stress to decrease with increasing temperature, as predicted by the *Meniscus Instability* model. It was not possible to identify a transition between scission dominated and reptation dominated crazing regimes. This may be due to the insufficiency of the data, the inadequacy of the surface energy parameter, or a failure of the forced reptation model.

The surface energy is expected to provide a link between macroscopic parameters and microscopic chain dynamics. The use of surface energy is called into question by the observations reported here that the craze fibrils contain diffuse boundaries. The *Meniscus Instability* model must be reexamined in light of the evidence presented here to provide a parameter which can effectively link macroscopic measurements with theories of polymer chain dynamics. In addition, a more thorough temperature dependent test of the fibril diameters is in order, to obtain a precise determination of the scission to reptation transition.

The *Meniscus Instability* model also lacks an accounting of the orientation process among the polymer chains. A correction similar to the entropy term of the *coil-strand-*

transition model may be in order. Before such a correction can be accurately made detailed information on the orientation process is required. Models of scattering which can account for the polymer chain orientation within the framework of a craze fibril structure are desired so that the necessary information on this orientation processes may be used in the models of craze growth.

Possible sources of detector error must be investigated and scattering measurements must be taken with very high live-times (> 90%). The temperature trends in the fibril diameters do not appear to be obscured by the detector effects so this is not a critical problem for the measurements.

In conclusion, a state-of-the-art apparatus for RTSAXS measurements of craze growth has been produced. This apparatus is capable of detailed investigations of all standard deformation modes with variable temperature. Two sample materials, HIPS and a solvent-toughened polystyrene have been examined at temperatures between 30 °C and 70 °C. The SAXS data from the craze fibrils was analyzed using several techniques including tests for power-law scattering exponents and a comparison of modified Porod's law models. The model comparison indicates a density gradient within the fibrils, which questions traditional SAXS measurements of these fibrils and the use of the surface energy parameter. Surface energy results have been examined in light of the molecular-level predictions of polymer chain dynamics. However, the present results are inconclusive in identifying a scission-to-reptation transition.

A precise interpretation of the scattering from craze fibrils has thus been developed, allowing detailed information of the craze structure to be extracted. These analysis tools, combined with the extensive capabilities of the apparatus, provide a complete suite of measurement probes allowing access to an unprecedented degree of information at both the macroscopic and microscopic levels. The potential to obtain such information provides a means to perform detailed tests of structure-property relationships along with a method for examining the theory of forced reptation. To further this work, more data is required to provide a precise measure of the surface energy as a function of temperature. An alternative

parameter must be considered to the surface energy. And finally, more comprehensive models of the craze structure need to be developed and tested.

Bibliography

[1] E. Paredes and E. Fischer, Makromol. Chem. **180**, 2707 (1979).

[2] H. Brown and E. Kramer, Journal of Macromolecular Science — Physics **B19**, 487 (1981).

[3] E. Kramer, in *Advances in Polymer Science*, edited by H. Kausch (Springer-Verlag, Berlin, 1983), Vol. 52/53 Crazing in Polymers, Chap. 1.

[4] H. Brown, P. Mills, and E. Kramer, Journal of Polymer Science: Polymer Physics Edition **23**, 1857 (1985).

[5] O. Gebizlioglu *et al.*, Macromolecules **23**, 3968 (1990).

[6] C. Plummer and A. Donald, Macromolecules **23**, 3929 (1990).

[7] G. Salomons *et al.*, Review of Scientific Instruments **67**, 1748 (1996).

[8] A. Hristov, A. Yee, L. Xie, and D. Gidley, Polymer **35**, 4287 (1994).

[9] A. Magalhães and R. Borggreve, Macromolecules **28**, 5841 (1995).

[10] D. Svergun, Journal of Applied Crystallography **25**, 495 (1992).

[11] D. Svergun, Journal of Applied Crystallography **26**, 258 (1993).

[12] L. Feigin and D. Svergun, *Structural Analysis by Small-Angle X-ray and Neutron Scattering* (Plenum Press, New York, 1987).

[13] E. Kramer and L. Berger, in *Advances in Polymer Science*, edited by H. Kausch (Springer-Verlag, Berlin, 1990), Vol. 91/92 Crazing in Polymers, Chap. 1.

[14] A. Kinloch and R. Young, *Fracture Behavior of Polymers* (Elsevier Applied Science, New York, 1993).

[15] L. Sperling, *Introduction to Physical Polymer Science*, 2nd ed. (John Wiley and Sons, Toronto, 1992).

[16] Y. Sha, C. Hui, A. Ruina, and E. Kramer, Macromolecules **28**, 2450 (1995).

[17] R. Bubeck, D. Buckley Jr., E. Kramer, and H. Brown, Journal of Materials Science **26**, 6249 (1991).

[18] D. Dompas and G. Groeninckx, Polymer **35**, 4743 (1994).

[19] C. Plummer and A. Donald, Polymer **32**, 409 (1991).

[20] L. Könczöl, W. Döll, and G. Michler, Colloid & Polymer Science **270**, 972 (1992).

[21] A. Argon, R. Cohen, O. Gebizlioglu, and C. Schwier, in *Advances in Polymer Science*, edited by H. Kausch (Springer-Verlag, Berlin, 1983), Vol. 52/53 Crazing in Polymers, Chap. 6.

[22] S. Zhurkov, V. Kuksenko, and A. Slutsker, in *2nd International Conference on Fracture* (Chapman and Hall, London, 1969), pp. 531–544.

[23] R. Bubeck *et al.*, in *Materials Research Society Symposium Proceedings* (Materials Research Society, Pittsburgh, 1987), Vol. 79, pp. 293–298.

[24] H. Brown, E. Kramer, and R. Bubeck, in *Materials Research Society Symposium Proceedings* (Materials Research Society, Pittsburgh, 1987), Vol. 79, pp. 277–285.

[25] Y. Ijichi *et al.*, Macromolecules **26**, 829 (1993).

[26] P.-G. de Gennes, *Scaling Concepts in Polymer Physics* (Cornell University Press, Ithaca NY, 1979).

[27] A. Bhatia and R. Singh, *Mechanics of Deformable Media, Graduate Student Series in Physics* (IOP Publishing, Bristol England, 1986).

[28] R. Fields and M. Ashby, Philosophical Magazine **33**, 33 (1976).

[29] H. Brown *et al.*, Macromolecules **22**, 1002 (1989).

[30] O. Gebizlioglu, A. Argon, and R. Cohen, Polymer **26**, 519 (1985).

[31] A. Takaki, T. Hasegawa, and M. Isogawa, Polymer Engineering and Science **34**, 680 (1994).

[32] A. Argon and R. Cohen, in *Advances in Polymer Science*, edited by H. Kausch (Springer-Verlag, Berlin, 1990), Vol. 91/92 Crazing in Polymers, Chap. 7.

[33] Z. Xiao and K.D.Pae, Polymer Engineering and Science **33**, 1189 (1993).

[34] P. Beahan, M. Bevis, and D. Hull, Proceedings of the Royal Society of London A. **343**, 525 (1975).

[35] L. Berger and B. Sauer, Macromolecules **24**, 2096 (1991).

[36] L. Berger and E. Kramer, Macromolecules **20**, 1980 (1987).

[37] T. McLeish, C. Plummer, and A. Donald, Polymer **30**, 1651 (1989).

[38] B. D. Cullity, *Elements of X-Ray Diffraction* (Addison-Wesley, Reading MS, 1959).

[39] G. Margaritondo, *Introduction to Synchrotron Radiation* (Oxford University Press, New York, 1988).

[40] J. Jackson, *Classical Electrodynamics*, 2nd ed. (John Wiley and Sons, Toronto, 1975).

[41] O. Glatter and O. Kratky, *Small Angle X-ray Scattering* (Academic Press, London, 1992).

[42] H. Klug and L. Alexander, *X-ray Diffraction Procedures*, 2nd ed. (John Wiley and Sons, Toronto, 1974).

[43] O. Glatter, Journal of Applied Crystallography **10**, 415 (1977).

[44] D. Svergun and A. Semenyuk, *Manual of Program Package GNOM*, e4.2 ed., 1993.

[45] G. Beaucage, Journal of Applied Crystallography **28**, 717 (1995).

[46] W. Ruland, Journal of Applied Crystallography **4**, 70 (1971).

[47] C. Vonk, Journal of Applied Crystallography **6**, 81 (1973).

[48] W. Wiegand and W. Ruland, Progress in Colloid & Polymer Science **66**, 355 (1979).

[49] J. Rathje and W. Ruland, Colloid & Polymer Science **254**, 358 (1976).

[50] P. Pfeifer and M. Obert, in *The Fractal Approach to Heterogeneous Chemistry*, edited by D. Avnir (John Wiley & Sons, Toronto, 1989), Chap. 1.2.

[51] P. Schmidt, in *The Fractal Approach to Heterogeneous Chemistry*, edited by D. Avnir (John Wiley & Sons, Toronto, 1989), Chap. 2.2.

[52] P. Schmidt, Journal of Applied Crystallography **15**, 567 (1982).

[53] P. Schmidt, Journal of Applied Crystallography **24**, 414 (1991).

[54] J. Martin and A. Hurd, Journal of Applied Crystallography **20**, 61 (1987).

[55] J. Koberstein, B. Morra, and R. Stein, Journal of Applied Crystallography **13**, 34 (1980).

[56] P. Schmidt *et al.*, Journal of Chemical Physics **94**, 1474 (1991).

[57] R. Bubeck *et al.*, Polymer Communications **27**, 357 (1986).

[58] H. Kausch and C. Plummer, Polymer **35**, 3848 (1994).

[59] A. Gent and A. Thomas, Journal of Polymer Science **10**, 571 (1972).

[60] T. Krupenkin and P. Taylor, Physica Scripta **28**, 5819 (1995).

[61] S. Kreitmeier *et al.*, Colloid Polymer Science **273**, 1008 (1995).

[62] J. Forrest, K. Dalnoki-Veress, J. Stevens, and J. Dutcher, Physical Review Letters **77**, 2002 (1996).

[63] D. Hall, J. Hooker, and J. Torkelson, Macromolecules **30**, 667 (1997).

[64] H. Brown, Y. Sindoni, E. Kramer, and P. Mills, Polymer Engineering and Science **24**, 825 (1984).

[65] P. Westbrook, J. Fellers, R. Hendricks, and J. Lin, Journal of Polymer Science Physics Edition **21**, 696 (1983).

[66] M. Dettenmaier, in *Advances in Polymer Science*, edited by H. Kausch (Springer-Verlag, Berlin, 1983), Vol. 52/53 Crazing in Polymers, Chap. 2.

[67] S. Saimoto, *Department of Materials and Metallurgical Engineering, Queen's University* private consultation.

[68] S. Gillen, *Technologist, Department of Physics, Queen's University* private consultation.

[69] C. Harkless, Ph.D. thesis, University of Florida, 1990.

[70] M. Capel, G. Smith, and B. Yu, Rev. Sci Instruments. **66**, 2295 (1995).

[71] M. Capel, Synchrotron Radiation News **6**, 22 (1993).

[72] W. Press, S. Teukolsky, W. Vetterling, and B. Flannery, *Numerical Recipes in C*, 2nd ed. (Cambridge University Press, Melbourne Australia, 1994).

[73] W. Cleveland and S. Devlin, Journal of the American Statistical Association **83**, 596 (1988).

[74] J. Smith, private consultation through Queen's University STATLAB, which provides statistical consulting to Queen's faculty, staff and graduate students including validity of statistical analysis in theses.

[75] P. Perrin and R. Prud'homme, Macromolecules **27**, 1852 (1994).

[76] B. Hartmann, in *Physical Properties of Polymers Handbook*, edited by J. Mark (American Institute of Physics, Woodbury, New York, 1996), Chap. 49.

[77] W. Cushman, Modern Plastics **72**, 75 (1995).

[78] T. Lin and C. Tsao, Journal of Applied Crystallography **29**, 170 (1996).

[79] S. Ito, M. Tosaki, and N. Maeda, Nuclear Instruments and Methods in Physics Research A **368**, 738 (1996).

[80] C. Barberato, beamline manager of SAXS beamline at Laboratòrio Nacional de Luz Sìncrotron (LNLS), Campinas, Brazil
private consultation.

[81] J. Rigden, J. Dore, and A. North, Studies in Surface Science and Catalysis **87**, 263 (1994).

[82] A. Guinier and G. Fournet, *Small-Angle Scattering of X-rays* (John Wiley and Sons, New York, 1955), translation by C. B. Walker.

[83] P. Smith, American Statistician **33**, 57 (1979).

[84] P. Lerman, Applied Statistics **29**, 77 (1980).

[85] D. Hinkley, Journal of the American Statistical Association **66**, 736 (1971).

[86] P. Bevington and D. Robinson, *Data Reduction and Error Analysis for the Physical Sciences*, 2nd ed. (McGraw-Hill, Inc, Toronto, 1992).

[87] D. Montgomery and E. Peck, *Introduction to Linear Regression Analysis*, 2nd ed. (John Wiley & Sons, Inc., Toronto, 1992).

Appendix A

General Scattering Equation for Oriented Rods

The derivation shown here closely follows the work of Porod,[41] Feigin and Svergun[12] and Brown et al.[2] With the primary difference being that Porod assumes randomly oriented rods and Brown et al. incorporate a slit smearing geometry directly into their derivation.

The structure factor, $F(\vec{q})$, for a rod-shaped particle can be divided into two parts ($\vec{r}_{\parallel}$ and $\vec{r}_{\perp}$). The first term accounts for scattering from the long axis of the rod and the second describes scattering in the radial direction.[2,12,41,81]

$$\begin{aligned} F(\vec{q}) = \quad (\Delta\rho) \quad & \underbrace{\int d\vec{r}_{\parallel} e^{-i\vec{q}\cdot\vec{r}_{\parallel}}}_{\text{Long Axis}} \quad \cdot \quad \underbrace{\iint d\vec{r}_{\perp} e^{-i\vec{q}\cdot\vec{r}_{\perp}}}_{\text{Radial Axis}} \\ = \quad (\Delta\rho)L & \frac{\sin\left(|\vec{q}|\frac{L}{2}\cos(\omega_{\parallel})\right)}{|\vec{q}|\frac{L}{2}\cos(\omega_{\parallel})} \cdot \iint dA\, e^{-iq_{\perp}r\cos(\omega_{\perp})} \end{aligned} \tag{A.1}$$

Here $(\Delta\rho)$ is the electron density contrast, L is the length of the rod, A is the cross-sectional area of the rod, $\omega_{\parallel}$ is the angle of the rod with respect to $\vec{q}$, $\omega_{\perp}$ is the angle between the projections of $\vec{r}$ and $\vec{q}$ in the plane of the rod, $r = |\vec{r}_{\perp}|$, and $q_{\perp}$ is the magnitude of $\vec{q}$ projected into the rod cross-sectional plane.

The scattering intensity may be approximated by taking the averages of the square for each factor separately, thus giving:

$$I(\vec{q}) \approx (\Delta\rho)^2 NL^2 \int \left[\frac{\sin\left(|\vec{q}|\frac{L}{2}\cos(\omega_\parallel)\right)}{|\vec{q}|\frac{L}{2}\cos(\omega_\parallel)}\right]^2 d(\cos(\omega_\parallel)) \cdot 2\pi A \int r dr\, \gamma_\perp(r) J_0(q_\perp r), \quad \text{(A.2)}$$

where N is the number of rods, A is the rod cross-sectional area, J_0 is the zero-order Bessel function, and $\gamma_\perp(r)$ is the correlation function describing the rod cross-section.

If $qL > 2\pi$ it is possible to approximate the integral in the first term as going from 0 to ∞ with no loss of accuracy. However, if there is a large degree of orientation among the rods, one needs to consider the angular range of orientation

$$I(\vec{q},\omega) \approx (\Delta\rho)^2 NL^2 \int_{\cos(\omega-\Delta\omega/2)}^{\cos(\omega+\Delta\omega/2)} \left[\frac{\sin\left(|\vec{q}|\frac{L}{2}\cos(\omega_\parallel)\right)}{|\vec{q}|\frac{L}{2}\cos\omega_\parallel}\right]^2 d(\cos(\omega_\parallel)) \cdot 2\pi A \int r dr\, \gamma_\perp(r) J_0(q_\perp r) \quad \text{(A.3)}$$

where ω is the azimuthal scattering angle with $\omega = 0$ being perpendicular to the rod axis and $\Delta\omega$ the angular range over which the rods are oriented. If ω is set to zero and $|\vec{q}|L\cos(\Delta\omega) \ll 2\pi$ then the following approximation can be made:

$$\left[\frac{\sin\left(|\vec{q}|\frac{L}{2}\cos(\omega_\parallel)\right)}{|\vec{q}|\frac{L}{2}\cos\omega_\parallel}\right]^2 \simeq 1 \quad \text{(A.4)}$$

and the scattering intensity perpendicular to the rod axis becomes

$$I_\perp(\vec{q}) \approx (\Delta\rho)^2 NL^2 \cos(\Delta\omega) 2\pi A \int r dr\, \gamma_\perp(r) J_0(q_\perp r). \quad \text{(A.5)}$$

In the case of a close-packed system of oriented rods, such as that of craze fibrils, the scattering intensity due to the rod cross-section will contain additional terms due to the inter-rod interactions. The general equation for the scattering intensity of craze fibrils then becomes:

$$I_f(q) = \tilde{I} \int r dr\, \gamma_f(r) J_0(qr) + \text{Interaction Terms} \quad \text{(A.6)}$$

Appendix B

Porod's Law for Oriented Rods

Porod's law for oriented cylinders may be obtained in two ways: through dimensional arguments from standard Porod's law and through a detailed derivation following that of the original Porod's law. The simpler dimensional arguments will be presented first, and this will be confirmed by the detailed derivation which will make clear the assumptions involved.

B.1 Dimensional Basis

The standard Porod's Law is given by:

$$\lim_{q\to\infty} \frac{I(q)}{Q} = \frac{S}{\pi \mathcal{V}} q^{-4}, \tag{B.1}$$

where I is the x-ray intensity, Q is the invariant, q is the scattering angle, S is the total surface area of the scatterers, and $\mathcal{V}$ is the total volume of the scatterers.

It has been shown[41] that scattering for randomly oriented long thin rods is proportional to $1/q$. Since this scattering will not be observed in oriented rods, Porod's law for this type of structure must take on the form:

$$I \propto q^{-3} \tag{B.2}$$

At the same time, for rod-like particles, $\mathcal{V}$ can be rewritten as

$$\mathcal{V} = AL = \pi \bar{R}_f^2 L \tag{B.3}$$

and S as:

$$S = 2\pi \bar{R}_f L; \tag{B.4}$$

where L is the length and $\bar{R}_f$ is the radius of the rods. This gives:

$$\lim_{q\to\infty} \frac{I_f(q)}{Q_f} = \frac{2}{\pi \bar{R}_f} q^{-3}, \tag{B.5}$$

which is Porod's law for oriented rods.

B.2 Detailed Derivation

As described in section 3.7 the equation for the scattering intensity from oriented rods (equation 3.29) is given by:

$$I_f(q) = 2\pi \overline{(\Delta\rho)^2} AL^2 \int_0^\infty r dr\, \gamma_f(r) J_0(qr) = Q_f \int_0^\infty r dr\, \gamma_f(r) J_0(qr), \tag{B.6}$$

where Q is the invariant.

From Guinier and Fournet,[82] $\gamma_f(r)$ may be determined by:

$$\gamma_o(r) = \frac{\overline{V_p(r)}}{V_p} \tag{B.7}$$

where $\overline{V_p(r)}$ is the overlapping volume of two identical particles separated by a distance r. For infinitely long parallel rods, a shift in the axial direction produces no change in V_p. The correlation function for oriented rods, $\gamma_f(r)$, therefore becomes:

$$\gamma_r(r) = \frac{\overline{A_f(r)}}{A_f} \tag{B.8}$$

where $\overline{A_f(r)}$ is the overlapping area of two circles with radius R, such that,

$$\overline{A(r)} = 4\int_{r/2}^{R} \sqrt{R^2 - x^2}dx \tag{B.9}$$

The integral may be solved by means of trigonometric substitution, giving a solution for the correlation function of:

$$\gamma_f(r) = 1 - \frac{2}{\pi}\tan^{-1}\left(\frac{r}{2\sqrt{R^2 - r^2/4}}\right) - \frac{1}{\pi}\sin\left\{2\tan^{-1}\left(\frac{r}{2\sqrt{R^2 - r^2/4}}\right)\right\} \tag{B.10}$$

For $r \ll R$

$$\tan^{-1}\left(\frac{r}{2\sqrt{R^2 - r^2/4}}\right) \Longrightarrow \frac{r}{2R} \tag{B.11}$$

and

$$\gamma_f(r) \Longrightarrow 1 - \frac{2}{\pi R}r \tag{B.12}$$

Having obtained a functional form for $\gamma_f(r)$, the integral in equation B.6 can be solved. Using the form of $\gamma_f(r)$ for small r, the solution to two integrals must be determined:

$$\frac{1}{q^2}\int qrJ_0(qr)d(qr) \qquad \text{and} \tag{B.13a}$$

$$\frac{2}{\pi R q^3}\int (qr)^2 J_0(qr)d(qr) \tag{B.13b}$$

Using the properties of Bessel functions, the following relations may be obtained:

$$\int xJ_0(x)dx = xJ_1(x) \tag{B.14a}$$

$$\int x^2 J_0(x)dx = x^2 J_1(x) + xJ_0(x) - \int J_0(x)dx \tag{B.14b}$$

Combining equations B.6,B.12, and B.14, the intensity due to scattering from infinitely long cylinders may be obtained. As in the original derivation of Porod's law, all but one of the terms is a diminishing oscillatory function of q. Grouping those terms together, the

intensity can then be given by:

$$\lim_{q\to\infty} \frac{I_f(q)}{Q_f} = \left[\frac{2}{\pi R}\int_0^\infty J_0(qr)d(qr) + \text{Oscillatory terms}\right], \tag{B.15}$$

thus

$$\lim_{q\to\infty} \frac{I_f(q)}{Q_f} = \frac{2}{\pi R}q^{-3}, \tag{B.16}$$

which is Porod's law for oriented rods.

Appendix C

Power-Law Model for Diffuse Boundary Particles

C.1 Diffuse Boundaries Described By a Convolution Integral

There have been many empirical forms proposed in the literature for the diffuse boundary modification to particle structure.[46,47,55,56] One method for determining the effect of diffuse boundaries on the scattering intensities involves the use of convolution methods[55] in describing the density function. In this method, the density function $\rho_o(r)$ is modified by convolution with a smoothing function

$$\rho_{\text{obs}}(r) = \rho_o(r) * h(r) = \int_{-\infty}^{\infty} \rho(r\prime)h(r\prime - r)dr\prime \tag{C.1}$$

where $h(r)$ is the smoothing function.

Following the arguments of Koberstein and Ruland,[46,55] the scattering intensity can be described by:

$$I_{\text{obs}}(q) = \mathcal{F}\{\gamma_o(r)\}\,\mathcal{F}\left\{h^{*2}(r)\right\} = I_p(q)H^2(q) \tag{C.2}$$

where $\mathcal{F}\{\}$ indicates a Fourier transform, the exponent $*2$ indicates a self-convolution, $I_p(q)$ is the Porod law intensity, and $H(q)$ is the Fourier transform of $h(r)$. This method has an

advantage when dealing with oriented rod modifications to Porod's law in that the derivation of the diffuse boundary modifications may be dealt with separately from the modifications to Porod's law.

C.2 Density at Boundaries From Power-Law Smoothing

A power law smoothing function may be written as:

$$h(r) = \frac{1-\beta}{\Delta}\left(\frac{|r|}{\Delta}\right)^{-\beta} \qquad 0<\beta<1 \qquad -\Delta<r<\Delta \tag{C.3}$$

with $r = 0$ defining the boundary of the particle and Δ the width of the diffuse boundary. It is worth noting that this form is similar to that of Schmidt et al.,[56] although, Schmidt does not employ a density convolution.

Applying the convolution operation with this smoothing function gives a density distribution function described by:

$$\begin{aligned} \rho_{\text{obs}}(r) &= \tfrac{1}{2}\rho_o\left[1+\left(\tfrac{-r}{\Delta}\right)^{1-\beta}\right] \qquad -\Delta<r\leq 0 \\ &= \tfrac{1}{2}\rho_o\left[1-\left(\tfrac{r}{\Delta}\right)^{1-\beta}\right] \qquad 0\leq r<\Delta \end{aligned} \tag{C.4}$$

To provide a continuous density in the interior of the particle, Δ is set to R, the radius of the particle.

C.3 Intensity From a Power-Law Smoothing Function

The intensity factor, $H(q)$, is the Fourier transform of $h(r)$:

$$H(q) = \int_{-\infty}^{\infty} h(r)\cos(qr)dr \tag{C.5a}$$

$$= (1-\beta)(qR)^{\beta-1}\int_0^{\infty}\frac{\cos(x)}{x^{\beta}} \tag{C.5b}$$

$$= \left(\frac{1}{qR}\right)^{1-\beta}\frac{(1-\beta)\pi}{2\Gamma(\beta)\cos(\beta\pi/2)} \qquad 0<\beta<1 \tag{C.5c}$$

and

$$H^2(q) = \left(\frac{(1-\beta)\pi}{2\Gamma(\beta)\cos(\beta\pi/2)}\right)^2 \left(\frac{1}{qR}\right)^{2-2\beta} \qquad 0 < \beta < 1 \tag{C.6}$$

Thus, applying equation 3.32, the intensity for oriented rods with power-law diffuse boundaries has the form:

$$\frac{I(q)}{Q} = \frac{2}{\pi}\bar{R}^{-3+2\beta}\left(\frac{(1-\beta)\pi}{2\Gamma(\beta)\cos(\beta\pi/2)}\right)^2 q^{2\beta-5} \tag{C.7}$$

Appendix D

Fitting Methodology

D.1 Fitting to Identify Power-Law Regions

A fitting algorithm was designed which would allow for the identification of three power-law regions within a data set and determine the exponential factor for each power-law region. The algorithm was composed of a grid search technique applied to a three section piecewise linear equation.[83] The breakpoint locations were determined by finding the q values which gave the maximum adjusted R^2 value ($\overline{R^2}$).[84,85]

The multiple-correlation coefficient, R^2, is a measure of the reduction in the variability of the dependent variable (y) obtained using the given independent variables (x_1, x_2, x_3, $\cdots$) and is useful for determining the optimal model functional form.[86,87] The value of R^2 varies between 0 and 1, with 1 indicating a perfect fit to the data, and is defined by:

$$R^2 = \frac{\sum_{i=1}^{n} (\hat{y}_i - \bar{y})}{\sum_{i=1}^{n} (y_i^2 - n\bar{y}^2)} \tag{D.1}$$

where n is the number of data points, $\hat{y}_i$ is the value of y_i predicted by the model, and $\bar{y}$ is the mean value of y. To guard against the inclusion of unnecessary variables, the adjusted R^2 values ($\overline{R^2}$) are used:

$$\overline{R^2} = \left(\frac{n-1}{n-p}\right) R^2 + 1 - \left(\frac{n-1}{n-p}\right) \tag{D.2}$$

where p is the number of regressor variables.

The fitting algorithm proceeded as follows: The power-law intensity relations were mapped onto the three section linear equation:

$$Y = C_o + C_1 X + C_2(X-a)_+ + C_3(X-b)_+ + C_4 X_2 \tag{D.3a}$$

where

$$\begin{aligned}(X-a)_+ &= X-a \quad \text{for} \quad x > a \\ &= \quad 0 \qquad\quad \text{otherwise}\end{aligned} \tag{D.3b}$$

$$\begin{aligned}(X-b)_+ &= X-b \quad \text{for} \quad x > b \\ &= \quad 0 \qquad\quad \text{otherwise}\end{aligned} \tag{D.3c}$$

and

$$Y = \ln(\text{Intensity}) \tag{D.3d}$$

$$X = \ln(q) \tag{D.3e}$$

$$a = \ln(q_1) \tag{D.3f}$$

$$b = \ln(q_2) \tag{D.3g}$$

with q_1 and q_2 being the first and second break points respectively and $X_2 = 0$ or 1 depending on which of the two opposite angles the data point is associated with. Values of a and b were varied and for each combination of a and b fit parameters were estimated and $\overline{R^2}$ was computed, giving a two-dimensional data set of $\overline{R^2}$ values, as shown in figure D.1. From this data set, a point of maximum $\overline{R^2}$ was determined.

Having obtained the a and b values which gave the best $\overline{R^2}$, values for the two breakpoints were calculated, and power-law exponents were determined from the estimates of the fit parameters C_1, C_2 and C_3.

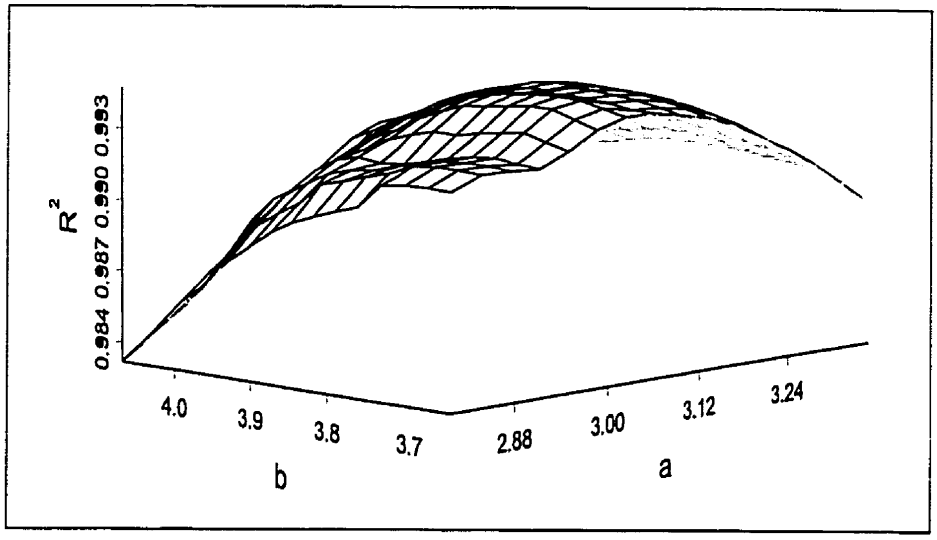

Figure D.1: Typical $\overline{R^2}$ distribution as a function of a and b. The maximum on this surface indicates the location of the two breakpoints.

D.2 Model Fitting

The fitting algorithm used for the *Sigmoidal-Gradient* and *Power-Law* models were designed specifically to compare these two models. To ensure an accurate comparison, the form of the fitting for the two models was made as similar as possible. The fit equations for the two models followed the forms:

$$Y = C_o + C_{s_1} X_s + C_{s_2} X_{s_2} \tag{D.4a}$$

where

$$Y = \ln(Iq^3) \tag{D.4b}$$

$$X_s = q^2 \tag{D.4c}$$

$$X_{s_2} = (X_s - b)_+ \tag{D.4d}$$

and

$$Y = C_o + C_{p_1} X_p + C_{p_2} X_{p_2} \tag{D.5a}$$

where

$$Y = \ln(Iq^3) \tag{D.5b}$$

$$X_p = \ln(q) \tag{D.5c}$$

$$X_{p_2} = (X_p - b)_+ \tag{D.5d}$$

with $(X_s - b)_+$ and $(X_p - b)_+$ being defined in the same manner as in equation D.3c. In this way, a comparison of $\overline{R^2}$ for the two models gave a good indication of which model best described the data.

In addition, the segmented linear equation allows for the testing of combined models such as:

$$Y = C_o + C_{s_1} X_{s_1} + C_{p_2} X_{p_2} \tag{D.6}$$

The four possible models based on combinations of X_s and X_p could then be compared, using calculated $\overline{R^2}$ values, to determine which best describes the data.

Famous Last Words:

Of making many books there is no end, and much study wearies the body.
Now all has been heard; here is the conclusion of the matter: Fear God and keep his commandments for this is the whole duty of man.

Ecclesiastes 12:12,13

TEST TARGET (QA-3)

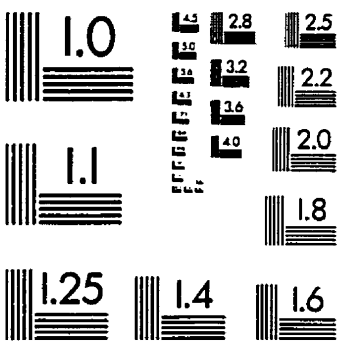

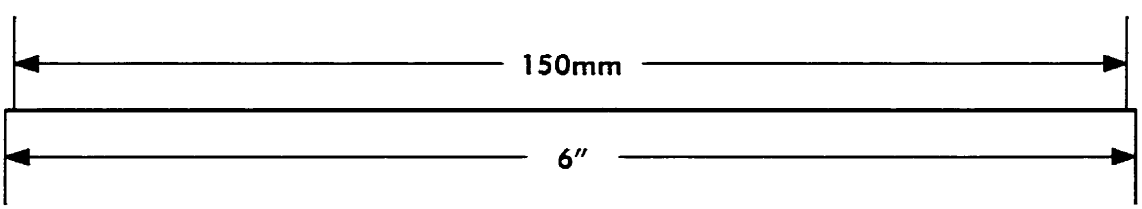

APPLIED IMAGE, Inc
1653 East Main Street
Rochester, NY 14609 USA
Phone: 716/482-0300
Fax: 716/288-5989